STABILIZING ORDERED BICONTINUOUS PHASES IN DIBLOCK COPOLYMER SYSTEMS

A Dissertation

Presented to the Faculty of the Graduate School

of Cornell University

In Partial Fulfillment of the Requirements for the Degree of

Doctor of Philosophy

by

Francisco Javier Martinez

May 2009

STABILIZING ORDERED BICONTINUOUS PHASES IN DIBLOCK COPOLYMER SYSTEMS

Francisco Javier Martinez, Ph. D.

Cornell University 2009

A combination of coarse-grained particle-based molecular simulations and self-consistent field theory (SCFT) were used to detect and circumvent the packing frustration responsible for the very limited stability of the bicontinuous phases in DBC systems. Such bicontinuous phases have promising applications in many technological areas like: solar-cells and photonic crystals. Lattice and continuum Monte Carlo simulations together with Molecular Dynamics were used to map out the phase diagram of the pure DBC melt. The morphologies observed were found to be dependent upon the size of the simulation box because of severe finite-size effects caused by the long-range periodicity of this type of systems. Thus, accurate free energy calculations, achievable only through Expanded Ensemble methods, were needed to discern the stability of the competing mesophases at each thermodynamic condition. The gyroid (G) phase was found to be stable in a narrow region of phase diagram. Direct evidence of packing frustration in the form of chain-stretching was found in the G phase nodes for all the models studied. Chain-length bidispersity was then investigated as a means to reduce such packing frustration; it was found that the preferential segregation of the longer chains inside the G phase nodes caused an increase in the range of temperatures where the G phase was stable. As an alternative strategy to diminish packing frustration, addition of minority-component homopolymer, was studied at the conditions were the G phase was found stable in the

pure DBC system. The progression of morphologies G → C → Double Diamond (DD) → Plumber's Nightmare (P) was observed upon increasing homopolymer content. The homopolymer concentrated in the nodes of the DD and P phases to reduce the packing frustration. Though tentative phase boundaries were delineated via free energy calculations, macrophase separation could not be satisfactorily assessed within the framework of particle-based simulations. Thus, SCFT was used to explore in more detail the DBC/homopolymer phase diagram, showing that, although in many cases two-phase coexistence of a DBC-rich phase and a homopolymer-rich phase precedes the stability of complex bicontinuous phases, the DD and P phases can indeed be stable in some regions of the phase diagram.

BIOGRAPHICAL SKETCH

Francisco Javier Martinez Veracoechea was born on December 2, 1980 in Caracas, Venezuela. In 1998 he started his studies as a Chemical Engineer in Universidad Simon Bolivar where he obtained his Bachelor's Degree in 2003. Shortly after that (January 2004), he joined the Ph.D. program of the Chemical and Biomolecular Engineering Department at Cornell University.

Dedicado a mi querida familia que amo y extraño, y que siempre me ha apoyado en todas las decisions que he tomado.

ACKNOWLEDGMENTS

I gratefully acknowledge the guidance and full-time dedication that my advisor Fernando Escobedo has given to me during the last five years of my life in helping me achieving the completion of my Ph.D. Degree.

TABLE OF CONTENTS

LIST OF FIGURES

LIST OF TABLES

CHAPTER 1

LATTICE MONTE CARLO SIMULATIONS OF THE GYROID PHASE IN MONODISPERSE AND BIDISPERSE BLOCK COPOLYMER SYSTEMS*

I. INTRODUCTION

Under the appropriate thermodynamic conditions, block copolymers can self-organize at nanoscopic length scales and form microstructures that can lead to numerous materials with useful properties[1] such as mechanical and optical anisotropy, large interface area between different domains, and long-range ordering. In diblock copolymer melts, different microstructures can be obtained by changing the temperature and volume fraction of any one block. The result is a complex phase diagram that presents a variety of well ordered structures with long-range periodicity. In the simple case of diblock copolymer melts, the following "classical" morphologies[1] can be found: lamellae (L), hexagonally packed cylinders (C), and spheres ordered in a BCC lattice (S). In addition, bicontinuous morphologies with triply periodic spacing have been discovered; e.g., in diblock melts the Gyroid[2] (G) phase has been found to be stable. In more complex systems, like star block copolymer melts and block copolymer/nanoparticle nanocomposites, the OBDD[3] (D) and Plumber's Nightmare[4] (P) phases have been respectively obtained. Bicontinuous morphologies are of special interest for the design of novel materials. For example, their interconnectivity in all three directions not only gives them unusual mechanical properties, but also makes them perfect candidates as precursors of porous materials,[5, 6] catalytic surfaces and high conductivity nanocomposites.[7] Theoretical and molecular

simulation studies are particularly useful tools to explore the complex phase behavior of both pure diblock copolymers and mixtures of copolymers and other components such as nanoparticles[8-10] and homopolymers.[11] From the numerous computational studies that have been reported, we will briefly review some of the most relevant to this work.

The phase diagram of pure diblock copolymer melts is relatively well understood, both experimentally[12] and theoretically (e.g., the SFCT of Matsen[13, 14] and the Field-Theoretic description of Fredrickson[15]). However, even though the G phase has been proven to be stable in a narrow window of compositions in this kind of theoretical studies,[14, 16, 17] to the best of our knowledge, it has never been reported in simulations of pure diblock melts. The G phase has only been found in simulations of systems of either triblock copolymers or diblocks with selective solvent; e.g., in the lattice MC simulations of triblock copolymer melts of Dotera et al.,[18] in the lattice MC work with surfactants in selective solvent of Larson et al.,[19] in the MD simulations of Rychkov and Yoshikawa[20] in a selective solvent, and in the Lattice-Boltzmann simulations of surfactants in mixtures of selective solvents of González-Segredo and Coveney.[21] One should consider, however,[11] that the inclusion of selective solvent or small amounts of homopolymer can stabilize the G phase, widening the range of conditions where such a phase can be observed by simulation. It has also been shown[16, 22] that the region of the phase diagram where the G phase is stable for triblock copolymers is significantly wider than that for diblocks, which again facilitates finding the G phase in simulations.

In several simulations of diblock copolymers without selective solvent, no clear indication has been provided on the existence of bicontinuous phases. Such is the case of the Brownian Dynamics simulations of Glotzer et al.[23, 24] and the Dissipative Particle Dynamics simulations of Groot et al.[25] where only classical morphologies

were found. The same is true for the Discontinuous Molecular Dynamic simulations of Schultz et al.[26, 27] where they studied diblock copolymer melts and block copolymer/nanoparticle nanocomposites. In this case, the Perforated Lamellae phase (PL) was found in the region of the phase diagram where the G phase is expected, in disagreement with both theory and experiments.[28]

Block copolymers microphases present long-range order with periodicity that has well-defined characteristic lengths associated with it. The size of the unit cell (i.e. repetitive unit) of these structures is therefore predetermined by the thermodynamic conditions at which the system is set. As a consequence, simulation box lengths need to be a multiple integer of the unit cell size in order to fit the structure and still satisfy the periodic boundary conditions. Simulations have proven[18] that inadequate choices of box dimensions can stabilize metastable phases. As a result, the size of the simulation box becomes an essential parameter in this kind of systems. An attempt to solve this problem was made by Schultz et al.[29] who developed an algorithm to change the shape of the simulation box while keeping fixed the total volume. Nonetheless, due to their cubic symmetry, bicontinuous morphologies cannot be fitted in a simulation box by changing its relative dimensions if the total volume is kept constant. The latter reason could be a possible explanation for the failure of previous work in obtaining the G phase.

In the present work we use lattice Monte Carlo (MC) simulations together with a simple model for the block copolymer chains to explore the phase diagram of pure diblock melts. Simulations were performed in the weak, intermediate, and strong segregation regime. In addition to the classical morphologies, the G phase was also found in a region of the phase diagram that agrees with experimental results and theoretical predictions. We also explored the use of polydispersity as a way to stabilize

the Gyroid phase in a wider region of the phase diagram as proposed by Hasegawa et al.[30]

II. MODEL AND METHODS

Model

Space is discretized in a simple cubic lattice where each site can be occupied only by a single bead of the polymer chain. Each bead in the chain represents a Kuhn segment. Bonds are allowed between nearest neighbors that are located at the edges of each site as well as between diagonals sites, yielding to a total of 26 neighbors per lattice site. Details about the applicability of this kind of lattice for block copolymers can be found elsewhere.[31, 32]

The total energy of the system is calculated by using pair wise additivity between the bead interactions. Each bead interacts only with its 26 nearest neighbors. The contact energy ε_{ij} is defined as,

$$\varepsilon_{ij} = \begin{cases} 1 \; if \; i \neq j \\ 0 \; if \; i = j \end{cases} \tag{1}$$

where *i* and *j* represent the type of bead.

To facilitate the mobility of the chains, the systems have a void fraction of $\eta = 0.25$. The beads do not interact with the void (i.e. $\varepsilon_{i\text{-void}} = 0$), hence vacuum acts like a non-selective good solvent. As is customary for lattice simulations, the Flory-Huggins interaction parameter (χ) is obtained from[18] χN=(# non-bonded neighbors)×(fraction occupied)×ε_{AB}/kT = (26-2)×(1-η)×1×β, i.e.,

$$\chi = 18\beta \tag{2}$$

where $\beta = \varepsilon_{AB}/kT$, k is Boltzmann constant, and T is temperature. Note that this mapping between χ and T is only approximate since small-chain effects are not accounted for. The copolymer composition is defined by,

$$f = \frac{\#\text{ of beads of one component in chain}}{N} \tag{3}$$

where N is the chain length. Since all beads occupy the same volume, f also defines the volume fraction of the given bead type. For the system of pure diblock copolymers, chains had N=20 unless otherwise indicated. Such a chain length is a compromise between computational efficiency (short chain) and a sufficiently fine discretization of block copolymer composition to map out the phase diagram. Therefore it is not surprising that chains of comparable lengths have been studied elsewhere.[18, 26] As a concrete example, N = 20 can be seen to approximately correspond to symmetric chains of Poly(isoprene-b-ethylene oxide) (PI-b-PEO) of a molecular weight of $MW \sim 2.5.10^3$ g mol^{-1}. For the bidisperse system of diblock copolymers, the shorter component had N=20 while the longer one had either N=40 or N=26.

Simulation details

The sampling scheme used was the traditional Metropolis Monte Carlo algorithm[33] in the Canonical Ensemble (NVT), where moves are accepted with probability:

$$P = \min[1, \exp(-\beta \Delta E)] \tag{4}$$

The moves implemented were: (1) individual "hop" moves,[31] where a single bead is attempted to move with equal probability to any of the sites that conserve the nearest neighbor condition between chemically bonded monomers; (2) "Reptation" moves,[19] where one of the two ends of the chain is moved randomly to one of the

nearest neighbor sites, and the rest of the beads "follow" it by occupying the position of the closest bead chemically bonded in the direction of the move; (3) "Switching" moves, whereby the order of the beads in the chain is inverted. This last move has the advantage of never requiring a check of excluded volume interactions, since the chain occupies the same sites before and after the move is implemented. The "hop", "reptation" and "switching" moves were performed with a relative frequency of 100**:**10**:**1 respectively.

Copolymer mesophases and bicontinuous phases in particular are not easy to characterize because of the lack of a convenient order parameter that can provide a clear identification of any such phase. As a consequence, most of the characterization is usually done through simple visual inspection of snapshots of the simulated system. Another powerful tool, widely used by experimentalists in the area of copolymers, to characterize these phases is the structure factor, ***S(q)***. The structure factor is calculated straightforwardly from simulations with the equation,[34]

$$S(\vec{q}) = \frac{(\sum_j \cos(\vec{q} \bullet \vec{r}_j))^2 + (\sum_j \sin(\vec{q} \bullet \vec{r}_j))^2}{N} \qquad (5)$$

where $\vec{q}$ is the wave vector and $\vec{r}_j$ are the positions of the monomers of the minority component in the system. With this definition, ***S(q)*** corresponds to the modulus of the Fourier transform of the positions of the minority component beads. Moreover, after calculating ***S(q)***, the concentration profile can be reconstructed directly[35] by an inverse Fourier transformation while neglecting wave vectors ($\vec{q}$) with a modulus larger than some cutoff (in this work q_{cutoff}=1.2). This procedure has the advantage of smoothing out the fluctuations in a particular configuration. All snapshots shown in this work were obtained using this procedure. Another advantage of calculating ***S(q)*** is that it provides useful information about the "natural" length of the unit cell of the periodic

structures. Such length can be extracted from the location of first refraction peak, by means of the equation,

$$L_{box} = \frac{2\pi}{q^*} m \tag{6}$$

where L_{box} is the estimated length of the unit cell, q^* is the modulus of the wave vector at which the principal $S(\mathbf{q})$ maximum is located and m is the first observed reflection spacing ratio for a given periodic structure[2] (e.g., $m=1$ for Lamellae, $m=\sqrt{6}$ for the Gyroid).

Simulations were equilibrated in the athermal limit and then quenched to the desired temperature where the microstructures are expected to form. It is important to emphasize that contrary to the case of SCFT calculations, the different morphologies need not be pre-specified since the system naturally evolves towards the final state. Typical simulation runs consisted of 10^6 MC moves per bead in the system. Some simulations were run twice as long to ensure stability. At each thermodynamic condition (i.e., a given set of χN and f values), a preliminary simulation was run at a simulation box of a typical size of $30\times30\times30$ (lattice units)^3 to obtain a hint of the "natural" spacing of the system by means of $S(\mathbf{q})$. Afterwards, different unit cell sizes corresponding to different morphologies can be estimated by use of equation 6 (an iteration of this process may be needed). Thus, different simulations (with the same value of χN and f), with different box sizes, consistent with the spacing of different morphologies, were run. However, in most of the cases the system evolved to the same morphology regardless of the simulation box size. Whenever more than one defect-free morphology was found at the same thermodynamic conditions, the stable phase was determined by performing simulations in bigger boxes (i.e., two or more unit cells) and evaluating the chemical potential. Simulation box sizes ranged from

$20\times20\times20$ (lattice units)^3 to $66\times66\times66$ for larger systems wherein the stability of the system was being tested.

III. RESULTS

Pure diblock melts

In order to map out the phase diagram of pure diblock copolymer melts simulations were performed in the weak, intermediate, and strong segregation regimes (χN~20 to 200). Since for our model the phase diagram is symmetric in volume fraction (f), we ran simulations only for compositions $f \leq 0.5$.

We obtained the classical morphologies of Lamellae (L), Cylinders (C) and Spheres (S) as can be seen in Figure 1.1 where only the minority component of the block copolymer is shown. Since the L and C phases possess periodicity only in one or two directions, respectively, they can rotate to better accommodate themselves in the simulation box to approach their natural spacing. To test if this "rotation" was artificially stabilizing any of these structures different system sizes were tried. However, no "artificial" stabilization was observed. Although some authors[25, 36] have suggested that hydrodynamic interactions could be crucial to simulate structures with periodicity in more than one dimension (specifically the C phase), Horsch et al.[24] have recently shown that hydrodynamics was not required to obtain these phases in simulations of diblock copolymers. The Lattice MC method employed in this work provides a much more effective configurational sampling than continuum space models and can readily obtain the C phase (despite the absence of hydrodynamics interactions).

In addition to the classical morphologies, in a very small region of the phase diagram the Gyroid phase (Figure 1.2) was found. To ensure that this structure actually corresponds to the G phase, $S(\boldsymbol{q})$ was calculated (Figure 1.3) and compared to

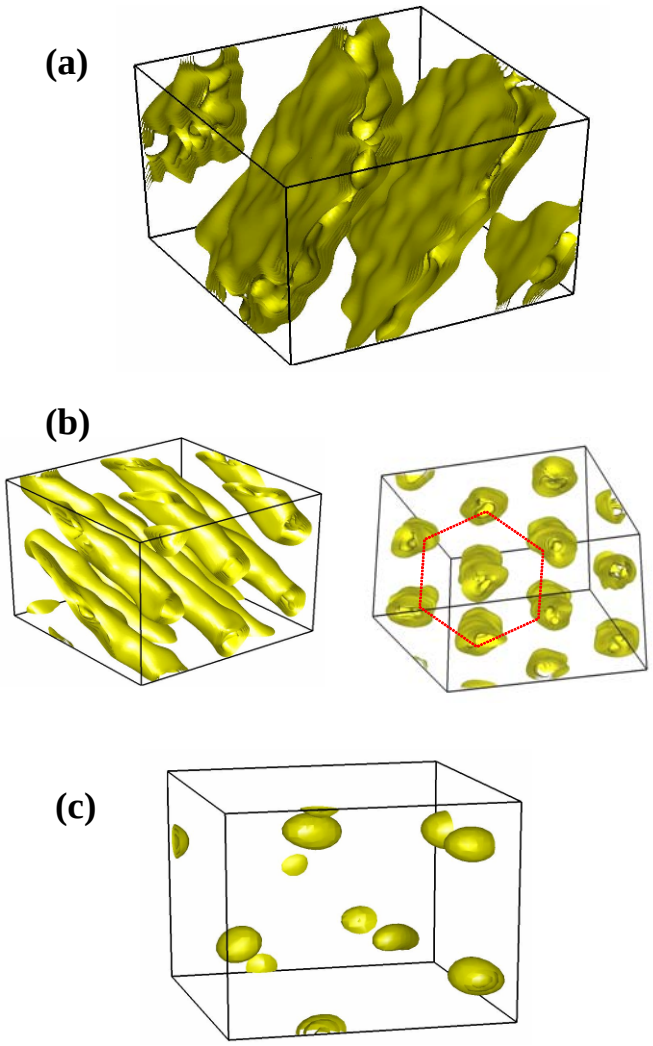

Figure 1.1. Snapshots of classical morphologies found in the simulations. Only minority component is shown. (a) Lamellae, (b) Cylinders and (c) Spheres.

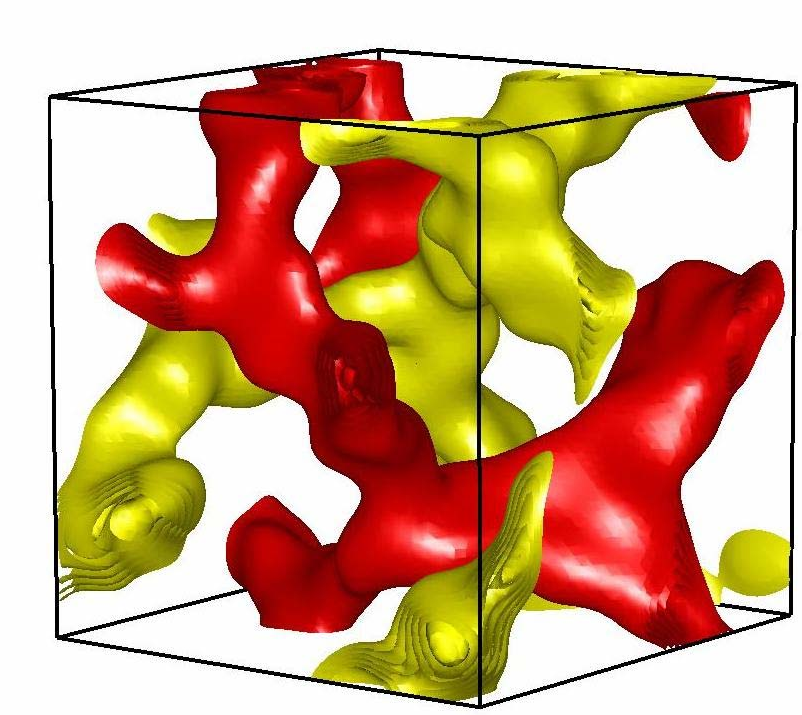

Figure 1.2. Snapshot of the unit cell of the Gyroid phase. Only the minority component is shown. The minority component forms two distinct channels (red and yellow) that never intersect.

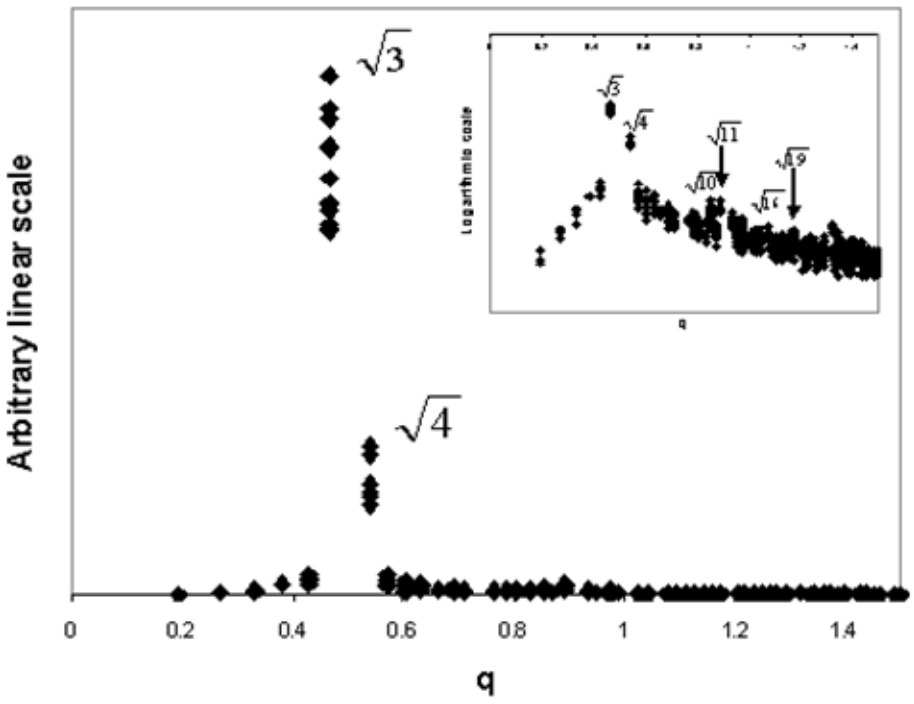

Figure 1.3. Structure factor calculated from simulated snapshots of the G phase. The inset shows the structure factor in a logarithmic scale. The ratio of the locations of the peaks is in good agreement with the experimental results[2] (i.e., $\sqrt{3}:\sqrt{4}:\sqrt{10}:\sqrt{11}:\sqrt{16}:\sqrt{19}$).

the experimental results of Gruner et *al*.[2] Comparison of the location of the peaks shows good agreement with the ratios that are observed experimentally (i.e., $\sqrt{3} : \sqrt{4} : \sqrt{10} : \sqrt{11} : \sqrt{16} : \sqrt{19}$). Moreover, when these ratios are reinterpreted as $\sqrt{6} : \sqrt{8} : \sqrt{20} : \sqrt{22} : \sqrt{32} : \sqrt{38}$ (i.e., multiplied by a factor of $\sqrt{2}$, as suggested by Gruner *et al*.[2]), it can be seen that the size of the unit cell given by equation (6) [with q^*=0.4664 from Fig. 1.2] coincides exactly with the size of the simulation box (i.e., 33 lattice units per side). In Figure 1.2, we can also see that the minority component forms a structure composed by "channels" and "nodes", each node is formed by the junction of three channels, as is expected for the Gyroid phase.

At the same thermodynamic conditions where we obtained the G phase (i.e., f = 0.30, χN = 40), we also found other structures when simulations were done in boxes of different sizes (e.g., C and Perforated Lamellae). However, the PL was only encountered in simulations with boxes much smaller than the G unit cell (less than 20 lattice units each side) leading us to conclude that PL is not stable in this thermodynamic state. To test the stability of the G phase respect to the C phase, two bigger boxes (33×33×66 lattice units) were simulated. In these simulations, instead of quenching from the athermal limit, simulations were started with the respective phases (C or G) already formed. While the C phase did not persist (i.e., cylinders started to connect to each other), the G phase remained stable. In addition, simulations with an even bigger simulation box (66 lattice units per side) were run; again, the Gyroid phase remained stable (Figure 1.4). Simulation of the chemical potential in fully equilibrated systems using Rosenbluth sampling[33] was used to identify the most stable phase; i.e., the one with the lowest free energy. We neglected the PV contribution to the Helmholtz free energy differences since it is expected that for the G and C phases the pressure will be similar and small. It can be seen in Figure 1.5(a) that the box dimensions for which the G phase was found (i.e., 33 lattice units per side) correspond

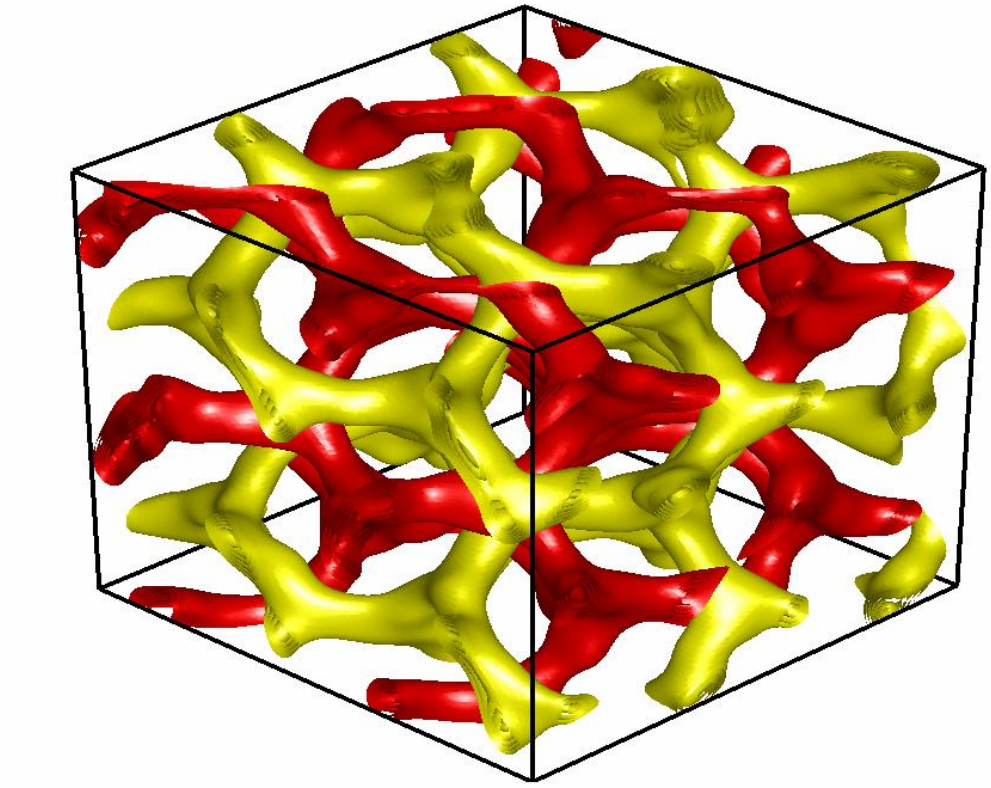

Figure 1.4. Eight (8) unit cells of the Gyroid phase; the box size is 66×66×66 and contained 10,781 chains. The G phase remained stable in this bigger system. Only the minority component is shown.

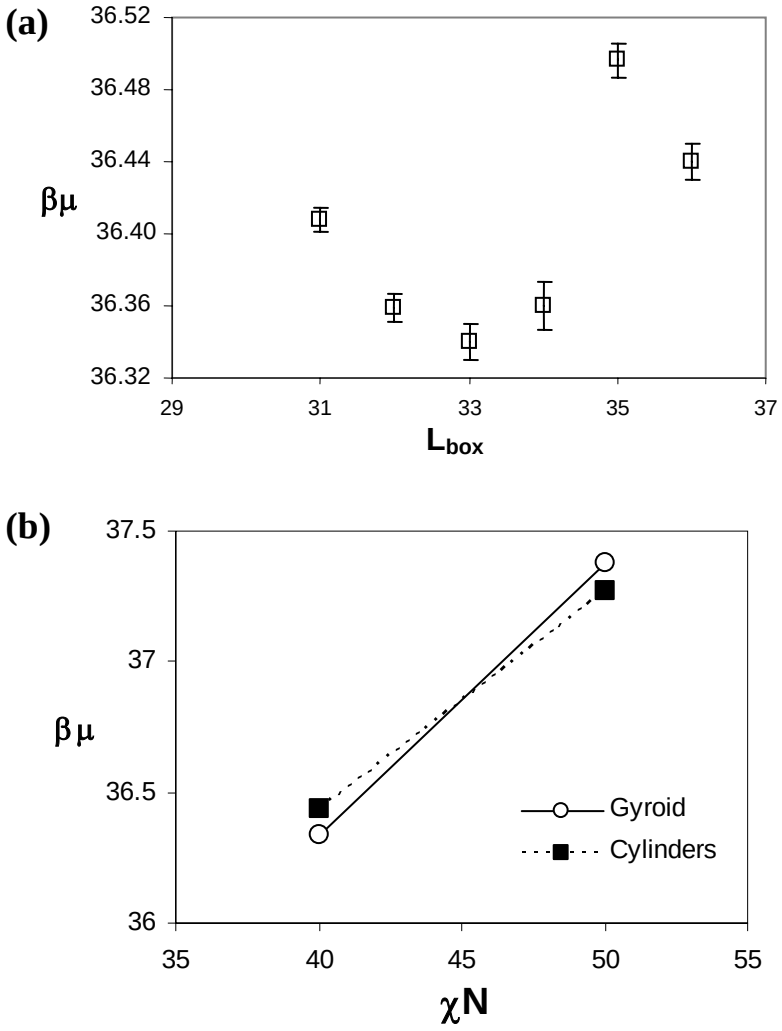

Figure 1.5. Comparison of the chemical potentials (βμ) between the G and C phases for f=0.30. (a) The chemical potential for the observed structure for each box size is presented as a function of the box linear dimension (L_{box}) for χN = 40. The structures observed at different sizes are: Interconnected Cylinders for L_{box} = 31, G phase for L_{box} ={32, 33, 34}, and C phase for L_{box} ={35, 36}. (b) Linear interpolation of βμ for the C and G phases between χN = 40 and χN = 50; for each phase and a given χN, the βμ value used is the smallest one obtained as a function of system size. The intersection occurs at χN ~ 45.

to a minimum in chemical potential. Using the lowest $\beta\mu$ value for which either G or C are stable, we find that $\beta\mu_{Gyroid} = 36.34(1)$ and $\beta\mu_{Cylinder} = 36.44(1)$, which indicates that the free energy of the G phase is slightly lower than that of the C phase at $f = 0.30$, $\chi N = 40$. As pointed out before,[18] inadequate choices of simulation box dimensions can stabilize metastable structures due to their inability to fit the unit cell of the stable structure. This effect becomes less important for much larger simulations boxes where two or more unit cells can fit. Since the G phase was the only one that remained stable in the much bigger systems (besides having a slightly lower chemical potential), we conclude that G is the stable phase at the conditions under consideration.

For $f = 0.30$ and $\chi N = 50$, only the C phase formed spontaneously. When quenching the simulated systems for different box sizes, a Gyroid-like structure was often initially observed; however, in all cases these unstable intermediates eventually evolved toward the C phase. Further tests were run at $f = 0.30$ and $\chi N = 50$ starting with the L or the G phase already formed (at different χN). In these simulations, only the G phase remained stable during the length of the simulation (10^6 MC steps) but its chemical potential [$\beta\mu_{Gyroid} = 37.38(1)$] was larger than that of the C phase [$\beta\mu_{Cylinder} = 37.27(1)$], confirming that that C phase is the one thermodynamically stable in this point of the phase diagram. Although we observed the G phase in only one point of the phase diagram (i.e., $f = 0.30$, $\chi N = 40$), we expect that it will be stable in a small finite interval of χN around this point [i.e., $\Delta(\chi N)<10$]. A rough estimate of the location of the high-χN G-C transition is $\chi N \sim 45$, found by linear interpolation [shown in Figure 1.5(b)] of the chemical potential data for $\chi N = 40$ and 50 given before.

For $f = 0.35$ and $\chi N = 40$, neither the G, L, or C phase was fully stabilized; instead, co-continuous structures were obtained where the minority component forms a single network of channels connected by three-fold nodes. Recently, Tyler and Morse[37] have shown using SCFT that an orthorhombic Fddd phase (O^{70}) should be

stable in a very narrow range of f and χN between the G and L phases. Regular co-continuous structures can be simulated depending on the box shape adopted; Figure 1.6 shows one such structure obtained for a box with side lengths in the ratio 35:35:70 (and for $f = 0.35$ and $\chi N = 40$). Although the structure in Figure 1.6 resembles the O^{70} phase, analysis of $S(\mathbf{q})$ shows some discrepancies in the location of the refraction peaks reported experimentally for systems of triblock copolymers by Bates et al.[38] Considering that the O^{70} phase is predicted to be stable in a very narrow region close to the ODT, it is possible that such a phase is suppressed in systems of "short" chains like ours, or that it is "skipped" by the coarse discretization of f values afforded by our 20-mer chains. Clearly, a more extensive simulation study is needed to clarify the effect of box size, shape, chain length, and composition on the formation of the O^{70} phase.

When all the resulting structures for the diblock copolymer melt are collected as a function of χN and f, we obtain the approximated phase diagram shown in Figure 1.7. This diagram is in qualitative agreement with the results of SCFT.[14] However, besides the appearance of the co-continuous structures previously mentioned, other differences are observed: the ODT is located at higher values of χN ($\chi N \sim 23$), the S phase is also shifted to higher values of χN, and a temperature driven Cylinder-Gyroid-Cylinder (C-G-C) transition is predicted. The up-shifting of the ODT and the S phase is in agreement with previous simulation results of Hall et al.,[26] and Vassiliev and Matsen,[39] where chains of similar size were used. In addition, weak segregation regime theory[17, 40] has predicted these two effects for chains of short length wherein fluctuations become important and therefore mean-field theories become no longer applicable.

Regarding the C-G-C transition, one should note first that SCFT actually predicts its occurrence but only for an extremely narrow range of f values (around

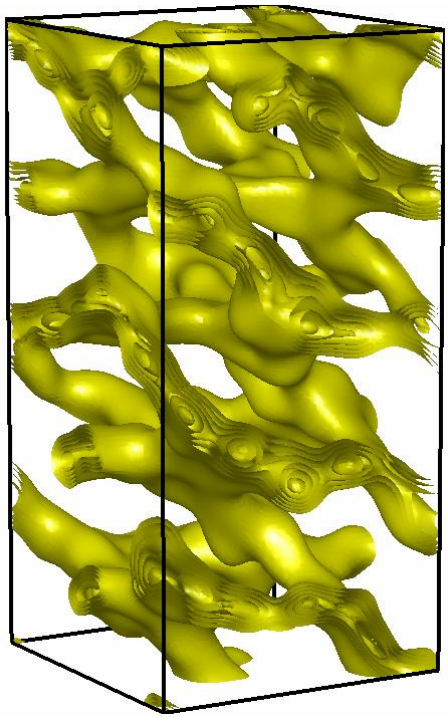

Figure 1.6. Snapshot of the co-continuous structure found at $f = 0.35$ and $\chi N = 40$. This structure was found only in a narrow region of the phase diagram between the L and G phases. Only the minority component is shown.

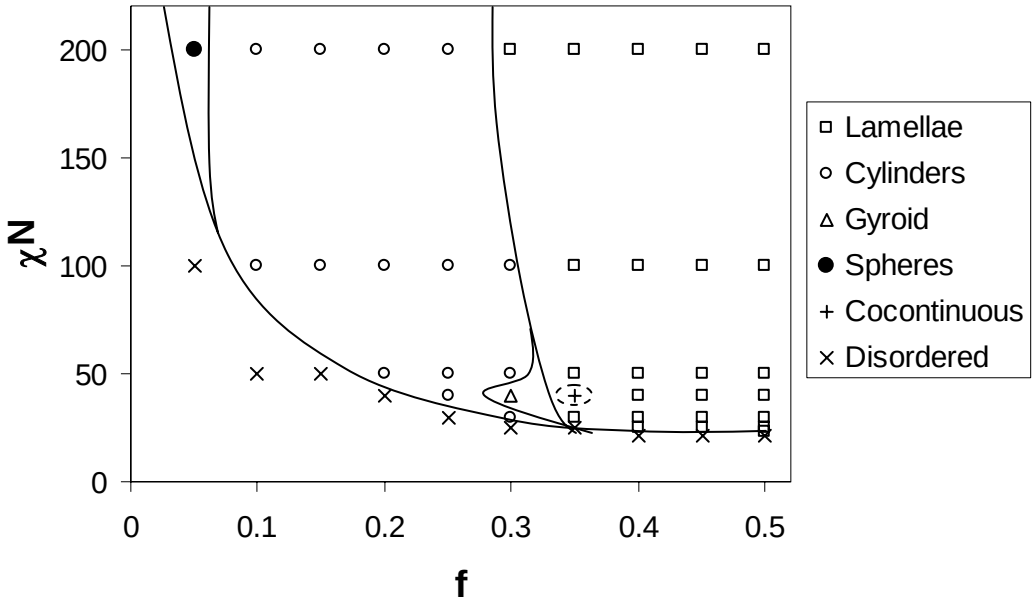

Figure 1.7 Approximate phase diagram obtained from our simulations. Solid line is just a guide for the eye. The ODT is located at $\chi N \sim 23$. The Gyroid phase was found stable for $\chi N = 40$ and $f = 0.30$.

f~0.32 and 45 < χN < 65). Furthermore, while SCFT clearly predicts a C-G transition at low values of χN, the exact location of the high-χN boundary of the G phase (i.e., the C-L-G high-χN triple-point) has not been established by rigorous SCFT calculations but only by extrapolations[14] (in the interval 40 < χN < 60 of the G phase boundaries). It is therefore not unexpected that in such a region of the phase diagram (where free energy differences among the L, G, and C phases are vanishingly small) discrepancies may arise between the predictions of a mean-field theory and the behavior of systems of finite chain-length. In addition, the experimental work of Bates et al.,[12] with the metastable PL phase re-interpreted as the G phase,[28, 41] suggests that not only C-G transitions at low values of χN can occur but also that G-C transitions at high values of χN are plausible (e.g., for PI-b-PS and PEP-b-PEE). In fact, most of the experimental work on the G phase has not examined the region where the G phase ceases to be stable at high segregations. In short, the possibility that systems can exhibit a C-G transition at low χN and a G-C transition at higher χN should not be ruled out *a priori*.

Structure of the nodes

In the Gyroid phase the minority component forms a structure composed of channels and nodes. The thickness of the channels is determined by the length of the minority component blocks. However, since each node is formed by the junction of three channels, nodes need to be bulkier in order to approach the constant mean curvature (CMC) structure[13] that minimizes the interfacial energy.

It has been suggested elsewhere[13, 30] that the reason for the very limited stability of the G phase in the phase diagram of pure diblock melts is packing frustration. Since the nodes of the G phase are wider than the channels, chains would need to stretch in the nodes to reach the center. Our simulated G phase allowed us to

examine whether this phenomenon occurs inside the nodes. Concentration profiles of the minority component in the simulated nodes show that there is indeed a low density region (i.e., a higher concentration of vacancies) inside the nodes. This is evident in Figure 1.8 where a typical concentration profile on a cross-section of a node is shown. As can be seen, the concentration in the middle of the node is lower than in its surroundings, evidencing the presence of vacancies. This fact was true for all thenodes present in all the snapshots of the Gyroid phase collected from independent runs. The presence of lower concentration regions in the center of the nodes indicates packing frustration of the copolymer chains and therefore a destabilization effect of the G phase. While some degree of vacancy accumulation also occurs at the A-B interfaces of all micro-segregated phases because it reduces the number of unfavorable contacts in the system, the vacancy accumulation in the node centers of the G phase is not driven by the same mechanism.

Chain stretching calculations (i.e., via the evaluation of end-to-end distances of the minority blocks) were carried out only for a limited number of statistically independent configurations (10 snapshots). This is because the only reliable way we found to identify of the positions of the Gyroid nodes was by visual analysis. The results from these calculations failed to detect chain stretching inside the nodes as it had been speculated, suggesting that, at least in our model, the penalty in entropy of mixing associated with having "vacancies" inside the nodes is less than the penalty in configurational entropy associated with stretching the chains to reach the center of the node. However, the absence of chain stretching inside the Gyroid nodes could also be due to the short length of the minority component block (6 beads for $f = 0.30$), given that the associated entropic penalty is larger for shorter, non-gaussian chains. Moreover, since in our model the contact energy between beads of the same type is *zero*, void spaces in the lattice act as a "good" solvent and the intra-node interactions

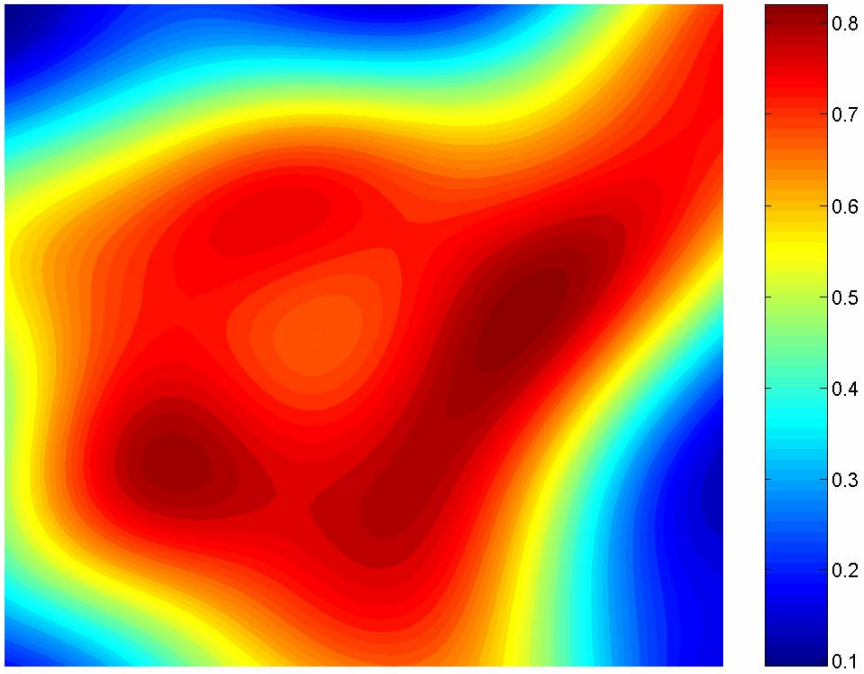

Figure 1.8. Concentration profile of the minority component in a typical node of the G phase. The concentration in the middle of the node is lower than in its surroundings indicating the presence of a higher concentration of vacancies. The scale represents the concentration of the minority component, ranging from 0 to 1.

are basically entropic. Hence, it is also possible that a model with more dominant energetic interactions (i.e., negative contact energies between equal-type beads and thus void spaces acting as "poor" solvent) could lead to a different nodal structure with less vacancies and more chain stretching. In either case, however, packing frustration inside the Gyroid nodes should still be prevalent.

Bidisperse mixtures of a diblock copolymer melt

Several strategies have been proposed to reduce packing frustration inside the G phase nodes, including the use of nanoparticles or low molecular weight homopolymers that could reside preferentially in the nodes of the Gyroid. In addition, Hasegawa et al.[30] suggested that copolymers having a bidisperse distribution of chain lengths could have a more stable G phase. In this case, the hypothesis is that longer chains can segregate to the nodes to fill the vacancies (Figure 1.9) while the shorter chains concentrate in the channels to avoid packing frustration in the nodes, therefore stabilizing the Gyroid phase. To our knowledge, this hypothesis has not been tested in simulations. Experimentally, Bendejacq et al.[42] have study the effect of polydispersity in diblock copolymers, finding the L and C phases (and coexistence L + C in between) but not the G phase; note that these authors focused in the strong segregation regime where the G phase is expected to be unstable. Also, Sides and Fredrickson[43] studied the effect of polydispersity using SCFT but only focused on the classical morphologies (L, C, and S).

We studied two model systems with the purpose of testing this hypothesis (Figure 1.10). The first one (System 1) was composed of 90 % chains of length N = 20, and 10 % chains with N = 40, with a volume fraction of minority component f = 0.30 (the same f where the G phase was found). The second system (System 2) had also 90 % of chains of length N = 20 and f = 0.30, but it contained 10 % of chains with

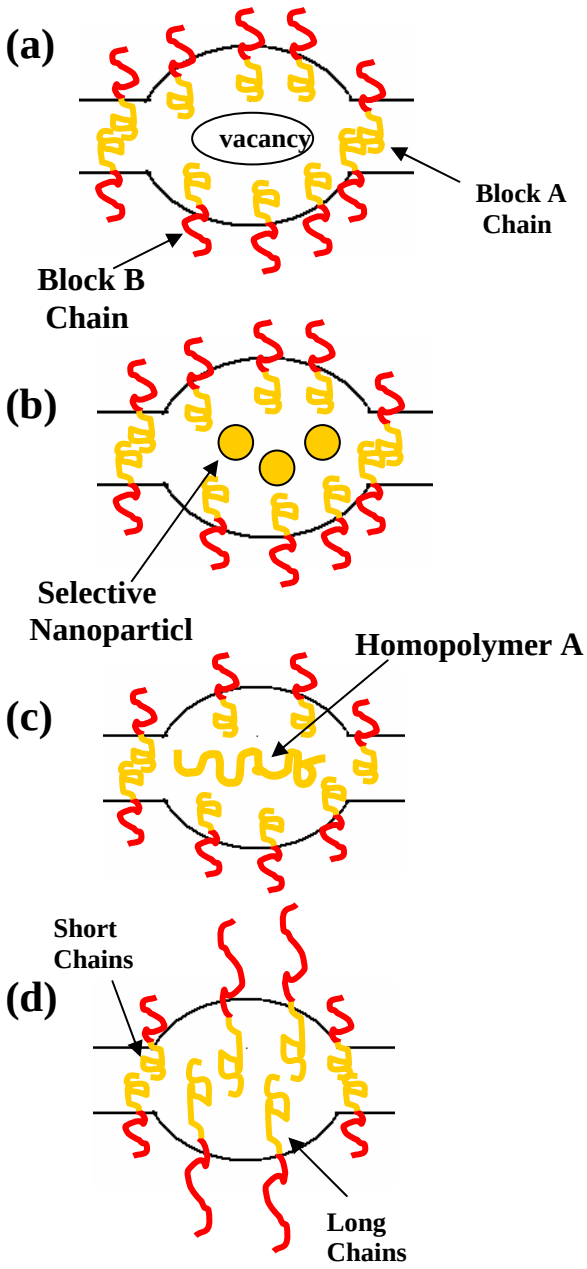

Figure 1.9. Cartoon representing how filling the "vacancies" in the nodes can stabilize the Gyroid phase. (a) Chains stretching in the Gyroid nodes to fill the vacancies. (b) Selective nanoparticles filling the vacancies. (c) Homopolymer filling vacancies. (d) Bidisperse distribution of chain length where the longer chains concentrate in the nodes. Based on a figure shown by Hasegawa et al.[30]

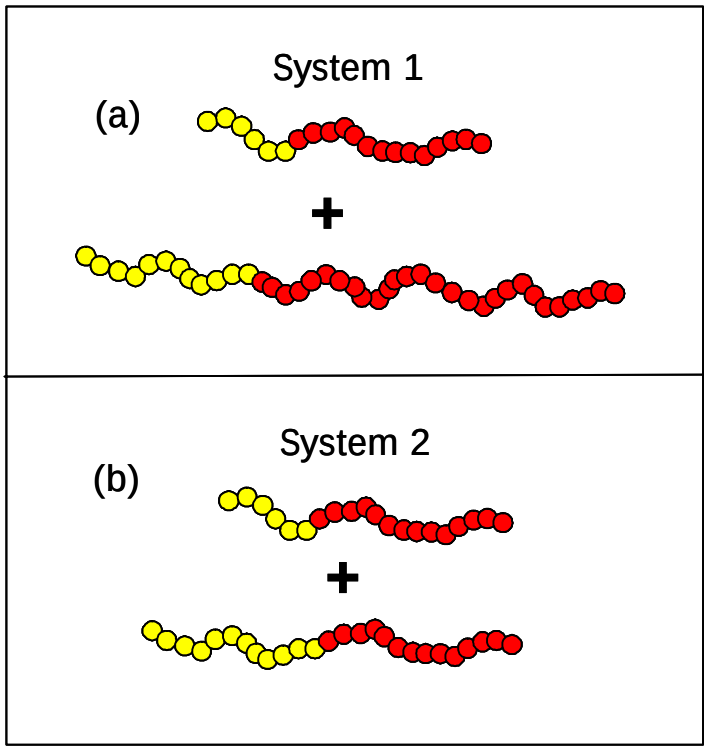

Figure 1.10. Cartoon representing the two model systems studied with a bidisperse distribution of components. (a) System 1: 90 % chains with N = 20 and 10 % chains with N= 40, the volume fraction of minority block in both components is $f = 0.30$. (b) System 2: 90 % of the original $f = 0.3$ chains with N = 20, mixed with f = 0.46 chains (N = 26). Thus, in System 2 the overall minority component fraction is $f_{all} = 0.316$.

N = 26 and f = 0.4615 (12 beads of minority component). System 2 was studied to test if just making longer the block of the minority component was enough to reduce packing frustration (note that for System 2 the overall composition is f = 0.3162). Simulations were performed around the same temperature where G was found (β = 0.11111, χN~ 40). No attempt was made to "optimize" the bidisperse systems compositions.

After equilibration, the G phase was also found in both systems with a unit cell size of 35 lattice units (in the pure melt the unit cell was 33 lattice units). In each system, the appropriate simulation box dimensions were estimated using $S(\mathbf{q})$ together with equation 6, as explained in the Section on simulation details. To see if there was actually segregation between longer and shorter chains, we calculated the intermolecular bead-to-bead radial distribution function for the minority component. As can be seen in Figure 1.11, in both systems the longer chains aggregate more than the shorter chains. This is evident in the stronger short-range correlations (i.e., higher peak) observed in the radial distribution function of the longer chains. We also examined the hypothesis that this aggregation leads to a spatially correlated segregation wherein the minority component blocks of the longer chains reside preferentially inside the Gyroid nodes. Figure 1.12 shows a typical snapshot of the system where only the minority component blocks are shown; the longer chains are "painted" in red and the shorter chains in yellow. As can be seen in Figure 1.12, most of the longer chains are indeed found inside the nodes, thus corroborating the hypothesis. This was true for both systems studied (results for other snapshots lead to similar conclusions).

To investigate how bidispersity affects packing in the Gyroid nodes, selected typical configurations were used to obtain concentration profiles of "voids" (smoothed out as described in the Section on simulation details). To estimate the mean void

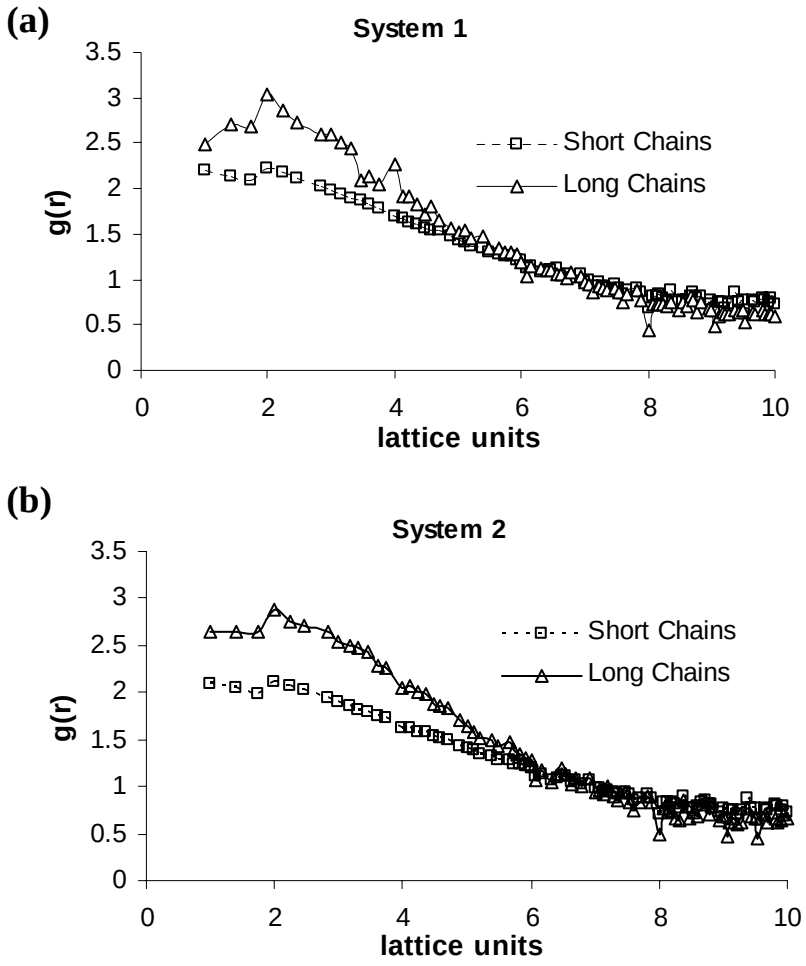

Figure 1.11. Intermolecular bead-to-bead radial distribution functions for the minority component. (a) System 1 [$g(r)_{max}$=3.04]. (b) System 2 [$g(r)_{max}$=2.89]. The stronger short-range correlation in the longer chains indicates some degree of clustering (aggregation) beyond what is observed in the shorter chains.

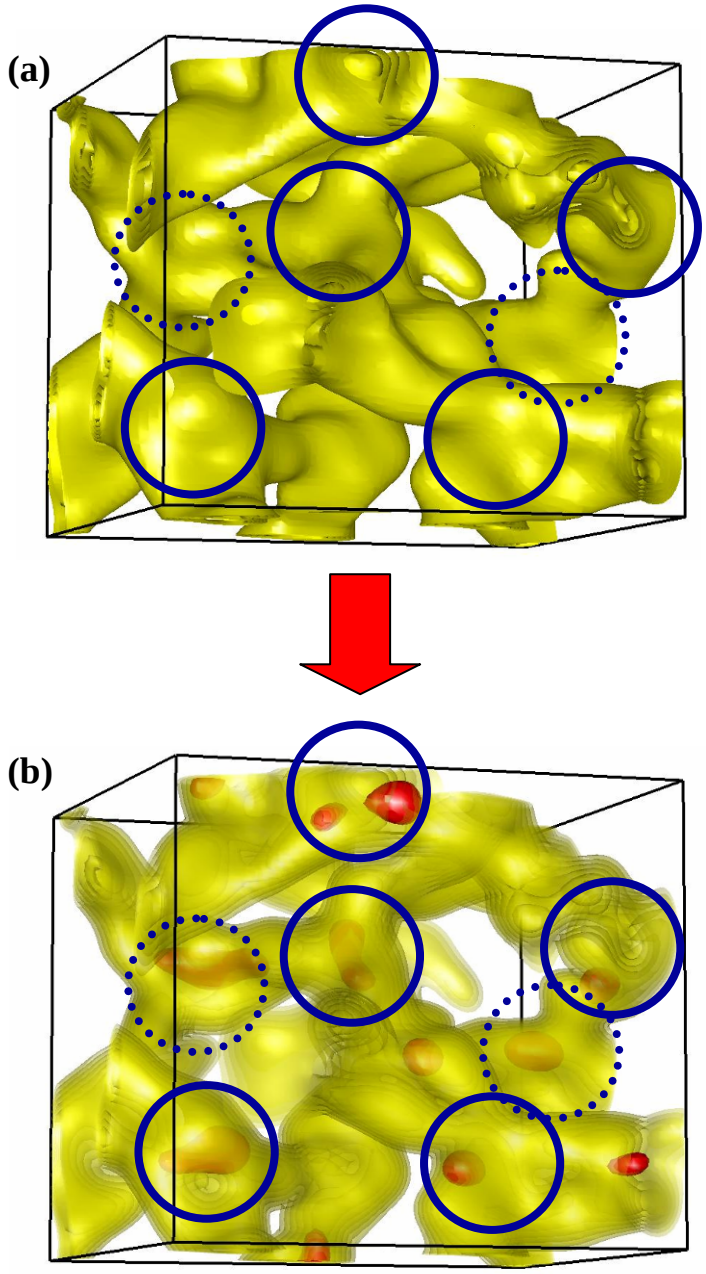

Figure 1.12. Snapshot of the Gyroid phase before (a) and after (b) “painting” in red the longer chains and making the structure semi-transparent. Shorter chains are kept in yellow and only the minority component is shown. Longer chains tend to reside in the nodes.

fraction inside the nodes, η_{node}, averages were obtained inside regions of space delimited by spheres of radius r_{cut} centered at the innermost point in the nodes. It is expected that the value of η_{node} will strongly depend on the choice of r_{cut}; a larger r_{cut} will give a η_{node} consistent with the *global* void fraction ($\eta = 0.25$) while a smaller r_{cut} will give a η_{node} representative of the *local* void fraction at the node center. In Figure 1.13, η_{node} values for the monodisperse system and the bidisperse System 1 are plotted as a function of r_{cut}. As can be seen, η_{node} values for small r_{cut} (i.e., highly localized at the center) for the bidisperse system are consistently smaller than those for the monodisperse system; this suggests that packing frustration in the former has been reduced relative to that in the latter (where vacancies concentrate in the node center). However, the results shown in Figure 1.13 should only be taken as qualitative trends, given the significant density fluctuations in the Gyroid nodes and the difficulty of unambiguously defining node centers. A different, indirect quantification of the effect of bidispersity on packing frustration is discussed next.

If the segregation of the longer chains to the nodes is indeed stabilizing the Gyroid phase, then the latter could in principle be stable in a wider region of the phase diagram. To test this idea, we ran simulations of both model systems at temperatures where Cylinders were stable; i.e., at temperatures immediately above ($\chi N \sim 30$) and below ($\chi N \sim 50$) the region where the G phase was initially found (See Fig. 1.5). At the higher temperature (lower χN), we found that again the Cylinder phase (not G) was stable, i.e., we did not detect widening of the G phase window in the region of higher temperatures. On the other hand, when we explored regions of lower temperature we found that while in System 2 the Cylinders were still stable, in System 1 the Gyroid was stable (Figure 1.14). Hence, we found that in System 1 the G phase became stable in a wider region of temperatures in the phase diagram, consistent with the idea that segregation of longer chains to the nodes reduces packing frustrations and

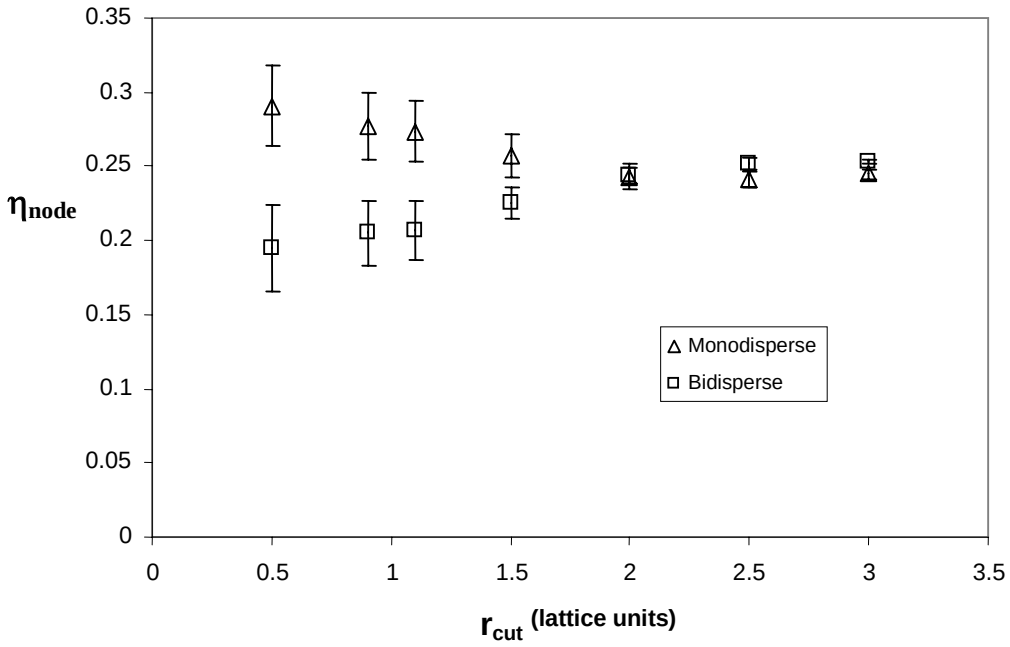

Figure 1.13. Mean void fraction η_{node} inside the Gyroid nodes as a function of the radius (r_{cut}) of the spherical region around the node center. Values of η_{node} are the average void fraction over all the volume inside such a spherical region, and for all the nodes in selected configurations of a given system.

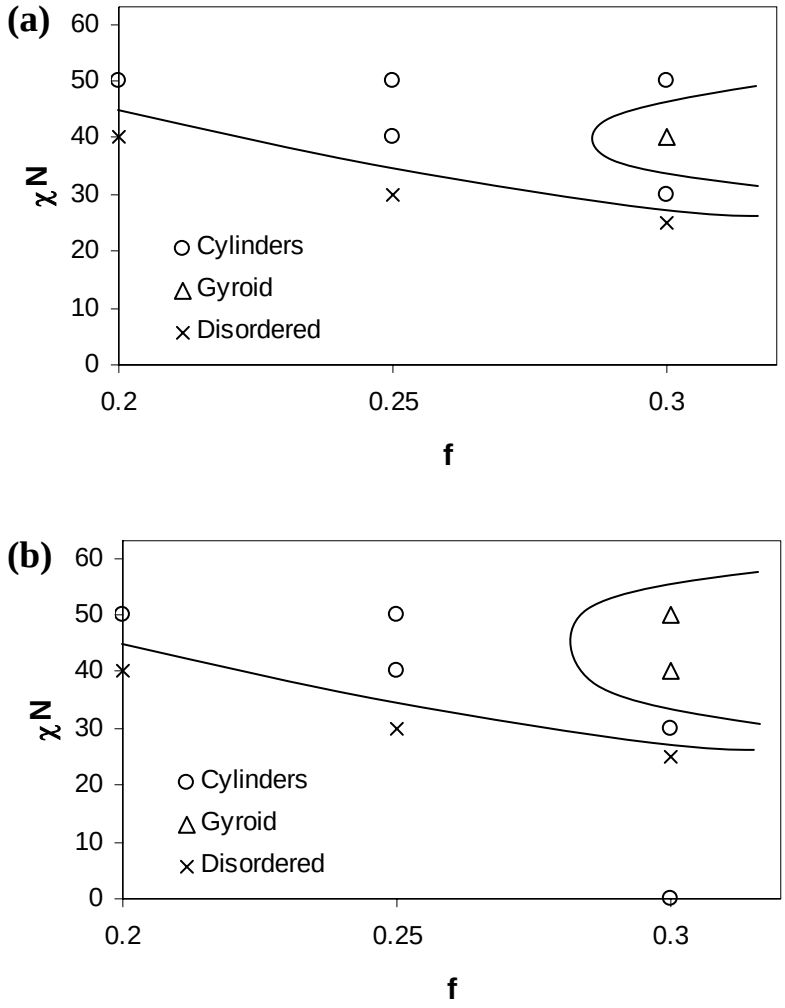

Figure 1.14. Effect of bidisperse distribution of chain lengths on Gyroid stability. (a) Zoom-in of phase diagram for the pure melt in region of Gyroid stability. (b) Modified phase diagram for the bidisperse mixture (System 1), the region of stability of G increases to lower temperature. Lines are only guides to the eye.

therefore stabilizes the structure. This is a significant effect, considering that only a very small amount of longer chains was added (a volume fraction of 10 % actually corresponds to a mole fraction of about 5 % of longer chains). It is unclear at this point why System 1 provides better stabilization of the G phase than System 2, while both system exhibit comparable extents of long-chain nodal segregation, it is possible that a longer majority block (in the long chains of System 1) may also provide added stability to the structure surrounding the node. In both systems, however, we did not find stabilization of the G phase in composition space, since we did not obtain this structure when we ran simulations at volume fractions $f = 0.25$ and $f = 0.35$ (i.e., compositions adjacent to the f where the G phase was found for the monodisperse system).

IV. CONCLUSIONS

We have mapped out the phase diagram of pure diblock melts using Canonical Monte Carlo simulations of a coarse-grained lattice model of the block copolymer chains. As expected, we found that the diblocks assembled into the classical morphologies of Lamellae, Cylinder and Spheres depending on the values of block composition (f) and χN. In a small region of the intermediate segregation regime (i.e., at $\chi N \sim 40$ and $f \sim 0.30$) the bicontinuous Gyroid phase was found to be thermodynamically stable. Also, a co-continuous structure that bears some resemblance to the O^{70} phase was encountered between the L and G phase (i.e., at $\chi N \sim 40$ and $f \sim 0.35$). To the best of our knowledge, this work constitutes the first time the Gyroid phase has been simulated for systems of pure diblock melts; the range of compositions and temperatures in which this phase is stable was found to be very narrow. The periodicity of the G phase in the three directions makes it especially sensitive to the choice of simulation box size. As a consequence, other phases like

Cylinders and Perforated Lamellae were also found at the same thermodynamic conditions when the simulation box was not of the right size to fit an integer number of Gyroid unit cells. However, such alternative phases were shown to be metastable, since they presented higher values of chemical potential and did not remain stable in larger simulation boxes. Concentration profiles of the minority component blocks revealed the presence of low concentration regions and the absence of chain stretching inside the Gyroid nodes. The low concentration regions cause an entropic packing frustration, henceforth limiting the stability of the G phase in the phase diagram.

We also studied mixtures of block copolymers with chain length bidispersity to test the hypothesis that this kind of systems can stabilizes the Gyroid phase (as suggested by Hasegawa et al.[30]). The intermolecular bead-to-bead radial distribution function showed that longer chains tend to aggregate more than the shorter chains. Moreover, analysis of configurations of the system revealed that the longer chains reside preferentially in the nodes of the Gyroid, and fill up better the node centers (i.e., a reduction of packing frustration). Finally, we found that for one of the systems studied with chain length bidispersity (System 1), the Gyroid phase is indeed stable in a wider range of temperatures than in the pure diblock melt. This result supports the idea that chain length bidispersity can be used as an effective means to stabilize the G phase. In principle, optimal bidisperse compositions could be found to maximize such an effect.

Several well-known limitations are associated with the simplified lattice model adopted here; e.g., the highly coarse-grained nature of the packing and energetic interactions. Furthermore, it should be noted that experiments are usually performed at constant pressure (P), while simulations in this work were performed at constant density (ρ) because of the difficulties associated with performing constant P simulations in lattice systems. Although most theories and simulations are also carried

out at constant ρ, we expect[44] that for chains of finite size, the two different phase diagrams (constant ρ and constant P) can become significantly different. Simulations of block copolymers in the continuum space could be used to determine the importance of this effect.

ACKNOWLEDGEMENTS

This work was partially supported by the ACS Petroleum Research Fund. Additional support from the US Department of Energy, Grant No. DE-FG02-05ER15682 is gratefully acknowledged. The authors are also grateful to Prof. U. Wiesner (MSE, Cornell University) for several stimulating discussions.

REFERENCES

1. Hamley, I. W., *The Physics of Block Copolymers*. Oxford University Press: **1998**.

2. Hajduk, D. A.; Harper, P. E.; Gruner, S. M.; Honeker, C. C.; Kim, G.; Thomas, E. L.; Fetters, L. J. *Macromolecules* **1994,** 27, (15), 4063-4075.

3. Thomas, E. L.; Alward, D. B.; Kinning, D. J.; Martin, D. C.; Handlin, D. L.; Fetters, L. J. *Macromolecules* **1986,** 19, (8), 2197-2202.

4. Finnefrock, A. C.; Ulrich, R.; Toombes, G. E. S.; Gruner, S. M.; Wiesner, U. *J. Am. Chem. Soc.* **2003,** 125, (43), 13084-13093.

5. Templin, M.; Franck, A.; DuChesne, A.; Leist, H.; Zhang, Y. M.; Ulrich, R.; Schadler, V.; Wiesner, U. *Science* **1997,** 278, (5344), 1795-1798.

6. Kamperman, M.; Garcia, C. B. W.; Du, P.; Ow, H. S.; Wiesner, U. *J. Am. Chem. Soc.* **2004,** 126, (45), 14708-14709.

7. Cho, B. K.; Jain, A.; Gruner, S. M.; Wiesner, U. *Science* **2004,** 305, (5690), 1598-1601.

8. Thompson, R. B.; Ginzburg, V. V.; Matsen, M. W.; Balazs, A. C. *Science* **2001,** 292, (5526), 2469-2472.

9. Lin, Y.; Boker, A.; He, J. B.; Sill, K.; Xiang, H. Q.; Abetz, C.; Li, X. F.; Wang, J.; Emrick, T.; Long, S.; Wang, Q.; Balazs, A.; Russell, T. P. *Nature* **2005,** 434, (7029), 55-59.

10. Wang, Q.; Nealey, P. F.; de Pablo, J. J. *J. Chem. Phys.* **2003,** 118, (24), 11278-11285.

11. Matsen, M. W. *Macromolecules* **1995,** 28, (17), 5765-5773.

12. Bates, F. S.; Schulz, M. F.; Khandpur, A. K.; Forster, S.; Rosedale, J. H.; Almdal, K.; Mortensen, K. *Faraday Discuss.* **1994,** 98, 7-18.

13. Matsen, M. W.; Bates, F. S. *Macromolecules* **1996,** 29, (23), 7641-7644.

14. Matsen, M. W.; Bates, F. S. *J. Chem. Phys.* **1997,** 106, (6), 2436-2448.

15. Fredrickson, G. H.; Ganesan, V.; Drolet, F. *Macromolecules* **2002,** 35, (1), 16-39.

16. Matsushita, Y. *J. Polym. Sci., Part B: Polym. Phys.* **2000,** 38, (12), 1645-1655.

17. Hamley, I. W.; Podneks, V. E. *Macromolecules* **1997,** 30, (12), 3701-3703.

18. Dotera, T. *Phys. Rev. Lett.* **2002,** 89, (20), 205502.

19. Larson, R. G. *J. Phys. II (Paris)* **1996,** 6, (10), 1441-1463.

20. Rychkov, I.; Yoshikawa, K. *Macromol. Theory Simul.* **2004,** 13, (3), 257-264.

21. Gonzalez-Segredo, N.; Coveney, P. V. *Europhys. Lett.* **2004,** 65, (6), 795-801.

22. Matsen, M. W. *J. Chem. Phys.* **1998,** 108, (2), 785-796.

23. Starr, F. W.; Schroder, T. B.; Glotzer, S. C. *Phys. Rev. E* **2001,** 6402, (2).

24. Horsch, M. A.; Zhang, Z. L.; Iacovella, C. R.; Glotzer, S. C. *J. Chem. Phys.* **2004,** 121, (22), 11455-11462.

25. Groot, R. D.; Madden, T. J.; Tildesley, D. J. *J. Chem. Phys.* **1999,** 110, (19), 9739-9749.

26. Schultz, A. J.; Hall, C. K.; Genzer, J. *J. Chem. Phys.* **2002,** 117, (22), 10329-10338.

27. Schultz, A. J.; Hall, C. K.; Genzer, J. *Macromolecules* **2005,** 38, (7), 3007-3016.

28. Hajduk, D. A.; Takenouchi, H.; Hillmyer, M. A.; Bates, F. S.; Vigild, M. E.; Almdal, K. *Macromolecules* **1997,** 30, (13), 3788-3795.

29. Schultz, A. J.; Hall, C. K.; Genzer, J. *J. Chem. Phys.* **2004,** 120, (4), 2049-2055.

30. Hasegawa, H.; Hashimoto, T.; Hyde, S. T. *Polymer* **1996,** 37, (17), 3825-3833.

31. Dotera, T.; Hatano, A. *J. Chem. Phys.* **1996,** 105, (18), 8413-8427.

32. Larson, R. G. *Macromolecules* **1994,** 27, (15), 4198-4203.

33. Frenkel, D.; Smit, B., *Understanding Molecular Simulation*. Academic Press: San Diego, CA, 2002.

34. McGreevy, R. L., *Computer Modeling in Inorganic Crystallography*. Academic Press: San Diego, CA, 1997.

35. Schultz, A. J.; Hall, C. K.; Genzer, J. *Macromolecules* **2007,** 40, (8), 2629-2632.

36. Groot, R. D.; Madden, T. J. *J. Chem. Phys.* **1998,** 108, (20), 8713-8724.

37. Tyler, C. A.; Morse, D. C. *Phys. Rev. Lett.* **2005,** 94, (20), 208302.

38. Epps, T. H.; Cochran, E. W.; Hardy, C. M.; Bailey, T. S.; Waletzko, R. S.; Bates, F. S. *Macromolecules* **2004,** 37, (19), 7085-7088.

39. Vassiliev, O. N.; Matsen, M. W. *J. Chem. Phys.* **2003,** 118, (16), 7700-7713.

40. Fredrickson, G. H.; Helfand, E. *J. Chem. Phys.* **1987,** 87, (1), 697-705.

41. Matsen, M. W. *J. Phys.: Condens. Matter* **2002,** 14, (2), R21-R47.

42. Bendejacq, D.; Ponsinet, V.; Joanicot, M.; Loo, Y. L.; Register, R. A. *Macromolecules* **2002,** 35, (17), 6645-6649.

43. Sides, S. W.; Fredrickson, G. H. *J. Chem. Phys.* **2004,** 121, (10), 4974-4986.

44. Escobedo, F. A.; de Pablo, J. J. *Macromolecules* **1999,** 32, (3), 900-910.

CHAPTER 2

SIMULATION OF THE GYROID PHASE IN OFF-LATTICE MODELS OF PURE DIBLOCK COPOLYMER MELTS*

I. INTRODUCTION

The study of block copolymers constitutes an active area of research.[1-5] The attractive feature of these systems is that they can self assemble at the nanoscale to yield structures of specific geometry with long range order.[6] Furthermore, the specific morphology can be rationally controlled using the appropriate experimental conditions. For example, in surfactant-like diblock copolymer (DBC) solutions the concentration of a selective solvent can be varied to yield different morphologies. In the case of pure DBC melts, the volume fraction of one block relative to the other controls the resulting morphology. The structures that can be found in such DBC melts can be grouped as 1) Classical: like Spheres in BCC packing (S), Cylinders Hexagonally Packed (C), and Lamellar phase (L), and 2) Complex: like the Bicontinuous Gyroid phase (G).[7, 8] The Perforated Lamella (PL) phase, a morphology often observed, is believed to be a long-lived metastable state in the bulk,[9] though it can be stable in thin DBCs films.[10,11] Recently, Tyler and Morse[12] predicted using self-consistent field theory (SCFT) that a co-continuous phase O^{70} is stable in a very narrow region of the DBC melt phase diagram.

The Gyroid phase is especially interesting among all the other morphologies found in DBC melts. From a practical point of view, its interconnectivity and periodicity in the three directions makes it a good candidate as a precursor of porous

* Reprinted with permission from Martinez-Veracoechea, F. J.; Escobedo, F. A. *J. Chem. Phys.*, 25, (10), 104907, **2006**.

materials with high contact surface,[13] high conductivity nanocomposites, and other specialty applications. From a theoretical point of view, the study of the G phase has encountered many difficulties and even now there remain some open questions about the causes of its limited stability in the DBC melt phase diagram.

Due to its relative simplicity, the DBC melt system has become a popular test bed for both experimental[9, 14] and field-theoretic[15-19] research. In addition, the interplay between DBC and nanoparticles has been extensively studied by Balazs et al.[20-23] Although many of the issues regarding the phase behavior of DBC melts have been resolved via mean-field SCFT[5, 16] using highly coarse-grained mesoscopic models, some open questions remain concerning the effect of finite chain length size and local density fluctuations on the phase diagram and the detailed structure of the Gyroid nodes, for example, for which more "microscopic" approaches are needed. While in principle field-theoretic (e.g., SCFT) calculations could be implemented with the desired "microscopic" resolution required to address these issues,[24] this is non-trivial and the more straightforward particle-based approaches are adopted here (despite their higher computational cost). In fact, numerous particle-based molecular simulations have already been devoted to the study of DBC melt systems. Nonetheless, particle-based simulation work devoted to the G phase in DBC melts is relatively scarce.

Most published particle-based simulation results about the G phase are restricted to systems with implicit selective solvent. Larson[25] found the G phase in lattice Monte Carlo (MC) simulations of surfactants in a selective solvent. Yu et al.[26] studied the cylinder-gyroid-lamella transitions in selective solvent DBC solutions also using lattice MC. González-Segredo and Coveney[27] studied the G phase in a system of surfactants in selective solvent using Lattice-Boltzmann. Rychkov and Yoshikawa[28-30] also found the G phase in a system of block copolymers in selective solvent using

Molecular Dynamics (MD). Very recently, Iacovella et al.[31] observed a G phase with crystalline nodes in polymer-tethered nanospheres systems using Brownian Dynamics (BD) and a model similar to that of Rychkov and Yoshikawa. On the other hand, in most simulation studies of pure DBCs in melt conditions, the G phase was not observed. Examples are the BD simulations of Horsch et al.,[32] the Discontinuous Molecular Dynamics (DMD) simulations of Schultz et al.,[33, 34] and the Dissipative Particle Dynamics with chains of soft spheres of Groot et al.,[35-37] where only "classical" morphologies and the meta-stable PL phase were observed. The G phase has been observed in lattice melts by Dotera et al.[38] but these simulations were for triblock copolymers where the expected range of stability of the G phase is wider than in the case of diblocks.[12] Relative to solvent implicit DBC solutions where chains have some freedom to move, the high density of melt systems leads to slower dynamics and higher computational costs. Moreover, it has also been suggested that the addition of selective solvent or small amounts of homopolymer stabilizes the formation of the G phase[39] therefore facilitating its simulation.

In a previous work,[40] we simulated the G phase in DBC melts using lattice MC. We found that the formation of the G phase was especially sensitive to the selection of simulation box size. This effect, also observed by Dotera et al.,[38, 41] is a consequence of the fact that block copolymer microphases present long range periodicity. Therefore, to obtain these phases in simulation boxes with periodic boundary conditions, the box size needs to be an integer multiple of the unit cell size. Structures with periodicity in only one or two dimensions (e.g., the L and C phases, respectively) are able to rotate within the simulation box to accommodate themselves consistently with the periodic boundary conditions. On the other hand, the G phase (periodic in the three directions) becomes severely frustrated for inappropriate sizes of the simulation box. When this frustration is present, other phases may be artificially

stabilized. In our previous work[40] we also examined the suggestion that the reason for the limited stability of the G phase in the DBC melt phase diagram was the existence of packing frustration of chain segments in the interior of the Gyroid nodes;[42, 43] e.g., we found that the addition of a small amount of 40-mer chains to a 20-mer DBC system led to a more uniform filling of such nodes (where 40-mers concentrate) and to an increased temperature range of G phase stability.[40]

In this paper, we use Molecular Dynamics and Monte Carlo methods to study the behavior of a bead-spring model for the DBC chains in the region where the G phase is expected to form. This model (to be referred to as *Model* 1) consists of chains of soft repulsive particles typically used with traditional Dissipative Particle Dynamics (DPD).[44] We show that for such a particle-based (continuum-space) model the G phase can be simulated in the melt state provided that the simulation box size is commensurate with the G lattice spacing. We outline an approximated phase diagram wherein stability between phases is discerned by estimation of the Helmholtz free energy for the different competitive phases. To rule out model-specificity on G phase formation, we also conducted targeted simulations of an alternative model (*Model* 2) that consists of chains of particles interacting via the Soddemann potential energy function[45] for amphiphilic molecules. Finally, we find evidence of packing frustration inside the G nodes in the form of chain stretching, whose extent is analyzed in the context of the different chain models employed.

II. METHODS

A. Molecular Dynamics via Dissipative Particle Dynamics

In the MD-DPD method the system of particles evolves according to Newton's equations of motion. The force acting in a particle is given by the sum of the conservative, random, and frictional (dissipative) forces,

$$\mathbf{F}_{ij} = \mathbf{F}^{\mathbf{C}}{}_{ij} + \mathbf{F}^{\mathbf{R}}{}_{ij} + \mathbf{F}^{\mathbf{D}}{}_{ij} = -\mathbf{F}_{ji} \tag{7}$$

to sample correctly the *NVT* ensemble it has been shown[37, 46] that the random and dissipative forces must be given by the following form,

$$\begin{aligned} \mathbf{F}^{\mathbf{R}}{}_{ij} &= \sigma\,\omega(r_{ij})\zeta\,\hat{\mathbf{r}}_{ij}/\sqrt{\delta t} \\ \mathbf{F}^{\mathbf{D}}{}_{ij} &= -\frac{1}{2}\sigma^2\left(\omega(r_{ij})\right)^2\left(v_{ij}\cdot r_{ij}\right)\hat{\mathbf{r}}_{ij}/kT \end{aligned} \tag{8}$$

where r_{ij} and v_{ij} represent, respectively, the relative distance and velocity between particles i and j, σ is the amplitude of the noise (in this work $\sigma = \sqrt{2}$), ζ is a random variable of zero mean and variance 1 and k is Boltzmann's constant. The functional form of the weighting function $\omega(r)$ is not pre-specified and it just represents the range of interaction of the random and dissipative forces. Here we follow the suggestion made by Soddemann et al.[47] where the weighting function can be given by,

$$\omega(r) = \begin{cases} 1 & if\ r \le r_c \\ 0 & if\ r > r_c \end{cases} \tag{9}$$

Soddemann et al.[47] pointed out that the choice of the conservative force does not depend on the DPD method itself but in the model fluid under consideration. Hence, we take the point of view that the DPD method is just a convenient thermostat to do MD in the canonical ensemble. As a consequence, the particular form of the conservative force $\mathbf{F}^{\mathbf{C}}$ is going to depend upon the model under consideration and will be considered explicitly later in the *Models* Section.

The numerical integration of the DPD equations of motion presents the difficulty that the dissipative force depends explicitly in the velocity. Therefore, direct implementation of the velocity-Verlet algorithm[44] is not possible. Although many sophisticated algorithms have recently been proposed to integrate the DPD equations,[48, 49] we adopted here the simple modification of the velocity-Verlet

algorithm proposed by Groot et al.[35-37] In this scheme, the equations of motion are integrated numerically according to,

$$\begin{aligned} r(t+\delta t) &= r(t) + v(t)\delta t + \tfrac{1}{2} F(t)\delta t^2 \\ \overline{v}(t+\delta t) &= v(t) + \alpha f(t)\delta t \\ F(t+\delta t) &= F\left(r(t+\delta t), \overline{v}(t+\delta t)\right) \\ v(t+\delta t) &= v(t) + \tfrac{1}{2}\left(F(t) + F(t+\delta t)\right)\delta t \end{aligned} \tag{10}$$

where α is an adjustable parameter that permits controlling the temperature. Similar to what was found by Groot et al., we observed that the target temperature was best achieved if $0.6 \leq \alpha \leq 0.65$. The choice of the value of δt is particular to the model.[48, 50] As expected, the integration step size choice is a compromise between computational efficiency and temperature control and thermodynamic consistency.

B. Monte Carlo Simulation of Chemical Potentials

At some thermodynamic conditions, more than one morphology can often spontaneously form depending upon the simulation box size. In the *NVT* ensemble, the most stable phase is the one with the lowest excess Helmholtz free energy per unit chain (βa^{ex}), where the "excess" properties are defined by taking as reference the ideal chain (i.e., a chain having only bonded interactions). The excess Helmholtz energy can be evaluated from,

$$\beta a^{ex} = \beta \mu^{ex} - (Z-1) \tag{11}$$

where $\beta\mu^{ex}$ is the excess chemical potential and $Z = P/\rho_{ch}kT$ is the compressibility factor with ρ_{ch} the copolymer chains number density. For this approach to be feasible, however, quite accurate pressures and chemical potentials must be attainable. While suitable pressure values can be obtained from the pressure tensor calculated in the DPD simulations, chemical potential evaluation is better suited to Monte Carlo

methods. Because the chemical potential for long chain molecules in dense systems is difficult to simulate via the test-particle insertion method[44] (even with configurational-bias sampling), we propose a novel variant of an expanded-ensemble (EXE) method[51, 52] that gradually couples-decouples a target chain in the system by appending/deleting beads to/from it. This method requires a means for accurate estimation of the free-energy differences associated with such growth/reduction transitions, and the use of suitable biasing weights to attain efficient sampling of all transitions; we adopt here Bennett's acceptance-ratio method[53] to estimate free-energy differences and the method of Trebst et al.[54] to get the biasing weights.

The partition function for an expanded-ensemble with M macrostates is given by:

$$Q_{EXE} = \sum_{m=1}^{M} \exp(\psi_m)\, Q(\lambda_m) \tag{12}$$

where $Q(\lambda_m)$ in our case is the partition function of the *NVT* ensemble with characteristic parameter λ_m, and ψ_m is an arbitrary bias weighting function. The system visits the macrostates with marginal probability

$$\Pi_{\psi}(\lambda) = \exp[\psi(\lambda)]\, Q(\lambda) / Q_{EXE} \tag{13}$$

For a copolymer system with N_{ch} chains of length N and for λ_m macrostates defined by the variable number of beads N_m of an additional chain in the system, to be denoted as the λ-chain; transitions between macrostates thus correspond to changes in N_m. If the growth/reduction attempts are proposed with equal probability, the Metropolis acceptance criterion for a macrostate transition $m \rightarrow m+\Delta$ performed with configurational-bias sampling is:

$$P_{acc} = \min\{\, 1, \exp(-\vartheta + \psi_{m+\Delta} - \psi_m)\} \tag{14}$$

where

$$-\mathcal{G} = \Delta \ln W(m \to m+\Delta) = \Delta \ln \left(\prod_{i=N_A}^{N_B} n_{sp}^{-1}(i) \sum_{j=1}^{n_{sp}(i)} \exp[-\beta U_j(i)] \right) \tag{15}$$

where W is the Rosenbluth weight[44] associated with the corresponding growth/reduction process, $\Delta = +1$ for growth, $\Delta = -1$ for reduction, $N_A = 1+\min(N_m, N_{m+\Delta})$, $N_B = \max(N_m, N_{m+\Delta})$, $n_{sp}(\mathrm{i})$ is the number of trial positions of the ith chain segment (sampled according to the underlying *bonded* potential), and $U_j(i)$ is the *non-bonded* interaction energy between the ith segment (at the jth trial position) and the system.

The Helmholtz free-energy differences associated with the *un-weighted* transitions between λ-states can be estimated using Bennett's acceptance ratio formula:

$$\beta A(\lambda_{m+1}) - \beta A(\lambda_m) \equiv \ln \frac{Q(\lambda_m)}{Q(\lambda_{m+1})} = C - \ln \frac{\ell_{m+1,m}}{\ell_{m,m+1}} \tag{16}$$

where $\ell_{m,m+1}$ is the number of trial transitions $\lambda_m \to \lambda_{m+1}$ and C is found from:

$$\sum_m \left(1 + \exp\left[\mathcal{G}(\lambda_m \to \lambda_{m+1}) - C\right]\right)^{-1} = \sum_{m+1} \left(1 + \exp\left[\mathcal{G}(\lambda_{m+1} \to \lambda_m) + C\right]\right)^{-1} \tag{17}$$

where $\sum_m$ denotes a sum over all transitions attempted (as indicated in $\mathcal{G}$) started at macrostate λ_m. The excess chemical potential associated with the insertion of a whole chain into the system is:

$$\beta\mu^{ex}(\lambda_1 \to \lambda_M) = [\beta A(\lambda_M) - \beta A(\lambda_1)] / \Delta N_{ch} = \sum_{m=1}^{M-1} \left[\beta A(\lambda_{m+1}) - \beta A(\lambda_m)\right] \tag{18}$$

Where $\Delta N_{ch}=1$. Because Bennett's method uses information of the un-weighted transitions between λ-states, [i.e., the $\beta A(\lambda_m)$ estimates do not depend explicitly on the ψ weights used, even though the actual transitions occur according to Eq. (14)], one can use in Eqs. (16)-(17) data accumulated over the entire run. This renders the

calculation much more efficient than the visited-states method typically employed[55, 56] and minimizes user intervention.[57-59]

It has been customary to assume that efficient sampling of all λ-states is best achieved by making Π_ψ in Eq. (13) a uniform distribution, in which case it follows that the weights would be directly related to the free energy differences, i.e., $\psi_m \sim \beta A(\lambda_m)$. However, this approach has been shown to provide a suboptimal means to sample the important (transitional) regions of the λ domain.[54] We therefore adopt here the method of Trebst et al.[54] which chooses the ψ weights such that the number of round trips (per CPU time) between the lowest λ (=1) and highest λ (=M) states is maximized. In our application, this should accelerate the convergence of the chemical potential calculation (reduction of statistical errors) by maximizing the times that the λ-chain *disappears from* and *reappears in* different places of the simulation box. Trebst et al. method relies in maximizing the steady-state "current" j with which the "walker" (i.e., the λ-chain) goes from λ=1 to λ=M estimated from:

$$j = D(\lambda)\,\Pi(\lambda)\frac{dx(\lambda)}{d\lambda} \tag{19}$$

where $D(\lambda)$ is the walker's diffusivity at state λ and $x(\lambda)$ is the fraction of times that the walker at state λ has had a label "+". The walker's label is assigned depending on the extreme λ-state that it visited last: if the most recent extreme-state visited was λ=1 (i.e., fully deleted chain) the walker's label becomes "–"; on the other hand, if the most recent visit was to λ=M (i.e., fully grown chain) the label becomes "+". Trebst et al. recipe for maximizing the current dictates that the optimal probability of visiting a given λ-state is given by: [54]

$$\Pi_{\psi'}(\lambda) \propto [D(\lambda)]^{-1/2} \propto \sqrt{\Pi_\psi(\lambda)\frac{d\,x(\lambda)}{d\lambda}} \tag{20}$$

To find the optimal weights ψ' that correspond to this probability distribution, we resort to Eq. (13) and use the fact that $Q(\lambda) \propto \exp[-\beta A(\lambda)]$ to arrive at the iteration formula:

$$\psi'(\lambda) = \beta A(\lambda) + \frac{1}{2}\ln\left(\Pi_{\psi}(\lambda)\frac{d\,x(\lambda)}{d\lambda} \right) \tag{21}$$

where $\beta A(\lambda)$ is to be estimated from Bennett's formula (16) [a Transition matrix approach] and the factor $\Pi_{\psi}(\lambda)\, dx(\lambda)/d\lambda$ is estimated from the statistics collected for the previously used weights ψ [a visited-states approach]. Since initially the weights are unknown, an iterative scheme is needed to gradually refine them. In practice, we start by using rough estimates of $\beta A(\lambda_m)$ from Bennett's method as the initial weights ψ_m and then perform two or three iterations with Eq. (21) to refine the optimal weights. Note that Eq. (21) is different from the prescription given by Trebst et al. [i.e., Eq. (13) in Ref. 54] in that we here take advantage of the accurate estimations of $\beta A(\lambda)$ afforded by Bennett's method which are unaffected by the iterations [unlike what happens in the estimation of $\Pi_{\psi}\, dx(\lambda)/d\lambda$, the statistics needed in Eq. (16)-(17) are never re-zeroed after an iteration].

During the calculation of the chemical potential the systems were evolved using standard continuum MC sampling in the *NVT* ensemble. For this purpose, the configurations equilibrated with DPD were used as input for the MC runs, using the same potential energy model underlying the DPD simulations. A typical MC run consisted of 10^6 cycles, each cycle comprising 3 attempted transitions of the λ-chain and N_{tot} (equal to the number of beads in the system) attempted relaxation moves with 5% translations, 5% rotations, 16% reptations, 3% switches (where a chain is repositioned upside-down), 41% hops, and 30% configurational bias moves.[44] All these moves were accepted using suitable forms of the Metropolis criterion. Transitions between λ-states were accepted using Eqs. (14)-(15) with $n_{sp}(i)$=10 $\forall$ i;

and were chosen such that $\lambda_{m+1}-\lambda_m = 1$; i.e., only one bead at a time was added or deleted. Further details about the implementation of the continuum MC can be found elsewhere.[60]

For the calculation of βa^{ex} via Eq. (5), statistical uncertainties in chemical potentials were estimated during the MC runs from the fluctuations of the plateau value of $\beta\mu^{ex}$ which was first reached at ~5×10^5 cycles (i.e., about half way the total simulation run). Uncertainties in the pressure were calculated during the DPD simulations using standard block analysis techniques[44] over production runs of 10^6 time steps ($\delta t = 0.01$) with pressure averages calculated in each of 500 blocks.

C. Models

In this work we thoroughly study a continuum model for the copolymer chains that we call "*Model* 1". In addition, to probe the model dependence of our results we briefly study an alternative continuum model that we call "*Model* 2". Since we will use as reference our previous results[40] obtained in a lattice system, we also explain that lattice model briefly. DBC chains consist of beads of two different types (e.g., A and B). Both bead types have the same size and the volume fraction f is given by the ratio between the number of minority component beads (A) and the total number of beads. Throughout this work we study chains composed by 20 beads (i.e., $N = 20$).

Model 1: Soft potential model.

This model was first used by Groot et al.[35-37] to study DBCs of length $N=10$. Here, polymers are represented by chains of soft beads connected by a harmonic potential. Each bead interacts with all the other beads through the conservative force

$$\mathbf{F}^{\mathrm{C}} = \begin{cases} -a_{ij}\left(1-r_{ij}/r_c\right)\hat{\mathbf{r}}_{ij} & if\ r_{ij} < r_c \\ 0 \quad if\ r_{ij} > r_c \end{cases} \tag{22}$$

the natural length scale of this model is r_c and therefore we set it equal to one. The term a_{ij} gives the strength of the repulsion. Beads of the same type interact with a_{ii} = 25 while

for different type beads[37] $a_{ij} \approx a_{ii} + 3.27\chi$, where χ is the Flory-Huggins interaction parameter used, as is customary in block copolymers, to quantify the degree of segregation between different species blocks. To represent melt conditions, systems are simulated at a density $\rho = 3$.

The DBC chains are formed by connecting the beads through a harmonic potential which leads to the force,

$$\mathbf{F}_{ij}^{har} = -k_h r_{ij} \hat{\mathbf{r}}_{ij} \tag{23}$$

where k_h is the spring constant (k_h = 4 in this work). In this model each soft sphere represents a coarse-grained element of polymer fluid and therefore is considered a mesoscopic model. The integration step used for this model was δt = 0.05.

Model 2: Soddemann et al. potential model

It is based on the model for amphiphilic molecules introduced by Soddemann et al.[45] Particles interact through the repulsive part of the Lennard Jones potential and species of the same type experience an additional attraction. The total potential of interaction is given by,

$$U(r) = \begin{cases} 4\left[\left(\frac{1}{r}\right)^{12} - \left(\frac{1}{r}\right)^{6} + \frac{1}{4}\right] - \phi, & r \le 2^{1/6} \\ \frac{1}{2}\phi\left[\cos(\alpha r^2 + \beta) - 1\right], & 2^{1/6} < r < 1.5 \\ 0, & r \ge 1.5 \end{cases} \tag{24}$$

where α and β are constants chosen to make the potential continuous (i.e., α = 3.1730728678 and $\beta = -0.85622864544$) and $\phi = 0$ for unlike particles while $\phi > 0$

(i.e., attractive) for like particles. The degree of attraction between like particles is regulated by varying the value of ϕ while keeping the temperature constant; hence, ϕ acts as a measure of χ. As opposed to *Model* 1 where segregation occurs through repulsion of different type particles, in this model segregation occurs thorough "attraction" between same type species.

Beads in a chain are connected via the anharmonic FENE (finite extensible non-linear elastic) spring, with a spring constant $k_f = 2.5$ and a maximum bond length $Ro = 3$. These values allow for the crossing of the polymer chains which helps accelerating the dynamics of phase formation. With this model we simulated systems of DBCs at a fixed density $\rho = 0.85$ to ensure melt conditions and an integration step of $\delta t = 0.01$. We consider that this model lies in between more "atomistic" models (i.e., those disallowing bead overlap and chain crossing) and coarser models like *Model* 1 where particles are allowed to overlap and chains to cross.

Lattice Model.

This model has been used extensively in the study of DBCs.[25, 41, 61, 62] Space is discretized in a simple cubic lattice and polymers are represented by chains of beads where each bead occupies one lattice site (the overall void fraction is kept at 25%). Bonds are only allowed between the 26th nearest neighbors of a lattice site (i.e., coordination number 26). Each bead interacts only with its neighbors with contact energies of $\varepsilon = 1$ for different-type beads and $\varepsilon = 0$ for equal-type beads. Simulations are carried out according to the *NVT* Monte Carlo scheme where a set of moves (usually hops, reptations, and switches)[40] is attempted and accepted with probability given by the standard Metropolis criterion.[44] More details about this model can be found elsewhere.[40] The lattice model is similar to *Model* 1 in that only repulsive interactions are at play, which are stronger for unlike species; it is similar to *Model* 2 in that beads have excluded volume. All three models allow chain crossing.

III. RESULTS AND DISCUSSION

A. Microphase Formation

Simulations were carried out in the intermediate segregation regime (χN~30-60) of the phase diagram in order to explore the formation of complex bicontinuous phases (i.e., the G phase). The systems were prepared in the athermal limit and then quenched to the desired temperature (i.e., $T = 1.0$ in Models 1 and 2). When we carried out simulations of *Model* 1, we typically use 5×10^6 steps to ensure equilibration. In most cases, the systems rapidly evolved to distinct morphologies and remained practically unchanged for the rest of the simulation. We observed the formation of the classical morphologies of Cylinders (C) and Lamella (L) as shown in Figure 2.1. In addition, at appropriate thermodynamic conditions and for small ranges of simulation box sizes we observed the formation of the Gyroid (G) phase. In Figure 2.2, we show eight copies of a unit cell of the G phase obtained at $f = 0.35$ and $\chi N = 50$. As expected, the minority component forms two distinct networks. Figure 2.3 shows the calculated structure factor[63] S(q) for the simulated morphology; the relative location of the peaks is consistent with the ratios expected for the G phase.[7, 64] To the best of our knowledge, these results constitute the first time that the G phase is successfully simulated in a pure DBC melt using a continuum space particle-based model.

We mentioned earlier that inappropriate choices of the size of the simulation box can artificially induce the formation of other metastable structures[38, 40] instead of the true stable morphology at a determined point of phase diagram. The appropriate size of the box for a given phase can usually be estimated with the equation,

$$L_{box} = \frac{2\pi}{q^*} m \tag{25}$$

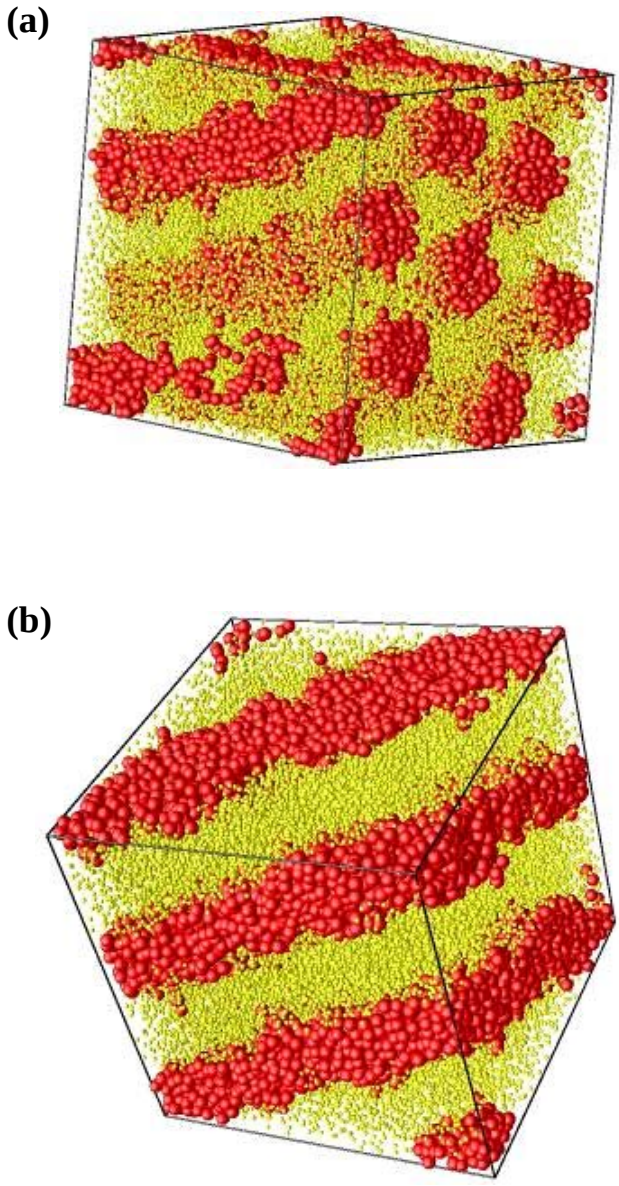

Figure 2.1. Snapshots of the classical morphologies obtained with *Model 1* showing the minority component beads in red (dark) and the majority component beads in yellow (light) at a reduced size. (a) Snapshot of the C phase observed at $f = 0.25$ and $\chi N = 50$; the hexagonal packing of the cylinders is evident. (b) Snapshot of the L phase observed at $f = 0.40$ and $\chi N = 50$.

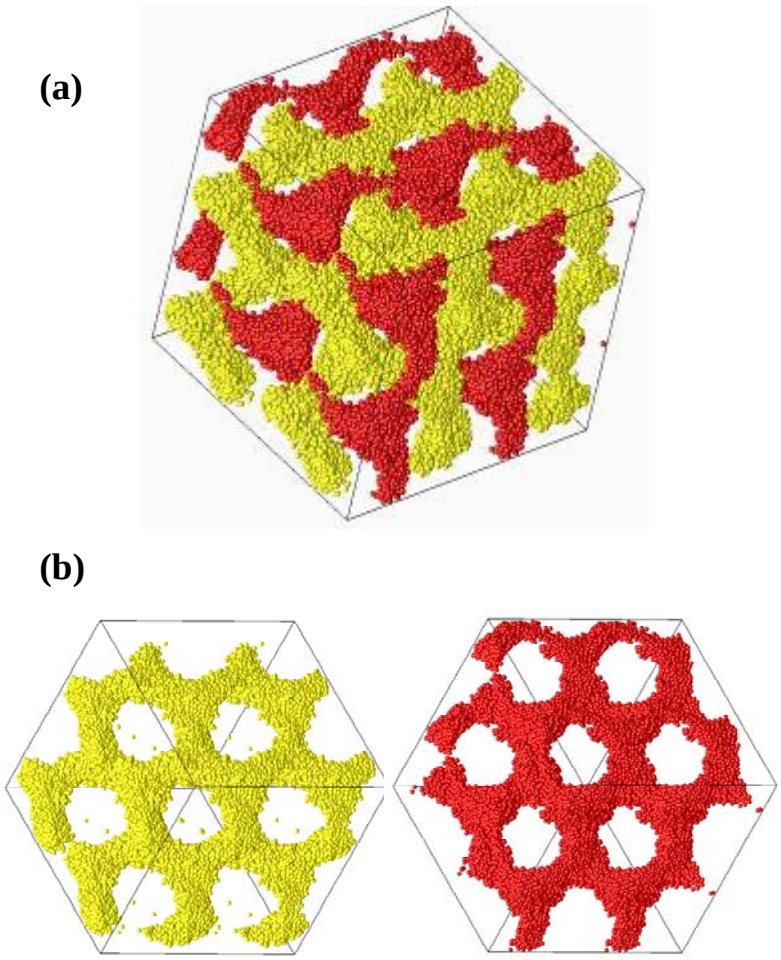

Figure 2.2. Snapshot of the Gyroid phase simulated with *Model 1* for $f = 0.35$ and $\chi N = 50$ with $L_{box} = 23$. (a) Eight (8) unit cells of the G phase seen from the 111 direction. Only the minority component is shown. The two distinct networks that never intersect are presented in red/dark and yellow/light. (b) The two distinct networks are presented separately to facilitate observation.

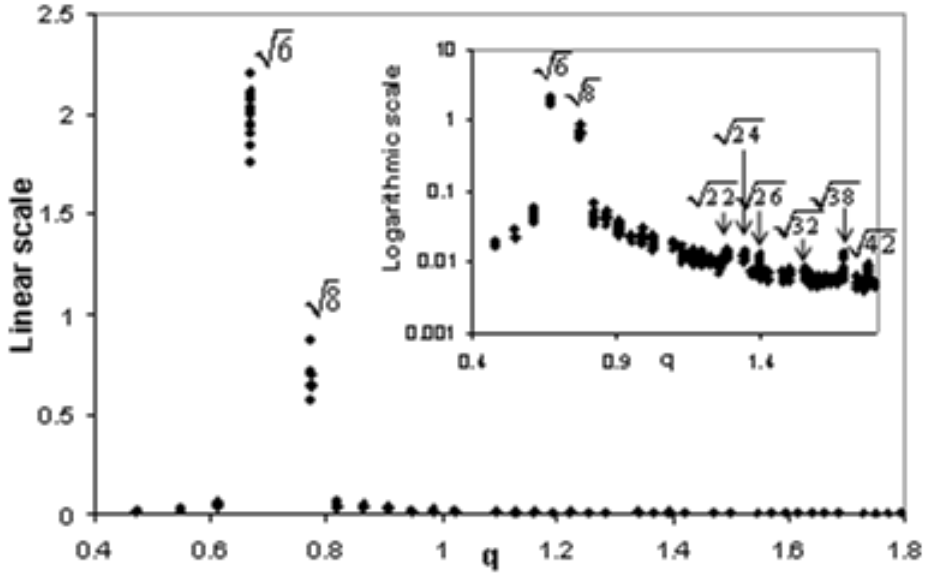

Figure 2.3. Calculated structure factor S(q) in an arbitrary linear scale for the simulated Gyroid phase snapshot presented in Figure 2.2, the inset shows S(q) in a logarithmic scale. The location of the peaks agrees with the spacing ratios expected for the G phase.[7, 64]

where q^* is the location of the first maximum in the structure factor of the system and m is the first observed reflection spacing ratio for a given periodic structure[7] (e.g., $m=1$ for Lamellae, $m=\sqrt{6}$ for the Gyroid).

In our DPD simulations we also found that at a given thermodynamic state more than one morphology could be formed depending on the simulation box size and, sometimes, the initial conditions, indicating that in some regions of the phase diagram the difference in free energy between competing morphologies is rather small. For example, at the point $\chi N = 40$ and $f = 0.30$ for simulation boxes of sizes $L_{box} = 19$, 20 or 22, the C phase is spontaneously formed after quenching. Nevertheless, for simulation boxes with size around $L_{box} = 21$ the G phase (instead of C) is automatically formed. In Figure 2.4 we present the approximate phase diagram for *Model* 1 in the intermediate segregation region for volume fractions $f \sim$ (0.25-0.40). Since we are only concerned with the bicontinuous phase, we only explored the region where the G phase is expected to be observed and its surroundings. Hence, we did not study the entire range of volume fractions where, in addition to the already observed structures, we expect to observe the Spheres (S) phase.

In the approximate phase diagram, we present for each point all the morphologies that were observed for different simulation box sizes. We have also outlined approximate phase boundaries based on the values of the excess Helmholtz free energy per molecule (βa^{ex}) obtained with the required accuracy via the methods described in section **II.B**. Table 1 shows the values of compressibility (Z), excess chemical potential ($\beta\mu^{ex}$), and excess Helmholtz free energy (βa^{ex}) for various phases at key points of the phase diagram where more than one phase was observed. The values of βa^{ex} obtained confirm that the differences in free energy between different phases at the same thermodynamic conditions can be quite small, therefore requiring accurate estimation of chemical potential values. It is important to note that our

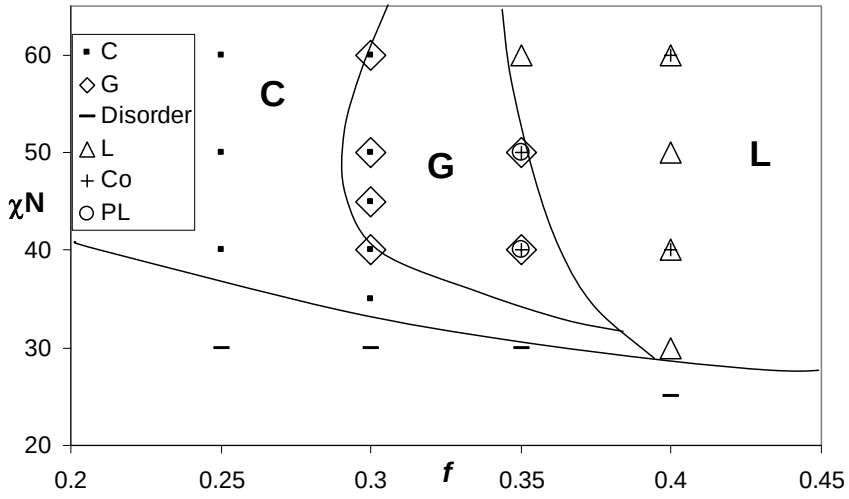

Figure 2.4. Approximate phase diagram obtained from DPD simulations of *Model* 1. Multiple symbols at a given point (set of thermodynamic conditions) are shown when more than one morphology forms for different sizes of simulation box. Based on a comparison of free energies, rough phase boundaries are outlined to guide the eye and to indicate when alternative phases are considered to be metastable. A long-lived lamellar phase with interconnecting tubes was observed at $f = 0.35$ and $\chi N = 60$, suggesting that this point is near the G-L transition.

(unreported) attempts to obtain chemical potentials by using standard configurational-bias Widom insertion methods were completely ineffective due to the prevalence of very large statistical uncertainties. Figure 2.5 shows a typical histogram of visited macrostates (i.e., number of inserted beads in the λ-chain) in a run for simulating the chemical potential of a system at $\chi N = 40$ and $f = 0.35$. As expected, the optimized ensemble methodology of Trebst et al.[54] tends to automatically concentrate the sampling to the "difficult" macrostates of the λ-chain (which in this case happen to be the beads 7-9 near the junction of the two blocks) as can be seen in the higher frequency with which those macrostates are visited.

In addition to the G phase, at $\chi N = 40$-50 and $f = 0.35$ the perforated lamella (PL) phase was also obtained (Figure 2.6). While at $\chi N = 50$ our calculated values of βa^{ex} show that the G phase is stable over the PL phase, at $\chi N = 40$ the values of βa^{ex} are practically equal (within statistical accuracy) for both phases. However, we assume the G phase to be stable since previous studies[5, 9, 17] have shown that, in pure DBC systems, the PL phase is just a long-lived metastable phase that appears at conditions where the truly stable phase is the Gyroid.

In several points of the simulated phase diagram (i.e., $f = 0.35$-40), we observed a co-continuous network (Co) phase where the minority component forms a *single* continuous network in space as shown in Figure 2.7. While a phase with these characteristics has not been observed experimentally in DBC melts thus far, Tyler and Morse[12] used Self Consistent Field Theory to predict that a co-continuous phase called O^{70} should be stable for DBC melts in a very narrow region of the phase diagram between the G and L phases. Our simulated Co phase and the O^{70} phase do present some similarities but the peaks in the structure factor S(q) of our simulated Co phase (results not shown) do not seem to coincide with the ones expected for the O^{70} phase.[12, 14, 65] However, any such comparison of S(q) is inconclusive given that in our

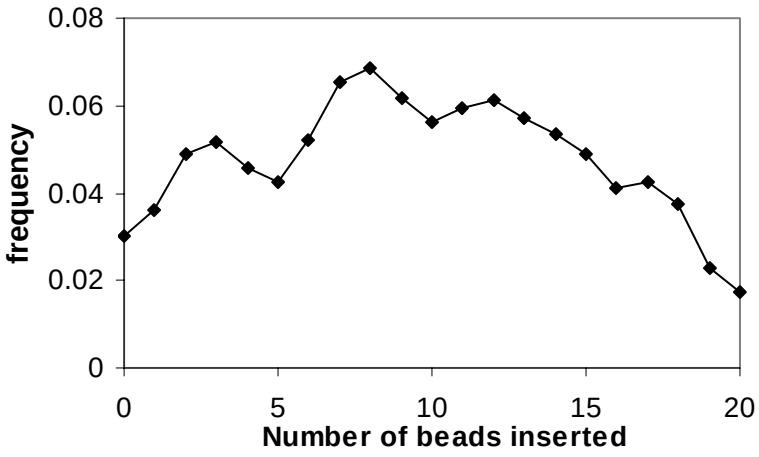

Figure 2.5. Histogram of visited macrostates during the simulation of $\beta\mu^{ex}$ via *EXE*. In maximizing the number of growth/removal cycles[54] of the target chain, the sampling is automatically concentrated on the "difficult" macrostates (i.e., those corresponding to the beads near the junction of the two blocks).

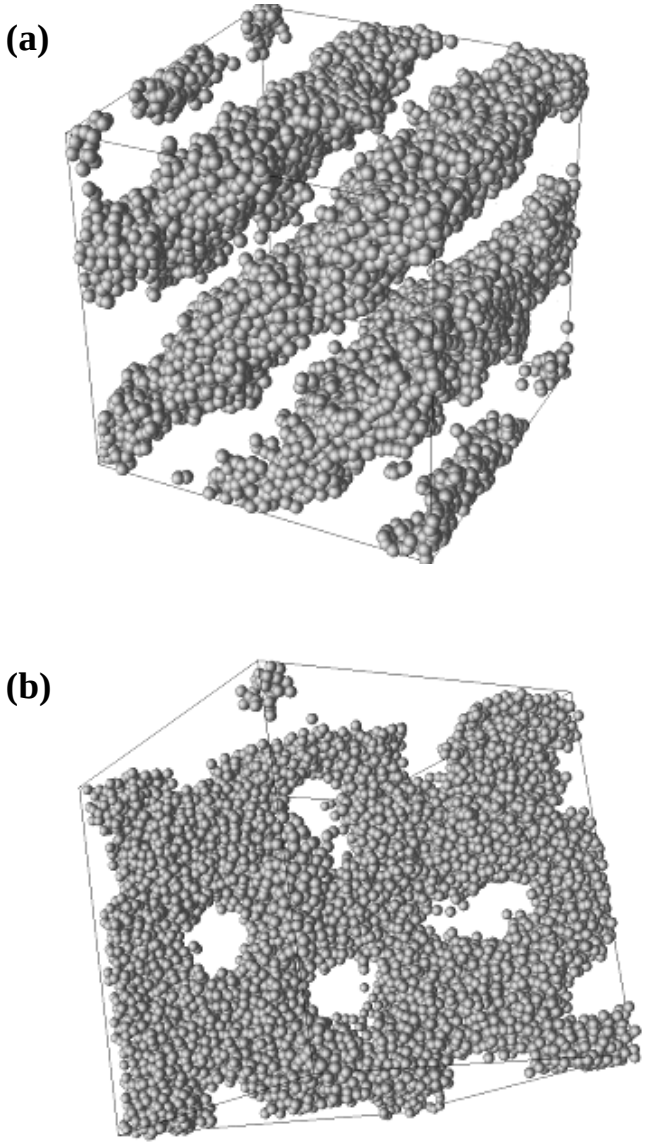

Figure 2.6. Snapshot of the metastable PL phase (*Model 1*). Only the minority component is presented. (a) All the lamellae are shown (b) Only one lamella is shown. The hexagonal packing of the perforations is evident.

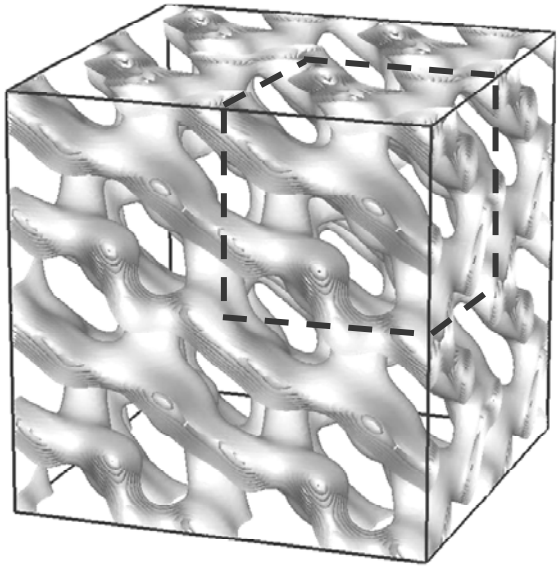

Figure 2.7. Isosurfaces of minority-component concentration for the co-continuous network phase (Co) showing a single periodic network as obtained with *Model 1*. The figure shows eight times a simulation snapshot of the Co phase. The dashed line indicates the size of one simulation box. More than one unit cell of the Co phase appears to be present in one simulation box.

snapshots there appear to be more than one unit cell of the Co phase contained inside the simulation box, and a lack of cell alignment with the box axes. Note in Figure 2.4 that although the Co phase comes up in a relatively wide region, βa^{ex} values (in Table 2.1) indicate that this is not a stable phase but a long-lived metastable state. Indeed, in some points of the phase diagram (e.g., $\chi N = 40$ and $f = 0.40$) we have observed the Co phase to spontaneously evolve to a more stable phase (e.g., Lamella) after long simulation runs. Although it is possible that this Co phase is just a defective G phase with some connections between the two networks, it seems unlikely that a defective phase would consistently show the same highly-regular structure presented in Figure 2.7. A more detailed analysis of the structure and region of stability of the Co phase (if a stable phase at all) lies outside the scope of the present work and will be the subject of a future study. Finally, we note that in our previous simulation work with a lattice model[40] we also encountered the same co-continuous network phase with the same regular structure albeit in a much more limited region of phase diagram.

Since the G phase had not been reported in previous continuum-space particle-based simulation work in pure DBC melts, we decided to briefly study an alternative model (*Model* 2) to determine if our results were particular to *Model* 1. However, simulations using *Model* 2 proved to be much more difficult; despite average simulation runs of over 5×10^7 steps, many of the systems did not reach equilibration to a definite morphology. The reason is that the steeper repulsive potential and the presence of an attractive potential well seem to make the system's dynamics significantly slower. Because of this, an exploration of the G phase boundaries for this model would demand prohibitively long simulation times. We therefore focused our simulations to a narrow region where, extrapolating from previous models, we expected to observe the G phase. We succeeded in detecting the G phase for $f = 0.30$ and $\phi = 0.30$ (where ϕ is the parameter that regulates the attractive strength in the Soddemann et al. potential)

Table 2.1. Excess Helmholtz free energy (βa^{ex}), excess chemical potential ($\beta\mu^{ex}$) and compressibility factor (Z) for the observed phases with *Model* 1 at different thermodynamic conditions. The quantities in parenthesis indicate the uncertainty in the last digit.

χN	f	*Phase*	Z	$\beta\mu^{ex}$	βa^{ex}
40	0.30	**C**	139.913(5)	240.75(5)	101.84(6)
40	0.30	**G**	139.654(7)	240.59(5)	101.94(6)
40	0.35	**G**	139.65(1)	240.62(6)	101.97(7)
40	0.35	**PL**	139.808(7)	240.76(5)	101.95(6)
40	0.35	**Co**	139.750(7)	240.76(5)	102.01(6)
40	0.40	**L**	139.780(5)	240.69(8)	101.91(9)
40	0.40	**Co**	139.801(4)	240.73(5)	101.93(5)
45	0.30	**G**	139.661(7)	240.69(5)	102.03(6)
45	0.30	**C**	139.862(7)	241.03(5)	102.17(6)
50	0.30	**G**	139.760(7)	241.18(5)	102.42(6)
50	0.30	**C**	139.650(7)	241.25(6)	102.60(7)
50	0.35	**PL**	139.812(7)	241.34(5)	102.53(6)
50	0.35	**Co**	139.80(1)	241.42(8)	102.62(9)
50	0.35	**G**	139.84(1)	241.23(5)	102.39(6)
60	0.30	**G**	140.02(1)	241.80(5)	102.78(6)
60	0.30	**C**	139.835(8)	241.62(5)	102.79(6)
60	0.40	**L**	139.924(5)	241.59(6)	102.67(7)
60	0.40	**Co**	139.997(7)	241.84(7)	102.84(8)

for a simulation box of L_{box} = 30. A minority-component concentration isosurface of the simulated G phase unit cell is shown in Figure 2.8. The calculated S(q) (results not shown) exhibited peaks with spacing ratios consistent with those shown in Figure 2.3; hence, corroborating the Gyroid character of the observed morphology. As expected, the C phase was formed instead for other simulation box sizes (i.e., L_{box} = 26-29). These results show, once again, that with the appropriate simulation box size the G phase can be obtained in continuum space simulations of DBC melts as long as the model employed is a sensible one. Finally, we are led to believe that the inability of previous particle-based simulation work in continuum space to observe the G phase in DBC melts was due to the use of boxes of inappropriate size rather than to limitations of the particular model adopted.

B. Structure of the Gyroid nodes

As can be seen in Figure 2.2, in the Gyroid phase the minority component forms two interweaving networks that never intersect. Each one of theses networks is composed of "tubes" (or "necks") and "nodes".[8] This basic structure is common to other bicontinuous phases like the Double Diamond and the Plumber's Nightmare.[66] For the particular case of the G phase, each node is formed by the intersection of three tubes. It has been suggested,[40, 42, 43] that the reason for the limited stability of bicontinuous phases in the phase diagram of DBC systems is the occurrence of packing frustration inside the nodes. The thickness of the tubes is determined by the length of the minority component block; however, the nodes are bulkier than the tubes because each node is formed by the junction of several tubes (e.g., three for the G phase) and are trying to preserve the constant mean curvature required to minimize the interfacial energy.[42] It has then been proposed[42, 43] that either the chains stretch to reach the center of the bulky nodes or regions of lower minority component

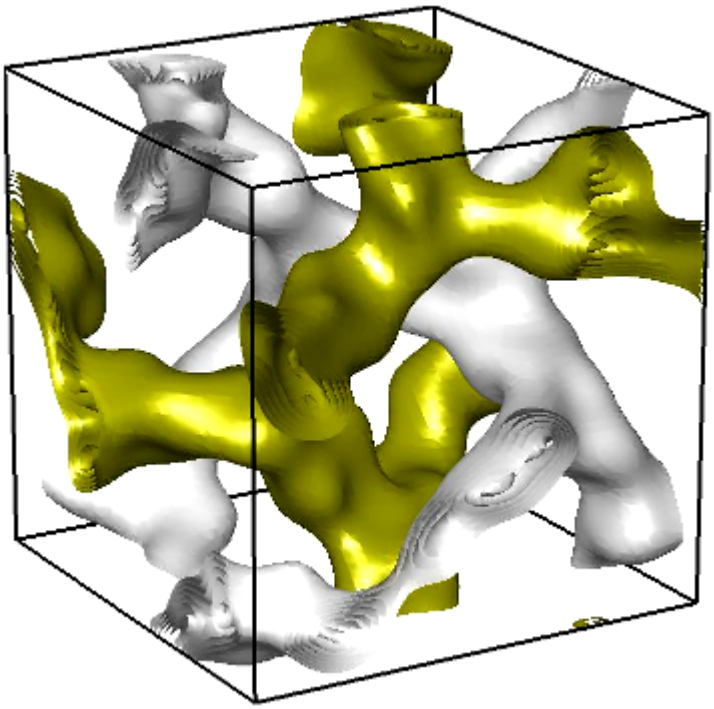

Figure 2.8. Minority component concentration isosurface for the G phase unit cell simulated with *Model* 2. The simulation box size was $L_{box} = 30$ and it was obtained at $f = 0.30$ and $\phi = 0.30$. More than 3×10^7 integration steps with $\delta t = 0.01$ were necessary in order to equilibrate the observed morphology.

concentration form in the center of the nodes. Either of these scenarios (or a combination of them) is entropically unfavorable and is referred to as "packing frustration". Our simulated G phases offer a great opportunity to directly detect the telltale signs of this "packing frustration" phenomenon.

To study the structure of the nodes in the G phase, we calculated the mean-square end-to-end distance for the full chain as well as for the minority and majority component blocks (i.e., block A and B respectively). To make the distinction between tube chains and node chains, we located the positions of the centers of the nodes in typical simulation snapshots where the G phase was already formed and equilibrated. Thus, if at least one of the chain beads was located within a sphere of radius r_o centered in any of the nodes, we assumed that the chain "belongs" to the node. Likewise, if all the beads of a chain are outside the spheres centered in the nodes we assume that the chain belongs to the tubes. The choice of the radius r_o is somehow arbitrary: if it is too big, many chains that are located in the tubes will contribute to the statistics of the nodes; if it is too small, only few chains will appear as belonging to the node and statistical inaccuracies will prevail. In addition, since the very location of the node center is found visually and hence subject to some arbitrariness, there is no point in making r_o excessively small. The choice of r_o is therefore a compromise among the above factors. For the systems studied here we found that r_o in the range [0.75-2.5] in dimensionless units is not only comparable to (or smaller than) the node size estimated visually but it also leads to results which are basically independent of the precise r_o value. We also observed that during short simulation runs (100 or 500 steps for *Model* 1 and *Model* 2, respectively) the position of the nodes' centers is essentially the same, allowing us to make averages over approx. 50 configurations to improve statistics. As mentioned earlier, for *Model* 1 (i.e., chains of soft spheres) we observed the G phase to form spontaneously in various points of the phase diagram. However, we

only analyzed the nodal structure of the G phase at conditions similar to those where the G phase was observed in the lattice system (i.e., $\chi N \sim 40$ and $f = 0.30$) in order to have some uniformity in the comparison. Figure 2.9 presents the mean-square end-to-end distance $\langle r^2 \rangle$ for the minority (A) block and the majority (B) block as function of r_o, inside the nodes and in the tubes. For this model the minority block inside the node tends to have a greater value of $\langle r^2 \rangle$ than in the tubes, consistent with the existence of packing frustration in the form of chain stretching. In addition, we also observed that $\langle r^2 \rangle$ tends to increase as r_o diminishes, suggesting that the chains need to stretch in order to reach the center of the node. Interestingly, Figure 2.9 also shows that the majority component block is more stretched for chains whose minority component block resides inside the nodes, indicating that the effect of packing frustration in the nodes is not limited to the minority component blocks. Although it is unclear why the majority component (B) blocks around the nodes also stretch, we surmise that this phenomenon is due to the way how the void inside the nodes is filled (Figure 2.10a). If such a filling were accomplished by only the stretching of the short A blocks, this would imply a too high block over-stretching and localized elastic tension (Figure 2.10b). Instead, a smaller entropic penalty may be incurred if the B blocks also stretch a little (Figure 2.10c), so that the chains can reach more easily the center of the (less bulkier) node. Thus, the packing frustration is alleviated by re-distributing the stretching between the two blocks.

When we compare the full-chain $\langle r^2 \rangle$ inside-the-nodes of the G phase to those observed for the chains in the C phase at the same thermodynamic conditions but different box size (recall Figure 2.4 and discussion thereof), we find that the chains inside the G nodes are considerably more stretched. For example, for simulation boxes of sizes $L_{box} = 20$ and 22 the C phase is spontaneously formed with full-chain $\langle r^2 \rangle$ values which are consistent (within statistical accuracy): 24.5(2) and 24.0(3),

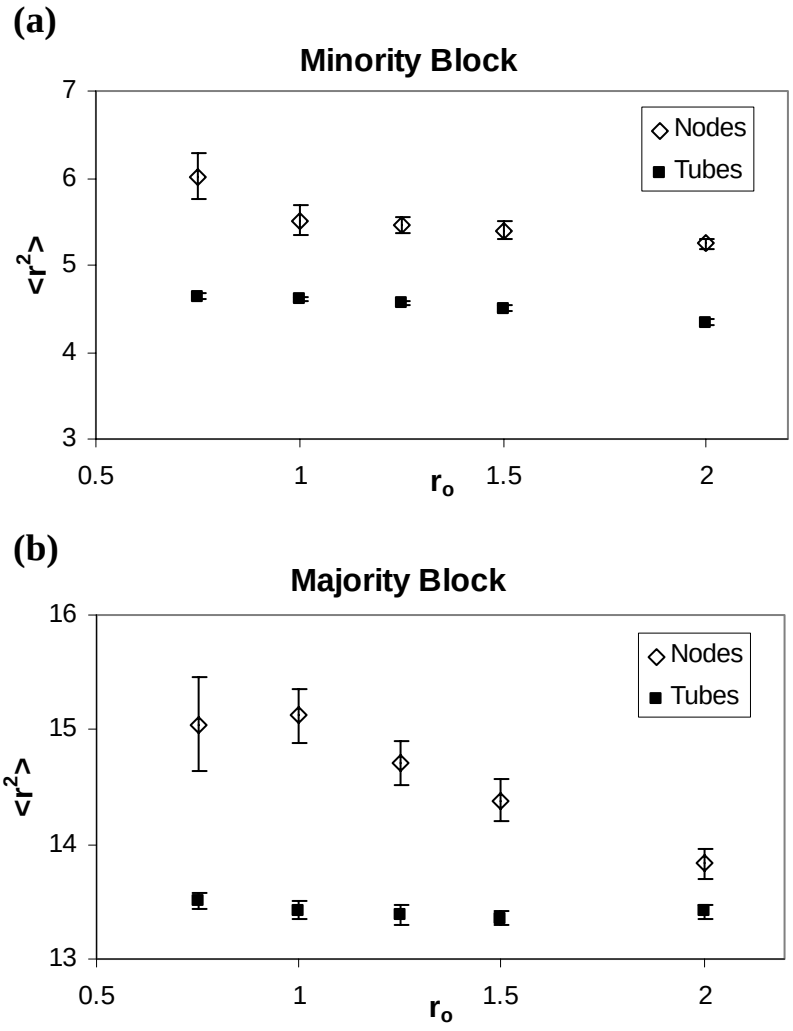

Figure 2.9. Mean-square end-to-end distance $\langle r^2 \rangle$ for chains of soft spheres (*Model* 1) in the G phase. The bigger values of $\langle r^2 \rangle$ inside the nodes indicate the presence of packing frustration. (a) Minority component (A) block $\langle r^2 \rangle$; (b) Majority component (B) block $\langle r^2 \rangle$

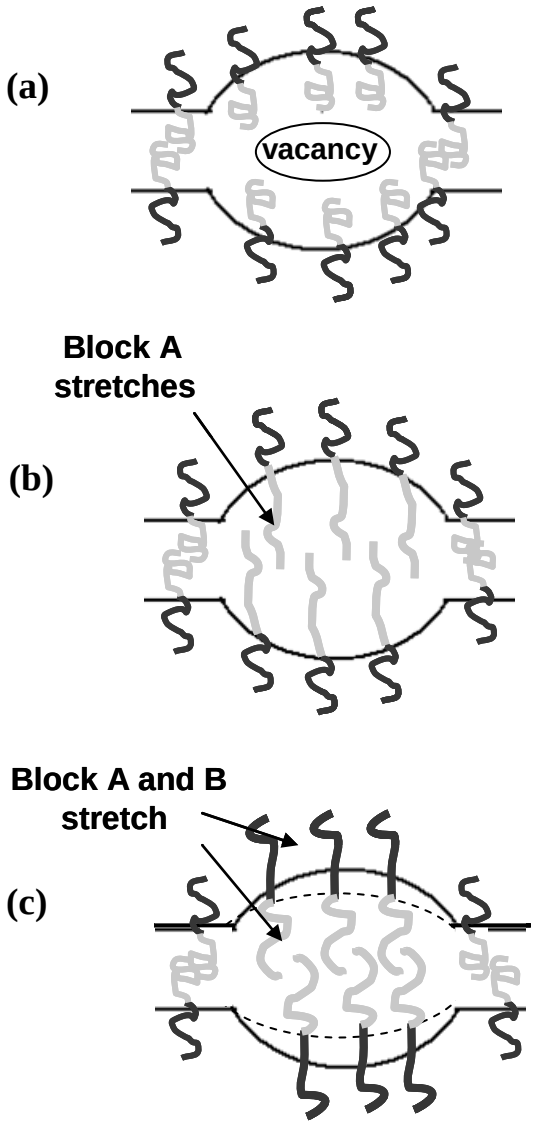

Figure 2.10. Cartoon illustrating how packing frustration could manifest in the G phase in pure DBC melts. (a) Because the nodes are bulkier than the tubes, if the chains do not stretch, packing frustration would appear as a lower density region or "vacancy" in the nodes' centers. (b) A hypothetical scenario where only A blocks stretch to fill the void. (c) A case where both (A and B) blocks "share" the stretching to reach the center of the node while slightly reducing the node bulkiness. Stretching of the B blocks has been exaggerated for visual effect. In scenarios (b) and (c) the penalty in packing entropy of (a) is traded by a penalty in the configurational entropy of the stretched chains; however, simulation data suggest that scenario (c) is the one that leads to the lowest entropy cost.

respectively; in contrast, with L_{box} = 21 the G phase is formed with an inside-the node $\langle r^2 \rangle$ value of 30.3(1.4) for r_o =1.0. These results are in agreement with the work of Yu et al.[26] who found that, in systems with selective solvent, the average chain in the G phase was stretched in comparison with the chains in the C or L phase.

When we analyzed *Model* 2 (i.e., chains with Soddemann et al. potential) we observed the same trend observed in *Model* 1; that is, the chains inside the nodes are appreciably more stretched than the ones located in the tubes. This fact is evident in Figure 2.11 where we show the $\langle r^2 \rangle$ of both (A and B) blocks for chains located inside and outside the nodes. In Figure 2.12 we present two isosurfaces of minority-component concentration, one for each network of the same G phase unit cell shown in Figure 2.8. Regions where minority-component concentration is zero appear "empty". We highlight in dark (red) the minority-component beads of the most stretched chains (i.e., those whose minority-block $\langle r^2 \rangle$ is greater than 20), and draw circles around the G nodes to guide the eye. Most of the highly stretched chains tend to group in the nodes, a trend that we observed for all the snapshots examined.

The two continuum space models studied in this work have two key differences. The first one is with the excluded volume interactions: while in *Model* 1 beads can overlap, in *Model* 2 beads cannot come too close due to a steep repulsion. The second difference is in the way segregation is achieved. In *Model* 1, microphase separation occurs due to a repulsive force between different-type blocks. In *Model* 2, blocks of the same kind interact with each other through an attractive force. Although in both cases the net effect is to cause the segregation between different-type blocks, the way how this is generated also determines the interactions between chains and vacuum. In *Model* 1, the vacuum would act like a non-selective good solvent since chains prefer being in contact with the vacuum than with other chains. For the high density employed here with *Model* 1, however, regions of vacuum are effectively

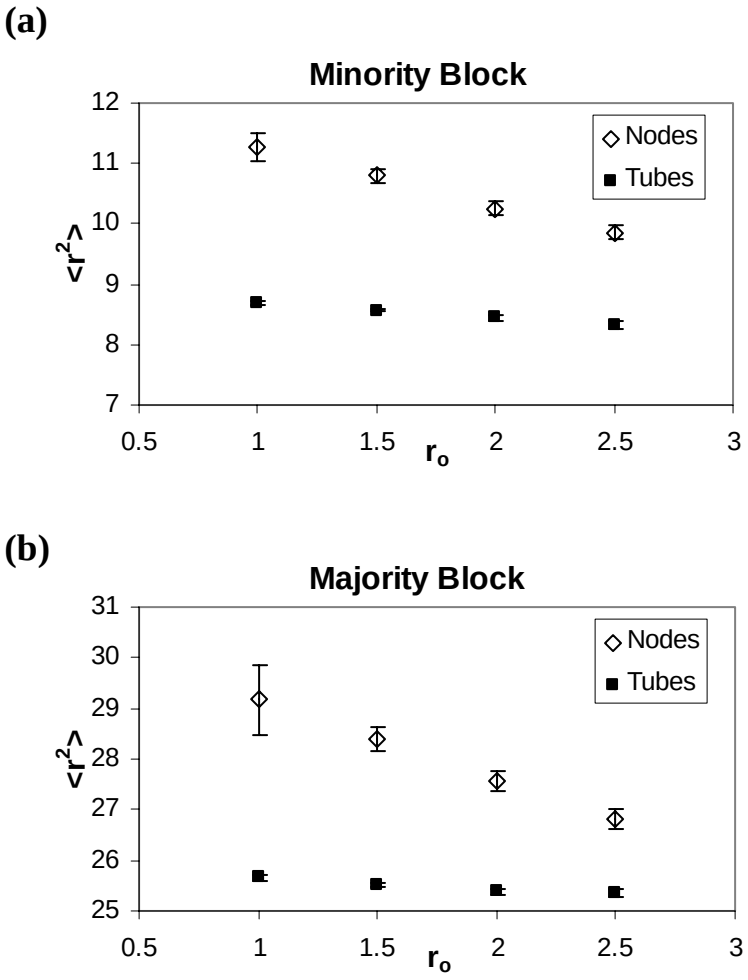

Figure 2.11. Mean-square end-to-end distance $\langle r^2 \rangle$ for *Model* 2 chains in the G phase. Stretching inside the nodes can be directly observed since $\langle r^2 \rangle$ is consistently larger inside the nodes. (a) Minority component block $\langle r^2 \rangle$; (b) Majority component block $\langle r^2 \rangle$.

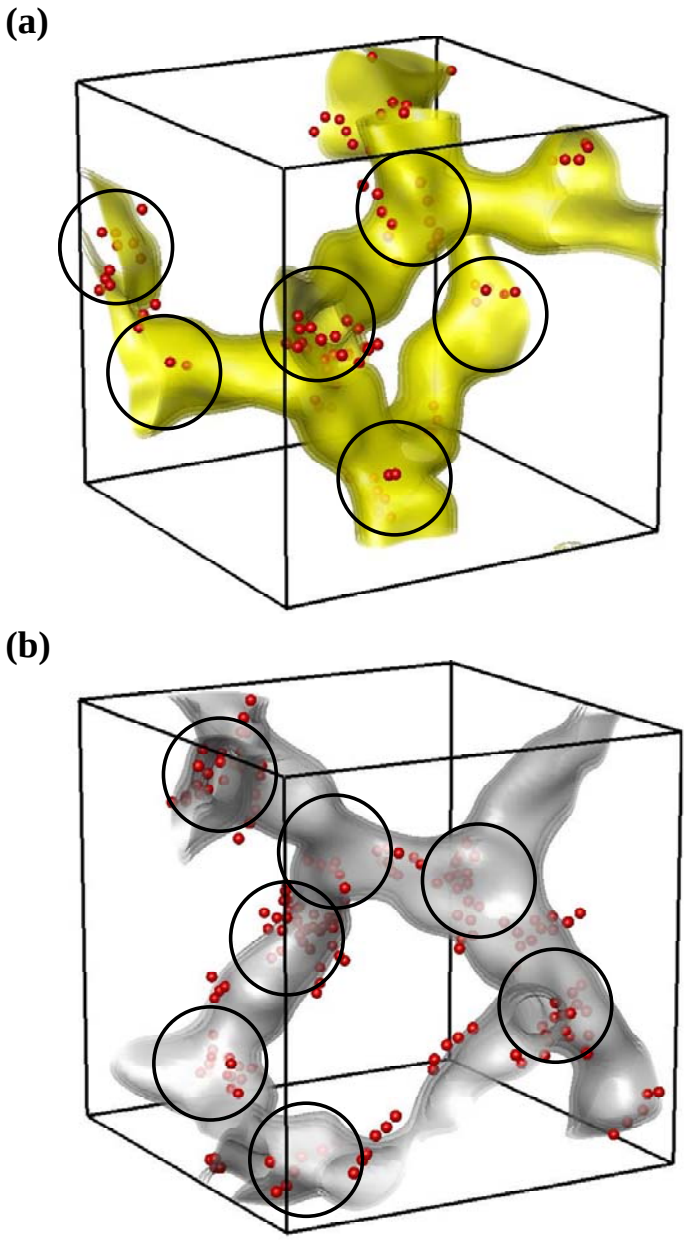

Figure 2.12. Minority-component concentration isosurfaces of the two networks encountered in the G phase unit cell obtained with *Model* 2. One of the two networks shown in Figure 2.8 is presented in (a) while the other is presented in (b). The minority beads of the highly stretched chains are shown in red (dark). Circles are drawn around the nodes to guide the eye. Most of the highly stretched chains are located inside the nodes.

suppressed. In *Model* 2, vacuum acts like a non-selective poor solvent because chains prefer being surrounded by same-type beads rather than by vacuum. These differences, however, do not seem to affect the way in which packing frustration is manifested inside the Gyroid nodes since in both models we find similar evidence of chain stretching.

In the lattice model, vacuum acts like a non-selective good solvent making it in this respect similar to *Model* 1. However, excluded volume interactions and spatial packing are unique in lattice models wherein partial overlapping of the beads is forbidden and empty space is discretized. Therefore we need not expect an identical manifestation of packing frustration.

In a previous publication[40] we studied the lattice model for DBCs using *NVT* Monte Carlo and analyzed the nodal structure of the G phase, finding clear evidence of packing frustration in the form of low concentration regions of the minority component in the nodal centers. Furthermore, we were unable to detect any signs of chain stretching given the statistical noise of the simulation data, in clear discrepancy with the behavior observed with the continuum space models. To clarify this issue, we decided to re-analyze the nodal structure of the lattice model Gyroid. We found that in our initial study, we had imposed a too restrictive requirement for a chain to "belong" to a node (i.e., more than 70 % of the minority block inside the node). By doing this and by restricting our study only to the $<r^2>$ of the minority component block, not only did we reduce the number of chains inside the nodes to a number where the statistical noise became dominant, but also we selected those few chains that had end-to-end distances limited to a value of the order of r_o. As a result, we failed to detect the chain stretching occurring in the Gyroid nodes. When reanalyzing the same on-lattice G phase configurations with the more appropriate parameters used for the continuum space models, we did detect chain stretching. Figure 2.13 shows how in every case

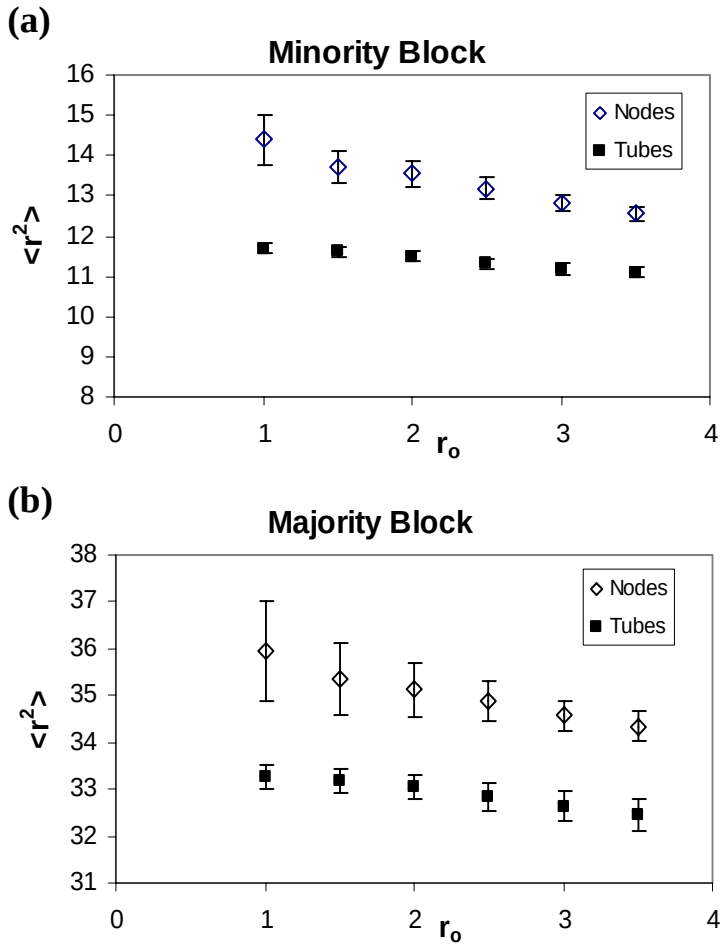

Figure 2.13. Mean-square end-to-end distance $\langle r^2 \rangle$ for the chains in the G phase simulated via on-lattice MC. Chains in the nodes are significantly more stretched than in the tubes. (a) Minority component block $\langle r^2 \rangle$; (b) Majority component block $\langle r^2 \rangle$.

(i.e., A block, or B block) $\langle r^2 \rangle$ is indeed larger inside the nodes than in the tubes, in accordance with the behavior observed in continuum space. Interestingly, however, the degree of chain stretching inside the nodes in the lattice system is less than in the continuum space models. We estimated the chain stretching (s) as the ratio between $\langle r^2 \rangle$ in the node and $\langle r^2 \rangle$ in the tubes for the minority component block, although similar results are obtained if the full-chain or majority-block $\langle r^2 \rangle$ are compared. As a representative example, if we set $r_o = 1.0$, we find that the degree of stretching for *Model* 1 is $s = 1.29$, for *Model* 2 $s = 1.30$ while for the lattice model is $s = 1.23$. A similar trend is observed for other values of r_o.

Previously, we had pointed out that packing frustration could be present in the form of either chain stretching or low concentration regions inside the nodes. It is reasonable to expect that when chains are stretched to reach the node's center, the low concentration regions will tend to be reduced or disappear. Henceforth, we would expect that in the continuum space models, where the chains were found to be more stretched, the low concentration regions should become less apparent. This expectation is confirmed by observations in Models 1 and 2, where we also monitored the number density of beads inside the nodes and, to the precision of our calculations, we could not identify the presence of low concentration regions in the center of the nodes. However, it is pointed out that for the length scale of the nodal dimensions, the density becomes a rapidly fluctuating quantity which, coupled to the difficulty of unambiguously defining the node centers, severely limits a reliable estimation of the average nodal density. Therefore, we conclude that low concentration regions in the center of the nodes for the continuum models, if present, cannot be reliably detected. The reason for this difference in behavior between the discrete and continuum models is not clear to us, although we suspect that differences in the excluded volume interactions play an important role.

IV. CONCLUSIONS

We explored the phase behavior of pure DBC melts in the intermediate segregation regime using the continuum space model for DBCs first proposed by Groot et al.[37] In this model (i.e., *Model* 1) copolymers are represented as chains of soft spheres connected through a harmonic potential. Good agreement with previous simulation work and theory is observed in the location of the classical phases C and L. In addition, we were able to simulate the bicontinuous G phase in a region of phase diagram that is consistent with theory and experiment. To the best of our knowledge, this is the first time that the G phase is successfully obtained in pure DBC melts in continuum-space particle-based simulations. Consistently with previous work,[38, 40] we found that the formation of the G phase can be seriously hindered by the inadequate choice of simulation box size. Such finite size effects can frustrate the system to the point where metastable phases become artificially stabilized. A co-continuous network phase (Co) was also observed in several points of the phase diagram in the region between the places where the L and G phases are stable. This Co phase was also observed in previous simulations[40] using lattice MC and bears some resemblance with the O^{70} of Tyler and Morse.[12]

A different copolymer model (*Model* 2), where beads interact with the Soddemann et al. potential energy function, was also successfully used to simulate the G phase. With this model, however, the simulations were found to take much longer to equilibrate. Again, we found that the final morphology obtained has a strong dependence on the system's box dimensions.

The fact that the G phase was simulated with two very distinct continuum space models (and in a lattice model in a previous paper) indicates that the particular details of the copolymer model are not crucial to the formation of this phase, although they do affect the size of the stability domain in the phase diagram. Indeed, we

conjecture that the reason for the difficulties of previous studies to simulate the G phase is related to finite size effects.

Having successfully obtained the G phase with two continuum space models, we analyzed the nodal structure of these phases and reanalyzed the nodal structure of the G phase obtained via lattice MC simulations. We found that for all these three models, the basic structure of the node is similar, showing evidence of packing frustration in the form of chain stretching; namely, chains inside the nodes exhibit larger mean-square end-to-end distances $\langle r^2 \rangle$ than chains located in the tubes. To the precision of our calculations we could not find in the continuum space models significant evidence of regions of low concentration of minority component in the center of the nodes as we found in the lattice model.

In future work we will explore the use of nanoparticles of various sizes as a means to stabilize various bicontinuous phases in block copolymer melts by reducing the packing frustration inside the nodes.

ACKNOWLEDGEMENTS

This work was supported by the US Department of Energy, Grant DE-FG02-05ER15682. The authors are also grateful to Prof. U. Wiesner for stimulating conversations and to Dr. S. Mendez for his contribution to an early version of the DPD code.

REFERENCES

1. Cho, B. K.; Jain, A.; Gruner, S. M.; Wiesner, U. *Science* **2004,** 305, (5690), 1598-1601.

2. Cho, B. K.; Jain, A.; Gruner, S. M.; Wiesner, U. *Chem. Commun.* **2005**, (16), 2143-2145.

3. Jain, A.; Toombes, G. E. S.; Hall, L. M.; Mahajan, S.; Garcia, C. B. W.; Probst, W.; Gruner, S. M.; Wiesner, U. *Angew. Chem., Int. Ed. Engl.* **2005,** 44, (8), 1226-1229.

4. Kamperman, M.; Garcia, C. B. W.; Du, P.; Ow, H. S.; Wiesner, U. *J. Am. Chem. Soc.* **2004,** 126, (45), 14708-14709.

5. Matsen, M. W. *J. Phys.: Condens. Matter* **2002,** 14, (2), R21-R47.

6. Hamley, I. W., *The Physics of Block Copolymers*. Oxford University Press: 1998.

7. Hajduk, D. A.; Harper, P. E.; Gruner, S. M.; Honeker, C. C.; Kim, G.; Thomas, E. L.; Fetters, L. J. *Macromolecules* **1994,** 27, (15), 4063-4075.

8. Schick, M. *Physica A (Amsterdam)* **1998,** 251, (1-2), 1-11.

9. Hajduk, D. A.; Takenouchi, H.; Hillmyer, M. A.; Bates, F. S.; Vigild, M. E.; Almdal, K. *Macromolecules* **1997,** 30, (13), 3788-3795.

10. Knoll, A.; Lyakhova, K. S.; Horvat, A.; Krausch, G.; Sevink, G. J. A.; Zvelindovsky, A. V.; Magerle, R. *Nat. Mater.* **2004,** 3, (12), 886-890.

11. Huinink, H. P.; van Dijk, M. A.; Brokken-Zijp, J. C. M.; Sevink, G. J. A. *Macromolecules* **2001,** 34, (15), 5325-5330.

12. Tyler, C. A.; Morse, D. C. *Phys. Rev. Lett.* **2005,** 94, (20), 208302.

13. Chan, V. Z. H.; Hoffman, J.; Lee, V. Y.; Iatrou, H.; Avgeropoulos, A.; Hadjichristidis, N.; Miller, R. D.; Thomas, E. L. *Science* **1999,** 286, (5445), 1716-1719.

14. Bates, F. S.; Schulz, M. F.; Khandpur, A. K.; Forster, S.; Rosedale, J. H.; Almdal, K.; Mortensen, K. *Faraday Discuss.* **1994**, (98), 7-18.

15. Matsen, M. W.; Bates, F. S. *J. Chem. Phys.* **1997,** 106, (6), 2436-2448.

16. Fredrickson, G. H.; Ganesan, V.; Drolet, F. *Macromolecules* **2002,** 35, (1), 16-39.

17. Hamley, I. W.; Castelletto, V.; Mykhaylyk, O. O.; Yang, Z.; May, R. P.; Lyakhova, K. S.; Sevink, G. J. A.; Zvelindovsky, A. V. *Langmuir* **2004,** 20, (25), 10785-10790.

18. Zvelindovsky, A. V.; Sevink, G. J. A.; Fraaije, J. *Physical Review E* **2000,** 62, (3), R3063-R3066.

19. Honda, T.; Kawakatsu, T. *Macromolecules* **2006,** 39, (6), 2340-2349.

20. Huh, J.; Ginzburg, V. V.; Balazs, A. C. *Macromolecules* **2000,** 33, (21), 8085-8096.

21. Thompson, R. B.; Ginzburg, V. V.; Matsen, M. W.; Balazs, A. C. *Science* **2001,** 292, (5526), 2469-2472.

22. Chervanyov, A. I.; Balazs, A. C. *J. Chem. Phys.* **2003,** 119, (6), 3529-3534.

23. Lin, Y.; Boker, A.; He, J. B.; Sill, K.; Xiang, H. Q.; Abetz, C.; Li, X. F.; Wang, J.; Emrick, T.; Long, S.; Wang, Q.; Balazs, A.; Russell, T. P. *Nature* **2005,** 434, (7029), 55-59.

24. Fredrickson, G., *The Equilibrium Theory of Inhomogeneous Polymers*. Oxford University Press: New York, 2006.

25. Larson, R. G. *J. Phys. II (Paris)* **1996,** 6, (10), 1441-1463.

26. Yu, B.; Li, B. H.; Sun, P. C.; Chen, T. H.; Jin, Q. H.; Ding, D. T.; Shi, A. C. *J. Chem. Phys.* **2005,** 123, (23), 234902.

27. Gonzalez-Segredo, N.; Coveney, P. V. *Europhys. Lett.* **2004,** 65, (6), 795-801.

28. Rychkov, I. *Macromol. Theory Simul.* **2005,** 14, (4), 207-242.

29. Rychkov, I.; Yoshikawa, K. *Macromol. Theory Simul.* **2004,** 13, (3), 257-264.

30. Rychkov, I.; Yoshikawa, K. *J. Chem. Phys.* **2004,** 120, (7), 3482-3488.

31. Iacovella, C. R.; Keys, A. S.; Horsch, M. A.; Glotzer, S. C., *Icosahedral packing of polymer-tethered nanospheres and stabilization of the gyroid phase* Unpublished).

32. Horsch, M. A.; Zhang, Z. L.; Iacovella, C. R.; Glotzer, S. C. *J. Chem. Phys.* **2004,** 121, (22), 11455-11462.

33. Schultz, A. J.; Hall, C. K.; Genzer, J. *Macromolecules* **2005,** 38, (7), 3007-3016.

34. Schultz, A. J.; Hall, C. K.; Genzer, J. *J. Chem. Phys.* **2002,** 117, (22), 10329-10338.

35. Groot, R. D.; Madden, T. J. *J. Chem. Phys.* **1998,** 108, (20), 8713-8724.

36. Groot, R. D.; Madden, T. J.; Tildesley, D. J. *J. Chem. Phys.* **1999,** 110, (19), 9739-9749.

37. Groot, R. D.; Warren, P. B. *J. Chem. Phys.* **1997,** 107, (11), 4423-4435.

38. Dotera, T. *Phys. Rev. Lett.* **2002,** 89, (20), 205502.

39. Matsen, M. W. *Macromolecules* **1995,** 28, (17), 5765-5773.

40. Martinez-Veracoechea, F. J.; Escobedo, F. A. *Macromolecules* **2005,** 38, (20), 8522-8531.

41. Dotera, T.; Hatano, A. *J. Chem. Phys.* **1996,** 105, (18), 8413-8427.

42. Matsen, M. W.; Bates, F. S. *Macromolecules* **1996,** 29, (23), 7641-7644.

43. Hasegawa, H.; Hashimoto, T.; Hyde, S. T. *Polymer* **1996,** 37, (17), 3825-3833.

44. Frenkel, D.; Smit, B., *Understanding Molecular Simulation*. Academic Press: San Diego, CA, 2002.

45. Soddemann, T.; Dunweg, B.; Kremer, K. *Eur. Phys. J. E* **2001,** 6, (5), 409-419.

46. Espanol, P. *Phys. Rev. E* **1995,** 52, (2), 1734-1742.

47. Soddemann, T.; Dunweg, B.; Kremer, K. *Phys. Rev. E* **2003,** 68, (4), 046702.

48. Nikunen, P.; Karttunen, M.; Vattulainen, I. *Comput. Phys. Commun.* **2003,** 153, (3), 407-423.

49. Shardlow, T. *SIAM J. Sci. Comput.* **2003,** 24, (4), 1267-1282.

50. Vattulainen, I.; Karttunen, M.; Besold, G.; Polson, J. M. *J. Chem. Phys.* **2002,** 116, (10), 3967-3979.

51. Lyubartsev, A. P.; Martsinovski, A. A.; Shevkunov, S. V.; Vorontsovvelyaminov, P. N. *J. Chem. Phys.* **1992,** 96, (3), 1776-1783.

52. Wilding, N. B.; Muller, M. *J. Chem. Phys.* **1994,** 101, (5), 4324-4330.

53. Bennett, C. H. *J. Comput. Phys.* **1976,** 22, (2), 245-268.

54. Trebst, S.; Huse, D. A.; Troyer, M. *Phys. Rev. E* **2004,** 70, (4), 046701.

55. Escobedo, F. A.; Depablo, J. J. *J. Chem. Phys.* **1995,** 103, (7), 2703-2710.

56. Escobedo, F. A.; dePablo, J. J. *J. Chem. Phys.* **1996,** 105, (10), 4391-4394.

57. Fenwick, M. K.; Escobedo, F. A. *J. Chem. Phys.* **2003,** 119, (22), 11998-12010.

58. Fenwick, M. K.; Escobedo, F. A. *J. Chem. Phys.* **2004,** 120, (7), 3066-3074.

59. Abreu, C. R. A.; Escobedo, F. A. *Macromolecules* **2005,** 38, (20), 8532-8545.

60. Escobedo, F. A.; Chen, Z. *J. Chem. Phys.* **2004,** 121, (22), 11463-11473.

61. Matsen, M. W.; Griffiths, G. H.; Wickham, R. A.; Vassiliev, O. N. *J. Chem. Phys.* **2006,** 124, (2), 024904.

62. Woloszczuk, S.; Banaszak, M.; Jurga, S.; Pakula, T.; Radosz, M. *J. Chem. Phys.* **2004,** 121, (23), 12044-12049.

63. McGreevy, R. L., *Computer Modeling in Inorganic Crystallography*. Academic Press: San Diego, CA, 1997.

64. Epps, T. H.; Cochran, E. W.; Hardy, C. M.; Bailey, T. S.; Waletzko, R. S.; Bates, F. S. *Macromolecules* **2004,** 37, (19), 7085-7088.

65. Cochran, E. W.; Bates, F. S. *Phys. Rev. Lett.* **2004,** 93, (8), 087802.

66. Finnefrock, A. C.; Ulrich, R.; Toombes, G. E. S.; Gruner, S. M.; Wiesner, U. *J. Am. Chem. Soc.* **2003,** 125, (43), 13084-13093.

CHAPTER 3

MONTE CARLO STUDY OF THE STABILIZATION OF COMPLEX BICONTINUOUS PHASES IN DIBLOCK COPOLYMER MELTS*

I. INTRODUCTION

The capacity of block copolymer systems to self-assemble at mesoscopic length scales has made them the focus of extensive research.[1, 2] Particular attention has been paid to pure diblock copolymer (DBC) melts where different morphologies of specific geometry can be rationally obtained just by adjusting the relative sizes of the two blocks.[1, 3] By this means a number of distinct mesophases can be obtained: spheres with bcc packing (S), cylinders hexagonally packed (C), the lamellar phase (L), the bicontinuous gyroid phase[4, 5] (G), and the recently-observed co-continuous O^{70} phase.[6, 7] A perforated lamellae phase (PL) is often observed in experiments[8] and simulations;[9, 10] however, this phase has been proven to be just a long lived metastable state in the bulk of the pure DBC melt phase diagram.[11, 12]

Of great scientific and technological interest is a particular kind of mesophase based in minimal surfaces, known as the ordered bicontinuous phases.[13] In these phases the minority component forms two triply-periodic interweaving networks that never intersect, making them ideal candidates as precursor of: porous materials,[14, 15] regular three-dimensional networks, and high-conductivity nanocomposites.[16] Experimentally, some systems of surfactants have been observed to present a rich variety of these phases. For example, Ström and Anderson[17] observed in the system Didodecyldimethylammonium Bromide-Water-Styrene a progression of the

bicontinuous phases gyroid (G), double diamond (DD), plumber's nightmare (P) and Neovius' surface [C(P)]. However, pure DBC melts present a much more limited variety of bicontinuous phases. While in pure DBC melts it was initially thought that the stable bicontinuous phase was the DD phase, it is now well established that the only stable bicontinuous phase in pure DBC melts is the G phase.[4, 18, 19]

A common feature of the ordered bicontinuous phases is that their minority-component networks form a structure composed of tubes (connectors) and nodes.[20] The number of tubes intersecting in each node depends upon the specific phase. For example, the number of tubes that intersect in the nodes of the G, DD and P phases are: three, four, and six tubes, respectively. While the thickness of the tubes is roughly determined by the minority-component block length, the thickness of the nodes (which are formed by the junction of several tubes) is necessarily bulkier in order to approach the constant-mean-curvature (CMC) structure that will minimize the interfacial energy.[20] As a result, the DBC chains cannot reach the center of the nodes without either stretching or deforming the node's shape, causing an entropically unfavorable scenario known as packing frustration. It has been suggested[5, 20] that the reason for the limited stability of the bicontinuous phases in the pure DBC melt is the existence of packing frustration inside the nodes. Moreover, it has also been suggested[20] that since the G phase is the bicontinuous phase with the smallest number of tubes per node, and therefore with the smallest nodes, the G phase is the ordered bicontinuous phase with the least packing frustration, and hence, the only stable one in pure DBC melts.
In previous works,[21, 22] we were able to detect direct evidence of packing frustration inside the G phase nodes. Additionally, we used bidispersity as a means to alleviate the frustration, achieving the stabilization of the G phase in a wider range of temperatures.[21] The frustration in the nodes could also be alleviated by the addition of small quantities of other "fillers" or "additives" like selective nanoparticles or

homopolymer (Figure 3.1) that would preferentially concentrate inside the nodes.[23] In principle, this reduced frustration can be used not only to increase the range of stability of the G phase but also to stabilize other bicontinuous phases like the DD and P.[20] Indeed, in systems of triblock copolymers, Dotera[24] performed lattice Monte Carlo (MC) simulations where a progression of the form "single" G → "single" D → and "single" P was observed by the addition of homopolymer. In DBC systems, however, the situation is less clear. On one hand, mean-field SCFT has been used to predict the stabilization of the DD phase in a very narrow region of the phase diagram by the addition of homopolymer.[25, 26] On the other hand, the Wiesner Group[27, 28] has realized a series of experiments in a mixture of a diblock copolymer (e.g., PI-b-PEO) with an inorganic aluminosilicate, for which the P phase was observed but the DD was not.

Although SCFT has proven to be a very useful tool in resolving many of the issues regarding the phase behavior of block copolymer systems,[29-31] in the present work we will adopt the more straightforward (though more time consuming) particle-based approach, wherein the effects of finite chain length size and local density fluctuations are naturally incorporated. Particle-based simulations have been relatively successful in showing the stabilization of the G and PL phases in DBC systems with a selective solvent.[32-37] However, to best of our knowledge, a particle-based approach has never been used to predict the stabilization of ordered bicontinuous phases, different from the G phase, in DBC melt systems. Moreover, even though extensive work has been done in the area of block copolymer/nanoparticle composites,[38-40] these results did not treat the bicontinuous phases and concentrated in the "classical" (i.e., the L, C and S phases) morphologies.

In the present paper, we perform lattice MC simulations to study the stabilization of different complex phases through the reduction of packing frustration.

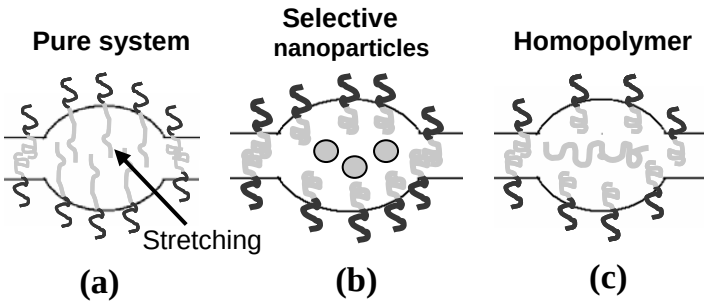

Figure 3.1. Cartoon representing how packing frustration can manifests in the form of chain stretching in the nodes of the bicontinuous phases, and some alternatives that can be used to alleviate this frustration. (a) In the pure system packing frustration occurs in the nodes. (b) Selective nanoparticles can reduce he frustration. (c) Homopolymer can alleviate the packing frustration inside the nodes.

Two different strategies are considered which aim to counter the frustration effects by addition of minority (A) component in the form of: 1) small solvent-like selective nanoparticles of size comparable to the polymer Kuhn length (i.e., monomeric solvent), 2) homopolymer of a chain-length equal to 80 % that of the copolymer chains. In order to be able to observe the bicontinuous phases, simulations were carried out at conditions where the G phase has previously been observed for the pure melt in lattice systems (i.e., $\chi N = 40$ and volume fraction of A-block=0.30).[21] A surprisingly different phase behavior is observed upon increasing the amount of the A-component additive in the two different cases. While with the first strategy (i.e., addition of small nanoparticles) we observed the progression G → PL → L→ Reversed-Gyroid (RG), with the PL phase sharing the phase diagram with a long-lived metastable orthorhombic co-continuous network phase known as O[52]. With the second strategy (i.e., addition of homopolymer) we observed the mesophase progression G → DD → P. In both, the DD and the P phases, the homopolymer was observed to preferentially concentrate in the nodes, consistent with the idea of reduction of the packing frustration. Additionally, in regions with homopolymer concentration equal to or greater than the concentration where the P phase was found, a novel morphology was observed, wherein cylinders of two different diameters alternate in a tetragonal (square) packing. The difference observed in the phase behavior for the two strategies considered is rationalized in terms of the difference in translational (mixing) entropy between the small nanoparticles and the homopolymer.

II. MODEL AND METHODS

A simple cubic lattice is used to discretize space where each site can be occupied only by a single bead of the polymer chain. Each bead in the chain represents a Kuhn segment. Bonds are allowed between the edges of each site as well as between

diagonals sites, yielding to a total of 26 neighbors per lattice site. This type of lattice have successfully been used in numerous studies of the phase behavior of surfactant/copolymer systems.[21, 32, 41]

In this scheme each bead interacts only with its 26 nearest neighbors. The contact energy ε_{ij} is defined as,

$$\varepsilon_{ij} = \begin{cases} 1 \; if \; i \neq j \\ 0 \; if \; i = j \end{cases} \tag{26}$$

where i and j represent the type of bead. In DBC systems only two different types of beads are needed: "A" beads (i.e., minority component) and "B" beads (i.e., majority component). The void volume fraction is set to $\eta = 0.25$ to facilitate equilibration.[21]

As is customary for DBC lattice simulations, the Flory-Huggins interaction parameter (χ) is obtained from χ=(# non-bonded neighbors)×(fraction occupied)×ε_{AB}/kT,

$$\chi = 18\beta \tag{27}$$

where $\beta = \varepsilon_{AB}/kT$, k is Boltzmann constant, and T is temperature.[24] The DBC composition is defined by,

$$f = \frac{\#\text{ of A beads in chain}}{N} \tag{28}$$

where N is the DBC chain length. Since all beads occupy the same volume, f also defines the volume fraction of A beads in a DBC chain.

In the present work the DBC chain length is set to $N = 20$ with a minority component volume fraction of $f = 0.30$. Additionally, the simulation conditions will be fixed at $\beta = 0.1111$ (i.e., $\chi N = 40$) since it has been found that at these conditions the pure DBC melt for this model presents a stable Gyroid phase.[21]

The small nanoparticles are represented by a single A bead (i.e., each nanoparticle occupies only a single lattice site). The homopolymer is represented as

chains of A beads, with a chain-length size of N_{ho} =16. The fraction of non-empty sites occupied by the "additive" (i.e., either nanoparticles or homopolymer) is denoted by ϕ_{add}.

Simulations are carried out according to the *NVT* ensemble Monte Carlo scheme where a set of moves (hops, reptations, and switches)[21] is attempted and accepted with probability given by the standard Metropolis criterion.[42] More details about this model can be found elsewhere.[21] The "hop", "reptation" and "switching" moves were performed with a relative frequency of 300**:**30**:**1 respectively. The systems were equilibrated in the athermal limit and then quenched to the target temperature (i.e., β=0.1111) where the systems were left to spontaneously evolve towards a morphology. Simulations were usually run for 8×10^6 MC cycles, of which 2×10^6 MC cycles were for equilibration and the rest for production (when statistics are collected). Each cycle comprised of N_{mon} MC moves where N_{mon} is the total number of monomers in the system.

III. CHEMICAL POTENTIAL CALCULATIONS

At a given set of thermodynamic conditions, more than one morphology can often spontaneously form depending upon the simulation box size and initial conditions.[21, 22, 24] The reason is that block copolymer morphologies present long range ordering, making some structures particularly sensitive to finite-size effects. As a consequence, metastable structures can be stabilized when the simulation box is not of a size commensurate with the unit cell of the stable phase. In the *NVT* ensemble, the most stable phase is the one with the lowest excess Helmholtz free energy per unit chain. Neglecting the PV contributions, which are assumed to be similar and small in different phases with the same density, the stability between phases can be discerned through the excess chemical potential ($\beta\mu^{ex}$), where the "excess" properties are

defined by taking as reference the ideal chain (i.e., a chain having only bonded interactions). In a previous paper[22] we gave a detailed explanation of how to accurately calculate $\beta\mu^{ex}$ using a variant of the expanded-ensemble (EXE) method.[43, 44] In this approach one gradually inserts/removes a target chain in the system by appending/deleting beads to/from it. This method requires a means for accurate estimation of the free-energy differences associated with such growth/reduction transitions, and the use of suitable biasing weights to attain efficient sampling of all transitions; we adopt here Bennett's acceptance-ratio method[45] to estimate free-energy differences and the method of Trebst et al.[46] to get the biasing weights. The partition function of the expanded-ensemble (Q_{EXE}) is defined as,

$$Q_{EXE} = \sum_{m=1}^{M} \exp(\psi_m)\, Q(\lambda_m) \tag{29}$$

where $Q(\lambda_m)$ in our case is the partition function of the *NVT* ensemble with characteristic parameter λ_m (e.g., the number of target-chain beads already inserted), and ψ_m is an arbitrary bias weighting function that is optimized to obtain efficient sampling[22] by means of a modification of the method of Trebst et al.[46]

If the insertion/deletion attempts are proposed with equal probability, the Metropolis acceptance criterion for a macrostate transition $m \to m+\Delta$, with configurational-bias sampling, biased only according to excluded volume interactions, becomes:

$$P_{acc} = \min\left\{1, \exp(-\upsilon + \psi_{m+\Delta} - \psi_m)\right\}, \tag{30}$$

with

$$\upsilon = -\Delta \ln W + \beta\left(U_{m+\Delta} - U_m\right) \tag{31}$$

where $\Delta = +1$ for growth, $\Delta = -1$ for reduction , U is the interaction energy and W is the Rosenbluth weight[42] calculated with excluded volume interactions alone for the

corresponding insertion/deletion process. Macrostate transitions were attempted with a frequency of two attempts per MC cycle.

The Helmholtz free-energy (A) differences associated with the insertion/deletion of a bead in the target chain can be estimated using Bennett's acceptance ratio formula:

$$\beta A(\lambda_{m+1}) - \beta A(\lambda_m) \equiv \ln \frac{Q(\lambda_m)}{Q(\lambda_{m+1})} = C - \ln \frac{\ell_{m+1,m}}{\ell_{m,m+1}} \tag{32}$$

where $\ell_{m,m+1}$ is the number of trial transitions $\lambda_m \rightarrow \lambda_{m+1}$ and C is found from:

$$\sum_m \left(1 + \exp\left[\upsilon\left(\lambda_m \rightarrow \lambda_{m+1}\right) - C\right]\right)^{-1} = \sum_{m+1} \left(1 + \exp\left[\upsilon\left(\lambda_{m+1} \rightarrow \lambda_m\right) + C\right]\right)^{-1} \tag{33}$$

where the summation in the left runs over all the $\lambda_m \rightarrow \lambda_{m+1}$ attempted transitions and the summation in the right over all the $\lambda_{m+1} \rightarrow \lambda_m$ attempted transitions. Finally, the excess chemical potential for a single specie is calculated from:

$$\beta\mu_i^{ex}(\lambda_1 \rightarrow \lambda_M) = [\beta A(\lambda_M) - \beta A(\lambda_1)] = \sum_{m=1}^{M-1} \left[\beta A(\lambda_{m+1}) - \beta A(\lambda_m)\right] \tag{34}$$

Stability between phases is then discerned by comparison of the molar Gibbs free energy of the mixture, βg, calculated as,

$$\beta g = \sum y_i \beta \mu_i^{ex} \tag{35}$$

with y_i the mole fraction of specie i in the system.

IV. RESULTS AND DISCUSSION

Addition of small nanoparticles

The phase behavior of DBC/small-nanoparticle mixtures was explored for a range of nanoparticle concentrations between $\phi_{add} = 0.0$ and $\phi_{add} = 0.40$. A variety of morphologies was observed by changing the nanoparticles volume fraction ϕ_{add}. Among the phases that had been previously reported in DBC systems we observed: the

bicontinuous G phase, the PL phase, and the L phase (Figure 3.2). In addition, an orthorhombic co-continuous network phase known as O^{52} was also observed (Figure 3.3). In this phase, the minority component forms a *single* continuous network. The O^{52} phase has never been observed in DBC systems and has only been reported for triblock copolymer melts in the experiments carried out by Cochran and Bates.[47] Since different co-continuous network phases could in principle be obtained, the structure factor, *S(q),* of the simulated network phase was calculated. Figure 3.4 shows different projections of the calculated *S(q)*. The location of the peaks is indeed consistent with the Pnna symmetry (i.e., the O^{52} phase) and with the *S(q)* obtained by Cochran and Bates.[47] Moreover, simulations only produced a defect free O^{52} phase when the edges of the simulation box had sizes consistent with ratios about 2**:**b**:**1 with b ~ (1.8-1.9), which are comparable with the ratios observed experimentally for triblock copolymers (i.e., 2**:**1.73**:**1).[47] At this point it is important to note that even though additional simulations were carried out in boxes with dimensions consistent with the lattice constants of the O^{70} phase,[6] the latter was never observed. Finally, for high nanoparticle concentration (i.e., $\phi_{add} \sim 0.40$) the "reversed" perforated lamellae phase (RPL) and the "reversed" Gyroid phase (RG) were observed. In the RPL phase the B blocks form perforated lamellae surrounded by an A-component (i.e., A blocks + nanoparticles) matrix. Similarly, the RG phase presents B-component interweaving networks in an A-component matrix.

As pointed out in previous works,[21, 22, 24] the mesophases obtained in simulations of DBC melts are particularly sensitive to the choice of simulation box dimensions. As a consequence, at a given set of thermodynamic conditions more than one morphology can be observed. Thus, the most stable phase has to be discerned by comparing the values of the chemical potentials as discussed in section III on *Chemical Potential Calculations.* In Figure 3.5 we present an approximated phase

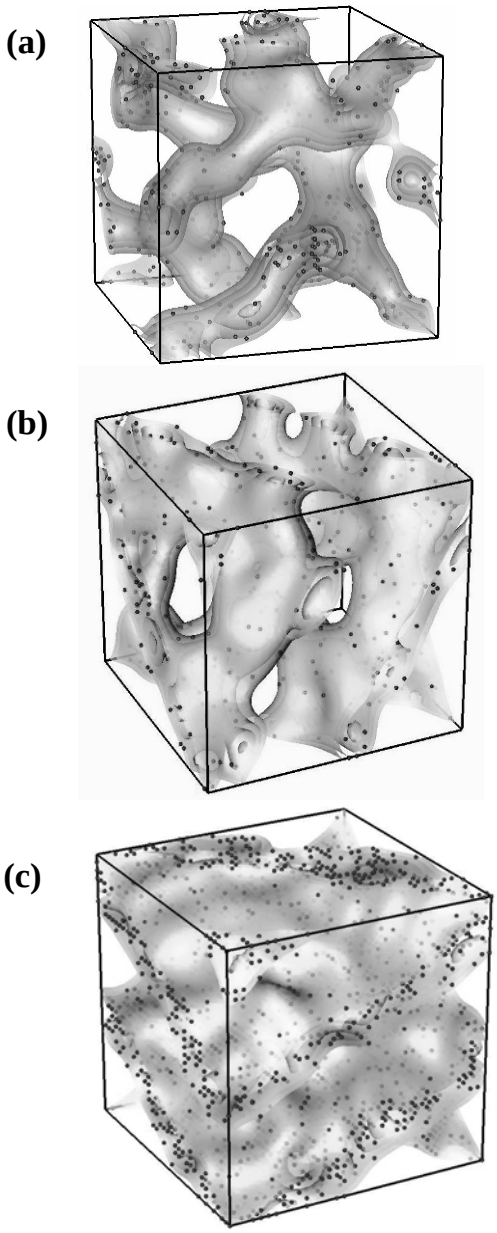

Figure 3.2. Commonly observed morphologies in DBC systems that were obtained by the addition of small selective nanoparticles. The majority (B) component is not shown. Nanoparticles that are located in the majority component domain are not shown for clarity.(a) The G phase. (b) The PL phase. (c) The L phase.

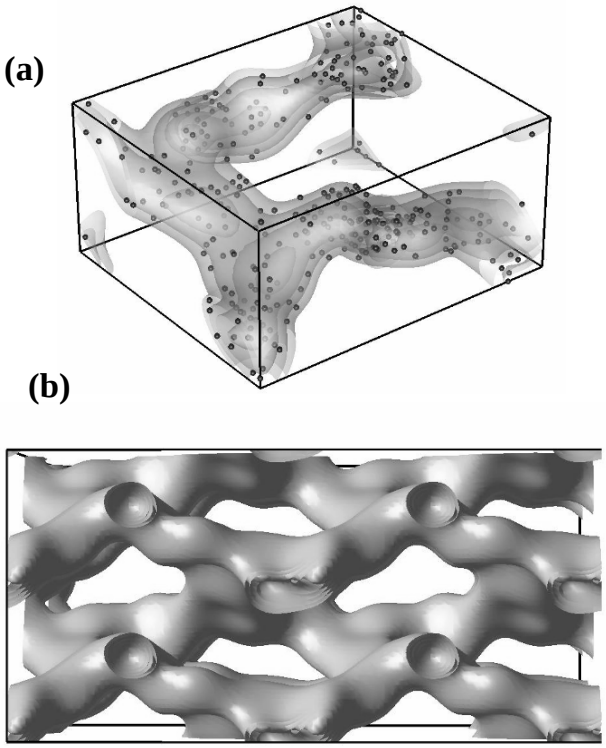

Figure 3.3. The orthorhombic co-continuous network phase O^{52} observed in simulations for a nanoparticle concentration range of ϕ_{add} ~ (0.05-0.09). Nanoparticles that are located in the majority component domain are not shown for clarity. (a) A unit cell of the O^{52} phase. (b) Eight (8) unit cells of the O^{52} phase.

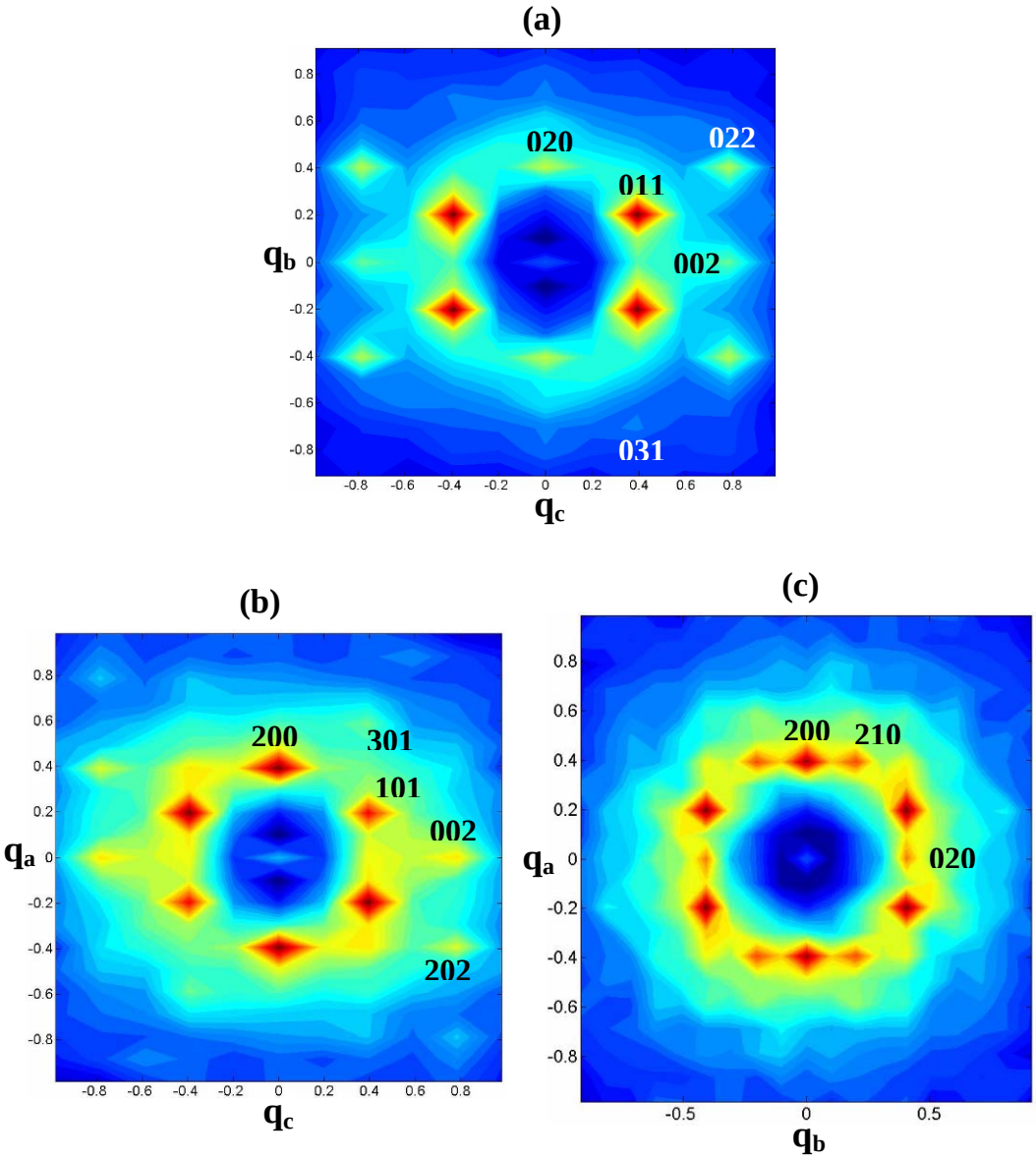

Figure 3.4. 2D projections of the structure factor for a simulated O^{52} phase with lattice constants a=32, b=31, and c=16 (lattice units), obtained at a nanoparticle concentration of ϕ_{add}= 0.06. Location of peaks is consistent with the Pnna symmetry. (a) Projection in the "a" axis. (b) Projection in the "b" axis. (c) Projection in the "c" axis.

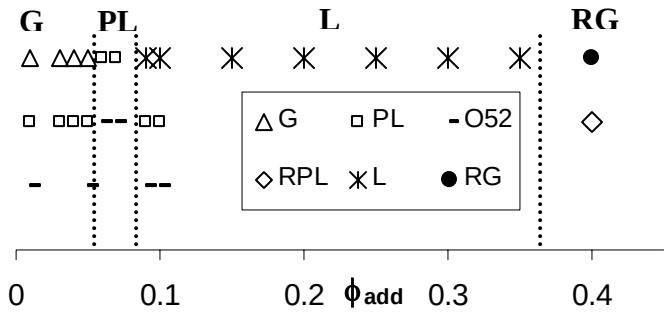

Figure 3.5. Approximate phase diagram where the morphologies obtained by addition of small nanoparticles are presented as a function of the nanoparticle concentration ϕ_{add}. All the morphologies observed (i.e., stable and metastable) are shown. Approximate phase boundaries between stable phases – which are indicated in big bold letters- are based on the chemical potential calculations. A progression of the form G → PL → L → RG is observed with increasing ϕ_{add}.

diagram where all the spontaneously obtained morphologies are shown as a function of the nanoparticle concentration ϕ_{add}. Though several mesophases can be shown at a given $\phi_{add,}$ phase boundaries between the stable phases are roughly delineated based on the calculated values of βg. In general, the stable phases showed a progression of the form G → PL → L → RG with increasing ϕ_{add}. Although the O^{52} phase was observed in the range ϕ_{add} = (0.05-0.09) free energy calculations indicate that this phase is a long lived metastable and that the stable phase in this region of the phase diagram is the PL phase [e.g., for ϕ_{add} = 0.06, βg^{O52}=17.57(1) and βg^{PL}=17.55(1)]. However, the very small difference in molar Gibbs free energy between these two phases (i.e., PL and O^{52}) together with the fact that simulations are only carried out in discrete points of the phase diagram, suggests that this result should be taken with caution; there could still be a very narrow region of the phase diagram where the O^{52} phase is stable. Moreover, the potential existence of the O^{52} phase as a long-lived metastable phase is also of interest since metastable phases are often observed in experiments (e.g., the PL phase in pure DBC melts[11]). In a similar note, at ϕ_{add} =0.40 the RG phase was observed in a cubic simulation box of size *Lbox* = 39 lattice units, with a calculated value of Gibbs energy of βg^{RG} = 4.595(2). In simulation boxes of sizes different than the latter, the RPL phase was always found. However the values of chemical potential for the RPL were always higher [e.g., *Lbox* = 35, βg^{RPL} = 4.600(2)], indicating the stability of the RG phase in this point of phase diagram. (Note that at ϕ_{add}=0.40 the mole fraction of nanoparticles is y^{nano} ~ 0.93, hence, the low values of the molar Gibbs energy of the mixture).

Although, the addition of small nanoparticles induced the formation of a variety of morphologies, neither the DD phase nor the P phase were observed. The reason for the absence of these phases can be explained in terms of spatial distribution of the nanoparticles throughout the minority (A-component) domain. In order to

achieve the stabilization of the bicontinuous phases, the nanoparticles need to preferentially reside inside the nodes (Fig. 3.1b). However, given the small size of the nanoparticles, it is reasonable to think that confining the nanoparticles to small regions (e.g., the nodes) of the A domain would produce a significant penalty to the entropy of mixing. Therefore, nanoparticles would tend to distribute uniformly throughout the minority component domain. This tendency can be observed in Figure 3.6a, where we show a typical snapshot of the L phase with nanoparticle concentration ϕ_{add} =0.20. Figure 3.6b shows the concentration profiles of A-block beads and nanoparticle beads along the direction perpendicular to the Lamellae. The concentration of nanoparticles is seen to vary less rapidly than the concentration of A-block beads as the interface is approached, consistent with the higher tendency of the nanoparticles to distribute uniformly in the A domain. Moreover, as the interface is approached, the concentration of nanoparticles increases relative to that of A-block beads to the point that nanoparticles are also present in finite concentrations (despite the energetic penalty implied) inside the B-component domain. This illustrates the importance of the nanoparticle mixing entropy contribution to the total free energy. As a consequence, the small solvent-like nanoparticles studied in this work are not likely to locate preferentially inside the nodes of a bicontinuous phase, thereby failing to stabilize either the DD phase or the P phase through reduction of packing frustration. It is also instructive to note, that since the nanoparticles tend to distribute uniformly in the A-component domain, the net effect of adding nanoparticles is to increase the effective size of the minority component block of the DBC (i.e., swelling the whole A-component block), hence decreasing the preferred mean curvature of the A-B interface. This is consistent with the observed progression of stable phases in which the system goes, with increasing ϕ_{add}, from the G phase (i.e., positive mean curvature)

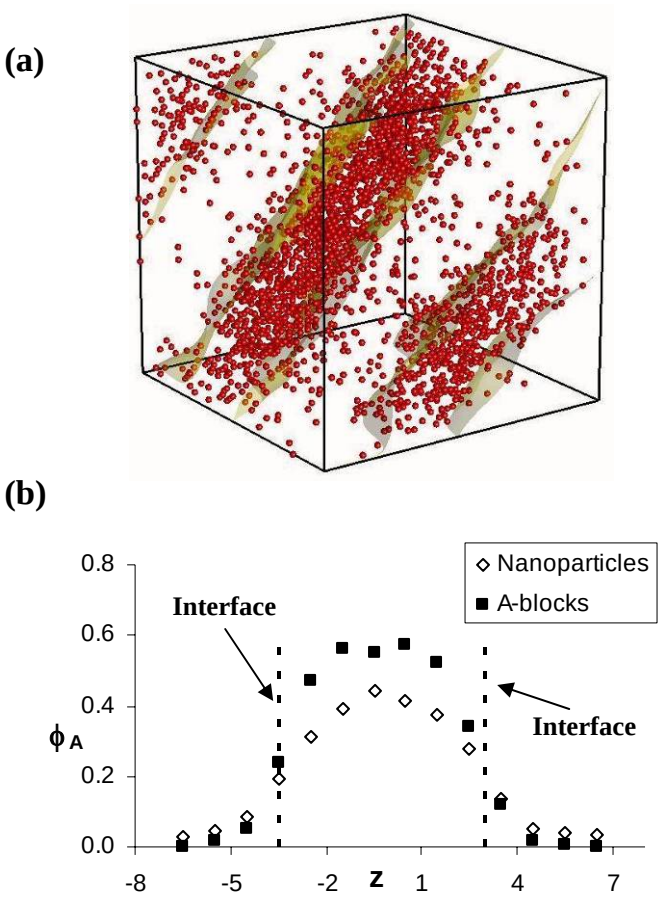

Figure 3.6. Distribution of small nanoparticles in simulated L phase at ϕ_{add}=0.20. (a) Typical snapshot of the simulated L phase. For clarity, copolymer beads are not shown. Nanoparticles are shown in red (dark). Surfaces dividing the A and B domain are shown as a guide to the eye. (b) Concentration profiles along the direction perpendicular to the Lamellae is shown for the A-block beads and nanoparticle beads. Nanoparticle concentration varies less rapidly than A-block bead concentrations, indicating that the nanoparticles tend to distribute homogeneously throughout the A-component domain. Non-negligible amounts of nanoparticles can also be found in the B-component domain. A similar behavior is observed (results not shown) for the other nanoparticle-stabilized phases (e.g., G, O[52], PL and RPL).

to the L phase (i.e., zero mean curvature) and then to the RG phase (i.e., negative mean curvature).

Addition of homopolymer

In this section, we study the possibility of reducing packing frustration in the ordered bicontinuous phases by addition of A-component homopolymer of size N_{ho} = 16. The choice of this homopolymer size is a compromise between two opposite factors: 1) The smaller the homopolymer chains, the greater the mixing entropy penalty that is incurred in order to confine the homopolymer inside the nodes. Accordingly, longer homopolymer chains should favor the formation of bicontinuous phases. 2) The longer the homopolymer chains, the greater the dislike between the homopolymer and the DBC chains, thus increasing the tendency of macro-phase separation into a DBC-rich phase and a homopolymer-rich phase; this hinders the possibility of obtaining multiple bicontinuous phases. Thus, our choice of homopolymer chain size is consistent with the SCFT calculations of Matsen[25] where it was found that these two criteria can be met, in order to stabilize the DD phase, when the ratio (α) of homopolymer chain length to DBC chain length is around $2/3 \le \alpha \le 1$.

The phase behavior of the DBC/homopolymer system was studied for values of homopolymer volume fraction (ϕ_{add}) in the range ϕ_{add}~[0.0-0.45]. A very complex phase behavior was observed, which is shown in Figure 3.7. As before, all the morphologies spontaneously formed for a given value of ϕ_{add} are shown. Phase boundaries between stable phases are roughly delineated based on the free energy calculations.

As expected, for low homopolymer concentration ϕ_{add}~(0.0-0.10) the G phase was observed. In addition, for a wide range of concentrations ϕ_{add}~(0.00-0.40) the C phase was obtained. For values of $\phi_{add} \ge 0.02$, the ordered bicontinuous DD phase was

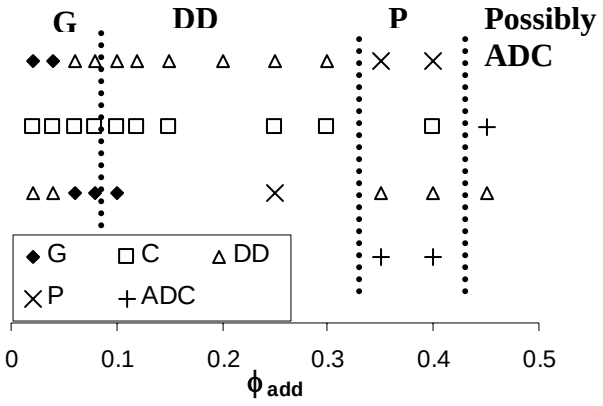

Figure 3.7. Simulated phase diagram for the DBC/homopolymer system. All the morphologies obtained at a particular value of ϕ_{add} are shown. Chemical potential calculations are used to discern stability between competitive phases and to delineate approximate phase boundaries. In general a progression of morphologies of the form G →DD→P was observed. Also, a possibly stable morphology of "Alternating Diameter Cylinders" (ADC) wherein cylinders pack tetragonally was observed.

also observed. In Figure 3.8a a snapshot of eight unit cells of the simulated DD phase is shown. As is customary throughout this work, the B-component domain is not shown. The minority (A) component forms two interweaving networks that never intersect. Figure 3.8b shows a single node of the simulated DD phase; as expected, four tubes (connectors) intersect in each node. In order to ratify the simulated morphology as the DD phase, the structure factor *S(q)* was calculated (Figure 3.9) to show that the location of the peaks at ratios $\sqrt{2}:\sqrt{3}:\sqrt{4}:\sqrt{6}$ is indeed consistent with the DD phase (i.e., Pn3m symmetry). To the best of our knowledge this constitutes the first time the DD phase is successfully obtained in particle-based simulations in DBC systems and at melt-like densities.

Since the DD has periodicity in the three directions its formation is very sensitive to the simulation box dimensions. As consequence the DD phase was only observed when simulation boxes were consistent with the DD unit cell size, which is a function of the thermodynamic conditions. For simulations with box dimensions inconsistent with the preferred DD unit cell size, other phases (e.g., C, G, etc) were formed depending on the value of ϕ_{add}. This dependence on simulation box dimensions of the observed structure is a general difficulty of particle-based simulations of all the ordered bicontinuous phases, since the "appropriate" unit cell size for each morphology at a given point of the phase diagram is not known a priori. Thus, in principle an extremely large number of simulation box sizes (and shapes in the case of orthorhombic phases) would need to be tried to be able to observe all the competitive morphologies. This approach is obviously not feasible and physical intuition together with some degree of trial-and-error process are necessary to constrain the search to only simulation box sizes consistent with the morphologies that are most likely to have the lowest free energy. In order to estimate the unit cell size of the different candidate morphologies from data obtained at a different value of ϕ_{add} or from another

(a)

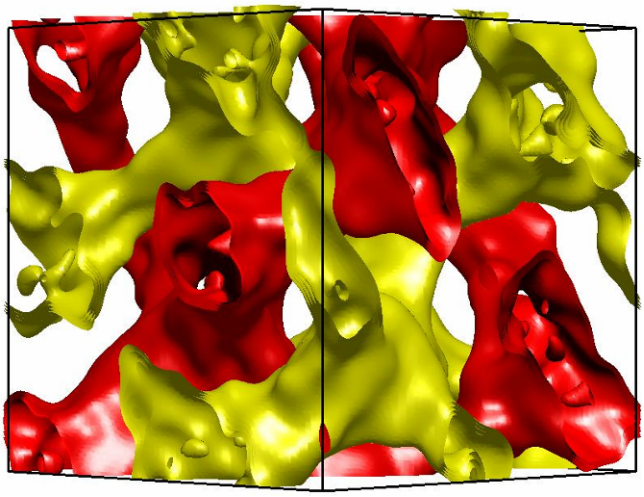

(b)

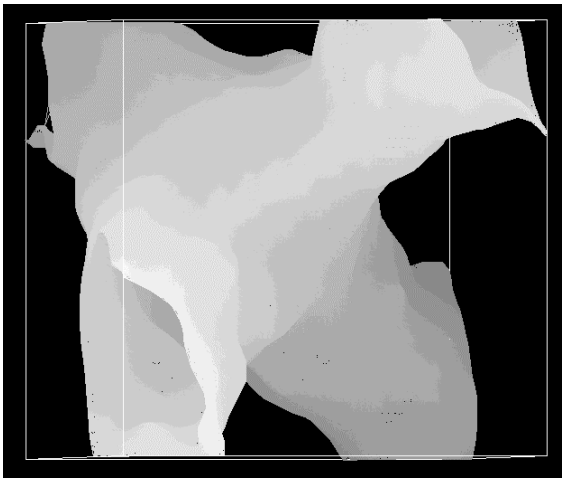

Figure 3.8. Snapshot of a simulated DD phase for the DBC/homopolymer system at ϕ_h = 0.20. (a) Eight (8) unit cells of the simulated DD phase The unit cell size of the shown snapshot is L = 30 lattice units. The B-component domain is not shown for clarity. The two minority component networks are shown in red(dark) and yellow(light) for clarity. (b) A single DD node, where the four connectors are seen to intersect.

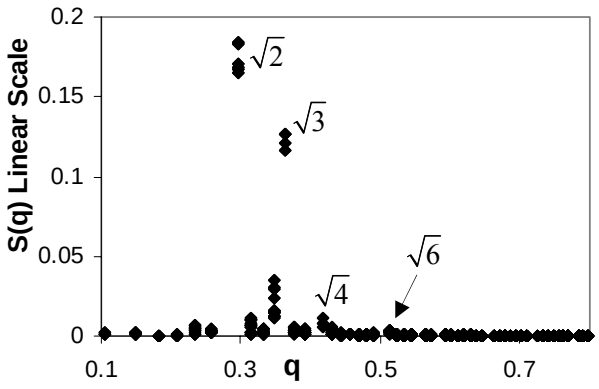

Figure 3.9. Structure factor *S(q)* for the simulated DD phase. The location of the peaks at ratios $\sqrt{2}:\sqrt{3}:\sqrt{4}:\sqrt{6}$ is consistent with the Pn3m symmetry.

bicontinuous morphology, we found it helpful to use simplified theoretical models for the geometry of bicontinuous phases. The simplest physical model to represent ordered bicontinuous phases is the "constant thickness" or "parallel surfaces" model,[4, 17] in which the A-B interfaces are assumed to lie at a constant perpendicular length λ from the minimal surface (e.g., G, DD, P surfaces) which is imagined to divide the B-component domain in two halves. In this model, the B-component volume fraction ϕ_B is related to length λ by the simple relation:[17]

$$\phi_B = 2A_o\left(\frac{\lambda}{L}\right) + \frac{4\pi\chi_e}{3}\left(\frac{\lambda}{L}\right)^3 \tag{36}$$

where L is the preferred unit cell size and A_o and χ_e are the normalized area per unit cell and the Euler characteristic, respectively, for the particular minimal surface. For the DD phase A_o=1.919 and χ_e= -2; while for the P phase, A_o=2.345 and χ_e= -4.[48] The first term of eq. (36) corresponds to the value that ϕ_B would be if the minimal surface were flat (i.e., gaussian curvature K = 0) and the second term to the correction due to the non-zero value of K. In Figure 3.10, we show the simulation box sizes where the DD phase was spontaneously obtained as a function of the homopolymer volume fraction ϕ_{add}, which is related to ϕ_B through,

$$\phi_B = 1 - \phi_A = 1 - \left[f\left(1 - \phi_{add}\right) + \phi_{add} \right] \tag{37}$$

where f =0.30 is the DBC composition. Additionally, Figure 3.10 shows the fit provided by eq. (36) with a single adjustable parameter λ that represents the half-width of the B-component domain. For the DD phase we found λ = 4.46 lattice units, which is about 0.75 times the observed B-block end-to-end distance (r_B) for the DD phase and agrees with the intuitive idea that the width of the B domain should lie in between those expected for a monolayer and a bilayer (i.e., $r_B/2 < \lambda < r_B$). Similar values of λ were obtained for the G phase (e.g., λ=4.32) and the P phase (e.g., λ=4.52)

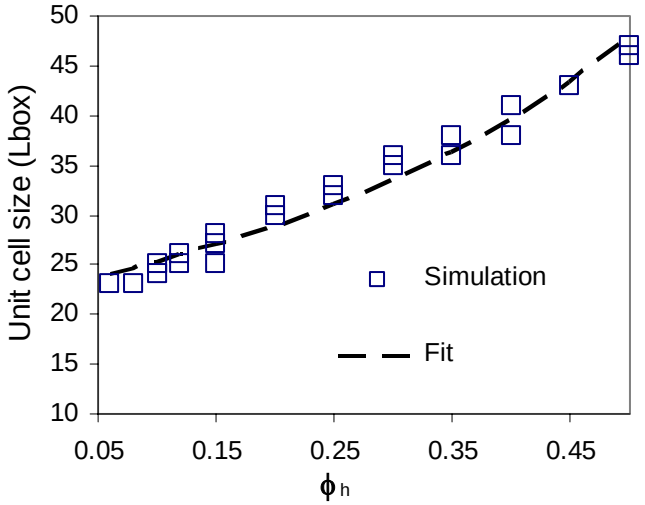

Figure 3.10. Simulation box dimensions (of one unit cell), wherein the DD phase was spontaneously formed, as a function of the homopolymer volume fraction ϕ_{add}. A single-parameter (λ) fit using eq. (36) is also shown. The fitted value of $\lambda = 4.45$ represents the half-width of the B-component domain..

indicating that the B-component domain width is almost independent of the bicontinuous morphology. It can be seen in Figure 3.10 that the simulation box size dependence in ϕ_{add} agrees well with the expected behavior for the constant thickness model of the DD phase. A similar agreement (results not shown) was also observed for the other bicontinuous phases. Moreover, the good agreement between the simulation results and eq. (36) indicates that λ remains approximately constant for the different values of ϕ_{add}. This trend can only be explained if the homopolymer does not penetrate into the B-component domain, a behavior that we have indeed observed in our simulations (see later the discussion on Figure 3.16).

In the range $0.02 \leq \phi_{add} \leq 0.40$ both the DD phase and the C phase were spontaneously obtained depending upon simulation box size. For $\phi_{add} < 0.05$ both of these phases are just metastable since the G phase has lower values of Gibbs energy [e.g., at $\phi_{add}=0.04$, $\beta g^{G}=35.70(1)$, $\beta g^{C}=35.76(1)$ and $\beta g^{DD}=35.81(1)$]. However, for the range $0.05 < \phi_{add} < 0.35$ the DD and C phases seem to compete for thermodynamic stability. For relatively high concentrations of homopolymer (i.e., $\phi_{add} > 0.12$) the Gibbs energy of the DD phase is found to be slightly lower than that of the C phase [e.g., for $\phi_{add} = 0.25$, $\beta g^{DD}= 32.597(9)$ and $\beta g^{C}=32.62(1)$]. Additionally, for these concentrations, defect free C phases become increasingly difficult to stabilize, thus making unambiguous the assignment of the DD phase as the stable one. However, for a narrow range of homopolymer concentrations (i.e., $0.05 < \phi_{add} < 0.12$), free energy calculations seem to indicate that the C phase has a lower Gibbs energy than the DD phase [e.g., for $\phi_{add} = 0.08$ and $Lbox = 48$, $\beta g^{DD}=35.175(10)$ and $\beta g^{C}=35.15(1)$]. The stabilization of the C phase (a phase with much greater mean curvature in the A-B interface than the G phase) with the addition of homopolymer is somewhat counterintuitive. However, this could be the consequence of an incomplete alleviation of the frustration in the DD nodes, because of the relatively small amounts of

homopolymer present in this region of phase diagram (i.e., $0.05<\phi_{add}<0.12$). Nonetheless, to the best of our knowledge, a similar transition (i.e., from the G phase to the C phase by adding minority component) has neither been observed experimentally nor predicted by theory. It is also plausible that the stable state in this narrow region of phase diagram is a two-phase state where the G and DD phases coexist, which would not be attainable in the relatively small simulation boxes used in this work, therefore causing the stabilization of a single metastable phase which in this case happens to be the C phase. Moreover, the C morphologies with the lowest Gibbs energy were usually the ones with the cylinders aligned along a diagonal of the simulation box. This suggests that C configurations are subject to "tensions" (i.e., anisotropies in the pressure tensor) that could cause a non-negligible penalty in the PV contribution to the Helmholtz free energy. Because of the above reasons, in this region of the phase diagram, we tentatively assign the C phase as metastable. Finally, in order to estimate the phase boundaries between the stable phases (i.e., the G and DD phases), we present in Figure 3.11 the Gibbs free energy of the G and DD phases as a function of ϕ_{add}, wherein it can be seen that the values of βg for both phases intersect around ϕ_{add} ~0.09.

For homopolymer volume fractions in the range $0.25<\phi_{add}<0.40$ the Plumber's Nightmare (P) phase was also observed. To the best of our knowledge this phase has never been observed before in simulations of DBC systems. In this morphology, the minority component forms two networks that never intersect, and each network is composed of six-fold nodes and connectors (Figure 3.12). Calculation of *S(q),* in Figure 3.13 confirms that the simulated phase is indeed the P phase (i.e., Im3m symmetry)[27] as can be seen from the clear peaks at positions $\sqrt{2}:\sqrt{4}:\sqrt{6}$. For homopolymer concentrations $\phi_{add} \leq 0.30$ the simulated P phases became defective after long simulation runs (i.e., more than 4×10^6 MC steps) indicating that for these

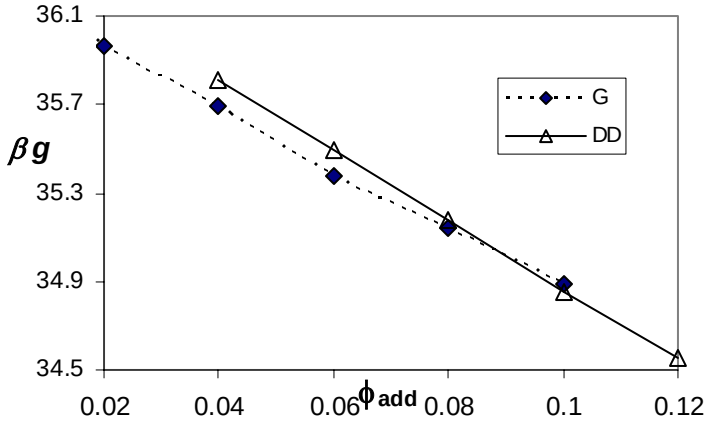

Figure 3.11. Gibbs free energy of the mixture (βg) for the G and DD phases in the DBC + homopolymer system as a function of the homopolymer volume fraction ϕ_{add} in the range ϕ_{add} ~(0.02-0.12). The G phase is stable only for $\phi_{add} < 0.09$.

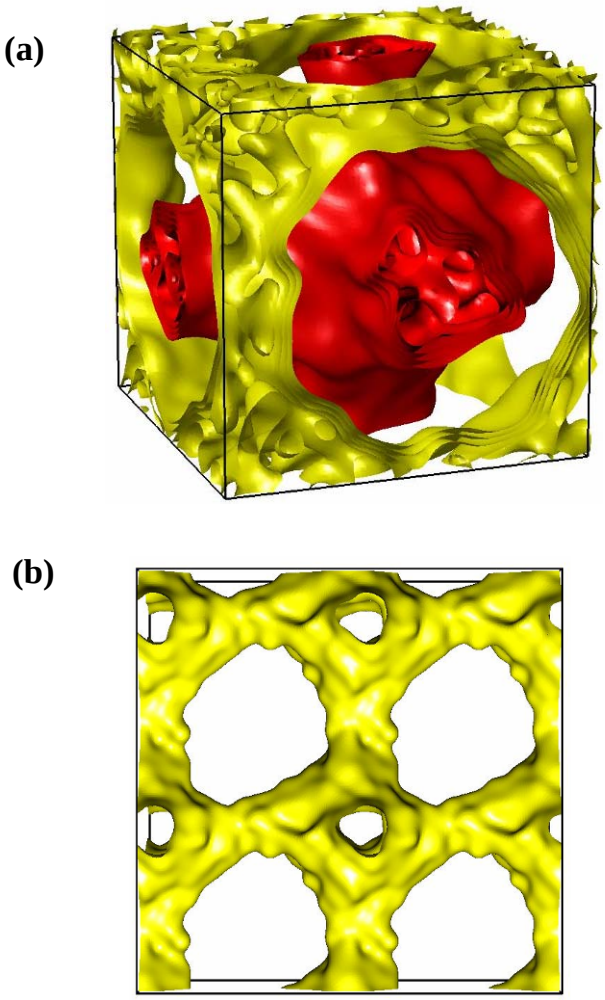

Figure 3.12. A simulated snapshot of the Plumber's Nightmare (P) phase observed at ϕ_{add} =0.35 in a simulation box of size *Lbox* = 46. The majority (B) component is not shown. (a) One unit cell of the P phase. The minority component forms two distinct networks that never intersect. They are shown in yellow(light) and red(dark) for visualization purposes. (b) One of the minority component networks has been replicated four (4) times.

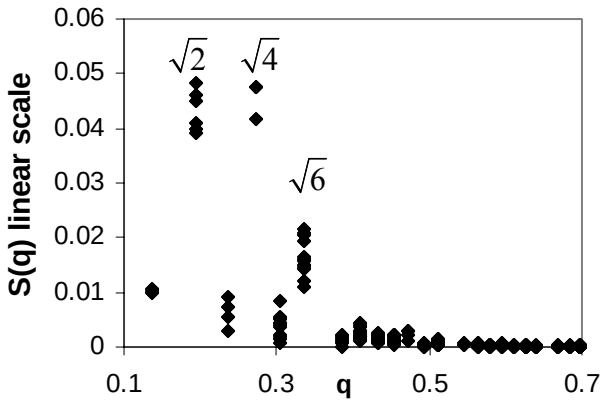

Figure 3.13. Structure factor *S(q)* for the simulated P phase. The location of the peaks at ratios $\sqrt{2}:\sqrt{4}:\sqrt{6}$ is consistent with the Im3m symmetry that is expected for the Plumber's Nightmare phase.

conditions the P phase is just metastable. However, in the range $0.35 \leq \phi_{add} \leq 0.40$ the simulated P phase not only remained defect free but additionally was observed to have a slightly lower Gibbs energy than the DD phase [e.g., for $\phi_{add} = 0.35$, βg^{DD}=31.19(1) and βg^{P}=31.18(1)]. Moreover, when "bigger" systems were used (e.g., at $\phi_{add} = 0.40$, box dimensions of: 41×82×82 for the DD phase and 49×98×98 for the P phase) such that the unit cells of the P and DD phases were replicated four times, the P phase still showed lower values of βg. As a consequence, we conclude that in the range $0.35 < \phi_{add} < 0.40$ the P phase is the stable phase.

For homopolymer volume fractions $\phi_{add} > 0.35$, a novel phase, in which cylinders of two different diameters alternate in a tetragonal (square) packing, was observed (Figure 3.14). This phase will be, henceforth, referred to as "Alternating Diameter Cylinders" (ADC). Although chemical potential calculations in the range $0.35 < \phi_{add} < 0.40$ indicate that the ADC phase is just a long lived metastable phase, the results seem to suggest that for $\phi_{add} \sim 0.45$ the ADC phase may be stable since it has a lower chemical potential than the other phases observed. However, this result should be taken with caution because most of the other phases observed at these conditions were defective, presumably because of the much longer equilibration times required for the large simulation boxes involved (e.g., at ϕ_{add}=0.45 $Lbox > 51$ for the P phase). Moreover, at these high values of ϕ_{add} it is also possible that other bicontinuous phases [e.g., C(P), I-WP, etc.[49]] could become stable. These phases, however, would have unit cell sizes far beyond those accessible in the present study [e.g., at ϕ_{add}=0.45, $Lbox \sim 80$ for the Neovius' surface phase estimated with eq. (36)] and are outside the scope of the present work. Nevertheless, even in the worst case scenario wherein the ADC phase is just a long-lived metastable we still think this phase is of significant importance for several reasons: 1) Long lived metastable phases are often observed experimentally, 2) Under different conditions (e.g., different thermodynamic

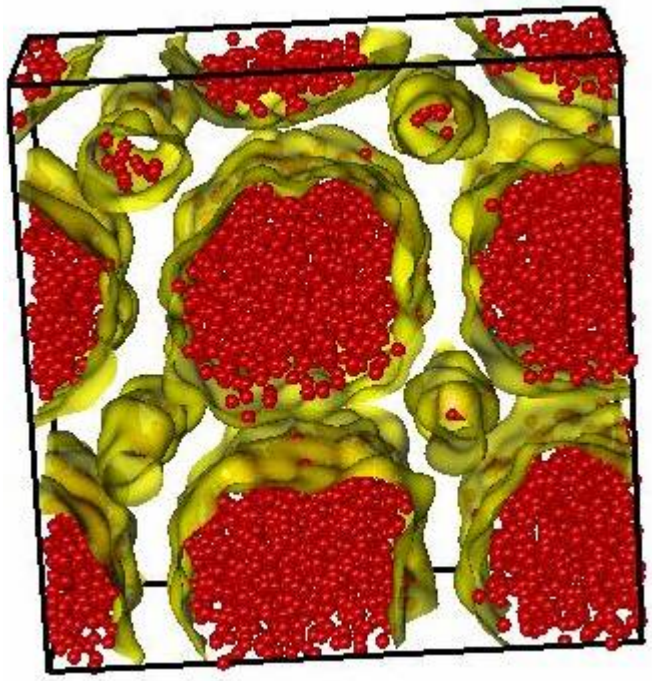

Figure 3.14. A simulated snapshot of four (4) unit cells of the "Alternating Diameter Cylinder" (ADC) phase. The majority component is not shown. The A-B interface is shown in yellow(light), while the centers of mass of the homopolymer chains are presented in red(dark). This snapshot was obtained at $\phi_{add} = 0.40$ where the unit cell size is L=39. The "thick" cylinders interior is rich in homopolymer chains while the "thin" cylinders present a much lower homopolymer concentration in their interiors. Cylinders pack tetragonally.

conditions, different model, or when subject to shear) this phase might be stabilized, and 3) The fact that the cylinders are arranged in a tetragonal packing gives insight about why the "ordinary" C phase is not stable in this region of the phase diagram. At high values of ϕ_{add}, if all the cylinders had the same diameter, packing frustration of the B-block would be prevalent in the corners of the Wigner-Seitz cell of the hexagonally packed cylinders. This is because the mean end-to-end distance of the B-blocks would be much smaller than the radius of the cylinders. This is evident in Figure 3.14 where it can be readily seen that the average B-domain distance separating two consecutive cylinders is much less than the diameter of the thick cylinders. It is interesting to note that the penalty in mixing entropy incurred by segregating the homopolymer in this way (i.e., having homopolymer-rich cylinders and DBC-rich cylinders) seems to be outweighed by the gain in conformational entropy of the B-block.

It has been argued that the reason for the lack of multiple ordered bicontinuous phases in pure DBC melt systems is the presence of packing frustration inside the nodes, which can be manifested in the form of void in the nodal centers,[21] chain stretching,[22] deformation of the nodes shape,[20] or more likely a combination of all the above factors. We have now shown here that by the addition of a component with the right characteristics, multiple bicontinuous phases (e.g., DD and P phases), can be stabilized. In order to link this stabilization to reduction in the packing frustration inside the nodes, we show in Figure 3.15a a single node of a typical snapshot of the simulated P phase, where the A-B interface in yellow(light) has been made transparent in order to show the centers-of-mass of the homopolymer chains in red(dark). Additionally, Figure 3.15b shows a plot of the volume fraction of the A-block and homopolymer beads as a function of the distance from the center of the P phase nodes. It can be seen from the figure that the homopolymer chains reside preferentially inside

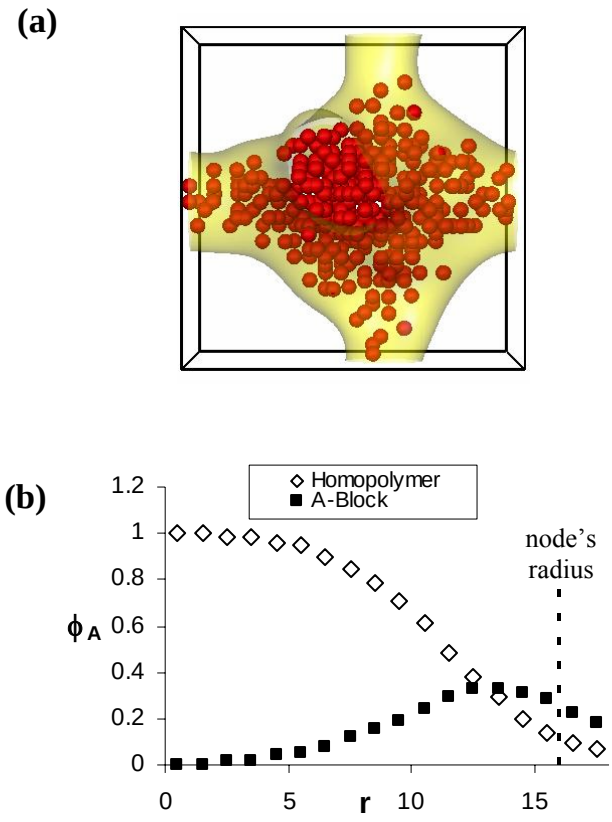

Figure 3.15. A typical snapshot of a single node of the P phase obtained at ϕ_{add} =0.25 and *Lbox* = 41. (a) The A-B interface in yellow(light) is made transparent and the centers of mass of the homopolymer chains are shown in red(dark). (b) Average volume fraction of homopolymer beads and A-block beads as a function of the distance from the nodes. The homopolymer chains concentrate in the center of the node in order to reduce packing frustration. Similar behavior was observed in all the snapshots we examined.

the nodes where they are found in much higher concentration (i.e., $\phi \sim 1.0$) than in the connectors. Moreover, since the concentration of DBC chains in the center of the nodes is essentially zero, absence of the homopolymer chains would clearly cause packing frustration because the DBC chains would need to stretch and the node would have to deform in order to diminish the void in the center of the nodes. A similar behavior is observed for the DD phase (results not shown); however, for a given value of ϕ_{add} the segregation towards the nodes of the homopolymer chain is more dramatic in the case of the P phase than in the DD phase. This is consistent with the hypothesis that since the P nodes are bulkier (e.g., at ϕ_{add} =0.25, $r_{node} \sim 16$ for the P phase, and $r_{node} \sim 12$ for the DD phase), the DBC packing frustration would be more drastic for the P phase if there were no homopolymer inside the nodes. Although a gradient of homopolymer concentration implies a loss of mixing entropy, yet again, for this size of homopolymer, the gain in conformational entropy for the DBC chains seems to partially outweigh this loss. Moreover, analysis of the mean square end-to-end distance $\langle r^2 \rangle$ of the homopolymer chains inside and outside the nodes [e.g., $\langle r^2 \rangle_{tube}$=29.5(9) and $\langle r^2 \rangle_{node}$=35.5(9)], and comparison with the $\langle r^2 \rangle$ observed in a melt of the pure homopolymer [e.g., $\langle r^2 \rangle_{melt}$=35.3(1)], reveals that the homopolymer in the tubes is forced to adopt unfavorable, more compact conformations (due to the smaller size of the tubes relative to the nodes). This indicates that the segregation of the homopolymer towards the nodes may also be understood from the perspective of the homopolymer sacrificing translational entropy in order to gain conformational entropy, which for this size of homopolymer is expected to have a more important impact to the total free energy.

Discussion on the origins of complex phase behavior

Although it is clear that reduction of chain stretching inside the bicontinuous phases' nodes (frustration relief) by addition of homopolymer should make these morphologies less unfavorable, it certainly does not guarantee that these phases should become the stable ones, as observed in this work. Moreover, packing frustration alone cannot explain the complex progression of phases observed with increasing ϕ_{add}, because just as the homopolymer reduces the frustration in the DD phase so does it in the G phase and there would not be any driving force for phase transitions to occur.

In order to understand the observed phase transitions, it is convenient to evoke the origins of curvature in the DBC systems. The morphologies observed in DBC systems are the result of the competition between energetic and entropic contributions to the free energy. In order to decrease the interfacial energy the system tries to approach morphologies of zero mean A-B interface curvature (H), however, if the two blocks are of different sizes, imposing $H = 0$ forces the blocks to adopt unfavorable configurations in order to fill space, creating an entropically unfavorable scenario (i.e., packing frustration). Thus, the resulting equilibrium morphology possesses an A-B interface that *tries* to approach a constant mean curvature surfaces (CMC). The preferred value of mean curvature (H^{pre}) depends upon the relative size of the two blocks as is observed in the pure DBC system where the curvature of the interface is progressively increased with the asymmetry of the two blocks, going from the L phase (i.e., $H = 0$) when the blocks are symmetric, to the S phase, with a high value of H, when the blocks are highly asymmetric.

For a specific relative size of the blocks in a DBC chain (i.e., for a given value of f) the preferred value of H can be modified by adding a second component that "likes" the minority component blocks. For example, as we showed above, adding selective small nanoparticles can induce a variety of structures with different values of

H, because the small nanoparticles, driven by their high entropy of mixing, distribute almost homogeneously in the A-component domain, causing the swelling of the A-blocks and thus increasing their effective size. In other words, since the nanoparticles "penetrate" into the DBC layer, the net effect of adding them is akin to increasing the A-block size. Conversely, if the selective "additive" does not penetrate into the DBC layer, the A-blocks will not augment their effective size and the preferred value of *H* will remain mostly unchanged. Whether an additive distributes homogeneously inside the A-component domain or not is again a competition between energetic and entropic terms.[2] The interfacial energy tends to "push" the additive away from the interface, concentrating the additive in the center of the A-domain. The entropy of mixing tends to favor configurations wherein the additive is spatially distributed in a uniform fashion. For the small solvent-like nanoparticles the entropic contributions tend to outweigh the energetic ones causing their penetration into the DBC layer. However, for the homopolymer chains used in this study, the total entropy does not primarily arise from translational degrees of freedom (as with the nanoparticles), but mainly from the chain conformations. The homopolymer can then be expected to have a much lower entropy of mixing (associated with the translational degrees of freedom), so that the energetic contributions should be dominant and the homopolymer chains should not significantly penetrate the DBC layer. This is indeed what is seen in the simulations. Figure 3.16a shows a typical snapshot of the C phase, where the centers of mass of the homopolymer chains are represented by the red(dark) beads, while the centers of mass of the A-blocks are presented in yellow(light). Figure 3.16b presents the volume fraction of homopolymer beads and A-block beads as a function of the distance from the cylinder axis. The homopolymer significantly concentrates in the center of the cylinders while most of the A-blocks just surround the homopolymer.

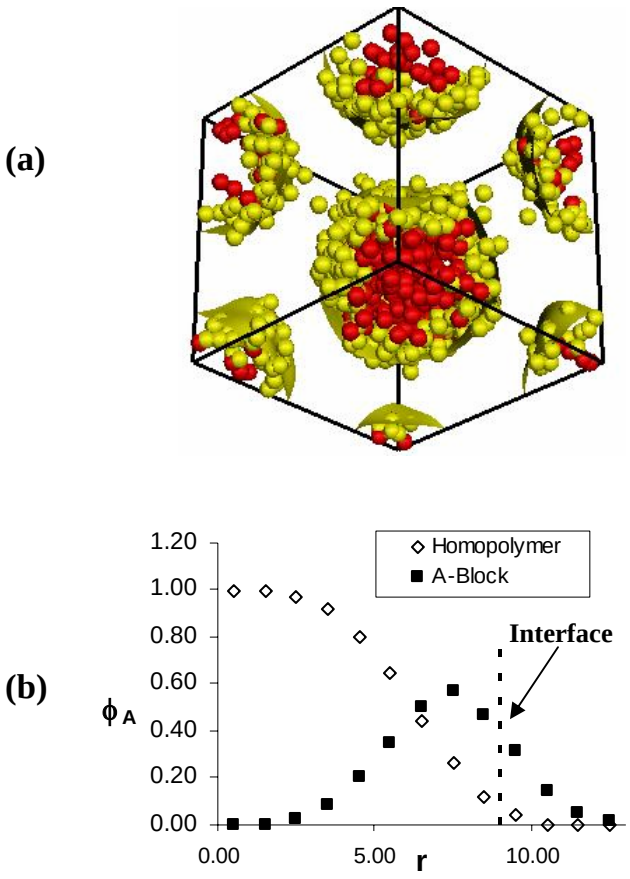

Figure 3.16. A typical snapshot of a metastable C phase observed at ϕ_{add}=0.25. The C phase offers a valuable opportunity to observe the inhomogeneous distribution of the homopolymer chains throughout the A-component domain. (a) The centers of mass of the A-blocks of the DBC chains are shown [i.e., yellow(clear) beads], while the centers of mass of the homopolymer chains are represented by the red(dark) beads. The A-B interface is also shown in yellow(clear) for reference (b) Average volume fraction of homopolymer beads and A-block beads as a function of the distance from the cylinder axis. The homopolymer does not distribute uniformly but prefers the center of the A-component domain.

Though this effect is most easily visualized in the C phase, the same trend is observed for all the other phases. Finally, we can postulate that, given that the homopolymer does not significantly penetrate the DBC layer, adding homopolymer should not significantly decrease the preferred value of H.

For a given morphology the actual value of the A-B mean curvature (H^{act}) can be estimated using the parallel surface model, for which it can be shown that:[17]

$$H^{act} \approx \left(\phi_B\right)^2 \Big/ \gamma\lambda \tag{38}$$

where γ is dimensionless constant particular to each minimal surface and λ represents the half-width of the B-component domain which is found to remain approximately constant [cf., Eq. (36) and discussion thereof]. From this relation, it is seen that for a given morphology, the actual value of the interfacial curvature decreases in proportion to the square of the B-component volume fraction ϕ_B [and ϕ_B decreases as ϕ_{add} increases, cf. Eq. (37)]. Adapting the argument that Ström and Anderson[17] used to explain the phase behavior of surfactant systems to the case of DBC melts, we postulate that the stable morphology is going to be the one that, while minimizing packing frustration, presents an *actual* value of the interfacial mean curvature (H^{act}), that is the closest possible to the *preferred* value H^{pre}.

At this point, we get to the root of the origin of the contrasting difference between the phase behavior observed when adding small nanoparticles and when adding homopolymer: the addition of small nanoparticles significantly decreases H^{pre} while the addition of homopolymer leaves H^{pre} mostly unchanged. For any selective additive, it is expected that the degree of penetration should increase with the additive concentration (i.e., because of the higher gradients), hence H^{pre} should always decreases with additive concentration.[17] However, it is the difference in the rate at which H^{pre} decreases, which causes the contrasting phase behavior observed in the two

types of systems studied. If the value of H^{pre} decreases *faster* than H^{act} with increasing concentration of additive (e.g., small nanoparticles case), the system progresses towards phases of less curvature. Conversely, if H^{pre} decreases slower than H^{act} with increasing concentration of additive (e.g., homopolymer case), the system progresses towards phases of more curvature.

The complex phase behavior observed with the addition of homopolymer can be now understood in terms of our postulate. First, let us establish that for a given value of ϕ_{add} the candidate phases can be sorted in the following manner with increasing curvature:[17] G→DD→P→C(P)→C. For small values of ϕ_{add} the system is just a slightly perturbed from the pure system and the G phase is stable. However, when the value of ϕ_{add} starts to increase, H^{act} decreases rapidly, departing from H^{pre} which stays approximately constant; therefore, causing the G phase to become unstable. In order to approach a value of mean curvature closer to H^{pre} the system needs to undergo a phase transition to a new morphology of higher curvature. The next morphology in the list is the DD phase which, given the presence of the homopolymer and its tendency to concentrate in the nodes, is no longer limited by packing frustration and is therefore stabilized. When more homopolymer is added, H^{act} continues to decrease until again it departs significantly from H^{pre} and the P phase, whose frustration has again been relieved by the significant amounts of homopolymer added, becomes stable. As even more homopolymer is added, new phase transitions are expected to occur. The next phase in the list is the C(P) phase which as mentioned above would have unit cell sizes too large to be observed in the present study. Nevertheless, it is indeed observed that for high values of ϕ_{add} the ADC phase which presents a highly curved A-B interface spontaneously forms, consistent with the postulate of stabilization of phases of increasing curvature. As pointed out before, for high homopolymer concentrations, packing cylinders hexagonally as required for the

C phase causes packing frustration in the B-blocks. Therefore, it is natural to assume that the stabilization of the ADC phase could be the result of a compromise between the system's need to achieve a highly curved interface like in the C phase and at the same time minimize packing frustration.

V. CONCLUSIONS

We performed a lattice MC study of two different strategies for reducing packing frustration in the ordered bicontinuous phases' nodes by means of the addition of minority (A) component. While the first strategy consisted of the addition of small solvent-like selective nanoparticles, the second strategy involved addition of homopolymer of a length 80 % that of the DBC chains.

The addition of small nanoparticles induced a progression of phases of the form G→PL→L→RG, in which the A-B interface curvature is observed to decrease monotonically with increasing nanoparticle volume fraction (ϕ_{add}). Additionally, in the same region of phase diagram where the PL phase was found stable, the orthorhombic co-continuous network O^{52} phase was observed, albeit as a long-lived metastable.

A radically different phase behavior was observed with the addition of homopolymer, in which phases of greater curvature than the G phase were stabilized. In general the observed sequence of phases, for increasing homopolymer concentration, was G→DD→P, with the novel ADC phase being possibly stable after the P phase. To the best of our knowledge this is the first time that the ordered bicontinuous DD and P phases are simulated and predicted to be stable in DBC melt systems using particle-based simulations. Examination of the structure of the ordered bicontinuous phases showed that the homopolymer preferentially locates in the center of the nodes, not only preventing the packing frustration that would otherwise exist but additionally allowing for a gain in homopolymer's conformational entropy.

The contrastingly different phase behavior observed for the two strategies was explained in terms of their difference in the rate of change of H^{act} relative to H^{pre} with increasing additive concentration. This difference originates from the different degrees of penetration of the two additives into the DBC layer, which are ultimately caused by the differences in translational (mixing) entropy between the homopolymer and the solvent-like nanoparticles. It is interesting to note that for the currently studied system the DD phase is stable for an extraordinarily wide range of homopolymer concentrations (i.e., $0.09<\phi_{add}<0.30$). This suggests that the homopolymer length adopted here leads to a degree of penetration (into the DBC layer) which is to some extent "optimal" to stabilize the DD phase. Thus, it can be envisioned that "optimal" sizes of additive can be found for which the composition range of stability of a particular bicontinuous phase is maximized.

In future work we will explore the possibility of provoking transitions between different complex phases by rationally controlling the additive's mixing entropy (and hence its degree of penetration into de DBC layer) through changes in the additive's architecture and chain-length, while keeping constant the additive's volume fraction.

ACKNOWLEDGMENTS

We are grateful to Professors Eric W. Cochran and Frank S. Bates for providing visualization models of the O^{52} and O^{70} phases. We also thank Professor U. Wiesner for stimulating conversations and for introducing us to the issues associated with the stabilization of the P phase in block copolymer-inorganic hybrid systems. The support by the US Department of Energy, Grant No. DE-FG02-05ER15682, is gratefully acknowledged.

REFERENCES

1. Hamley, I. W., *The Physics of Block Copolymers*. Oxford University Press: **1998**.

2. Abetz, V.; Simon, P. F. W., Phase behaviour and morphologies of block copolymers. In *Block Copolymers I*, **2005**; Vol. 189, pp 125-212.

3. Matsen, M. W.; Schick, M. *Phys. Rev. Lett.* **1994,** 72, (16), 2660-2663.

4. Hajduk, D. A.; Harper, P. E.; Gruner, S. M.; Honeker, C. C.; Kim, G.; Thomas, E. L.; Fetters, L. J. *Macromolecules* **1994,** 27, (15), 4063-4075.

5. Schick, M. *Physica A (Amsterdam)* **1998,** 251, (1-2), 1-11.

6. Tyler, C. A.; Morse, D. C. *Phys. Rev. Lett.* **2005,** 94, (20), 208302.

7. Takenaka, M.; Wakada, T.; Akasaka, S.; Nishitsuji, S.; Saijo, K.; Shimizu, H.; Kim, M. I.; Hasegawa, H. *Macromolecules* **2007**.

8. Knoll, A.; Lyakhova, K. S.; Horvat, A.; Krausch, G.; Sevink, G. J. A.; Zvelindovsky, A. V.; Magerle, R. *Nat. Mater.* **2004,** 3, (12), 886-890.

9. Schultz, A. J.; Hall, C. K.; Genzer, J. *J. Chem. Phys.* **2002,** 117, (22), 10329-10338.

10. Matsen, M. W.; Griffiths, G. H.; Wickham, R. A.; Vassiliev, O. N. *J. Chem. Phys.* **2006,** 124, (2), 024904.

11. Hajduk, D. A.; Takenouchi, H.; Hillmyer, M. A.; Bates, F. S.; Vigild, M. E.; Almdal, K. *Macromolecules* **1997,** 30, (13), 3788-3795.

12. Matsen, M. W. *Phys. Rev. Lett.* **1998,** 80, (1), 201-201.

13. Andersson, S.; Hyde, S. T.; Larsson, K.; Lidin, S. *Chem. Rev.* **1988,** 88, (1), 221-242.

14. Uehara, H.; Yoshida, T.; Kakiage, M.; Yamanobe, T.; Komoto, T.; Nomura, K.; Nakajima, K.; Matsuda, M. *Macromolecules* **2006,** 39, (12), 3971-3974.

15. Kamperman, M.; Garcia, C. B. W.; Du, P.; Ow, H. S.; Wiesner, U. *J. Am. Chem. Soc.* **2004,** 126, (45), 14708-14709.

16. Cho, B. K.; Jain, A.; Gruner, S. M.; Wiesner, U. *Science* **2004,** 305, (5690), 1598-1601.

17. Strom, P.; Anderson, D. M. *Langmuir* **1992,** 8, (2), 691-709.

18. Hajduk, D. A.; Harper, P. E.; Gruner, S. M.; Honeker, C. C.; Thomas, E. L.; Fetters, L. J. *Macromolecules* **1995,** 28, (7), 2570-2573.

19. Matsen, M. W.; Bates, F. S. *J. Chem. Phys.* **1997,** 106, (6), 2436-2448.

20. Matsen, M. W.; Bates, F. S. *Macromolecules* **1996,** 29, (23), 7641-7644.

21. Martinez-Veracoechea, F. J.; Escobedo, F. A. *Macromolecules* **2005,** 38, (20), 8522-8531.

22. Martinez-Veracoechea, F. J.; Escobedo, F. A. *J. Chem. Phys.* **2006,** 125, (10).

23. Hasegawa, H.; Hashimoto, T.; Hyde, S. T. *Polymer* **1996,** 37, (17), 3825-3833.

24. Dotera, T. *Phys. Rev. Lett.* **2002,** 89, (20), 205502.

25. Matsen, M. W. *Macromolecules* **1995,** 28, (17), 5765-5773.

26. Matsen, M. W. *Phys. Rev. Lett.* **1995,** 74, (21), 4225-4228.

27. Finnefrock, A. C.; Ulrich, R.; Toombes, G. E. S.; Gruner, S. M.; Wiesner, U. *J. Am. Chem. Soc.* **2003,** 125, (43), 13084-13093.

28. Jain, A.; Toombes, G. E. S.; Hall, L. M.; Mahajan, S.; Garcia, C. B. W.; Probst, W.; Gruner, S. M.; Wiesner, U. *Angew. Chem., Int. Ed. Engl.* **2005,** 44, (8), 1226-1229.

29. Matsen, M. W. *J. Phys.: Condens. Matter* **2002,** 14, (2), R21-R47.

30. Fredrickson, G., *The Equilibrium Theory of Inhomogeneous Polymers*. Oxford University Press: New York, 2006.

31. Fredrickson, G. H.; Ganesan, V.; Drolet, F. *Macromolecules* **2002,** 35, (1), 16-39.

32. Larson, R. G. *J. Phys. II (Paris)* **1996,** 6, (10), 1441-1463.

33. Yu, B.; Li, B. H.; Sun, P. C.; Chen, T. H.; Jin, Q. H.; Ding, D. T.; Shi, A. C. *J. Chem. Phys.* **2005,** 123, (23), 234902.

34. Gonzalez-Segredo, N.; Coveney, P. V. *Europhys. Lett.* **2004,** 65, (6), 795-801.

35. Rychkov, I. *Macromol. Theory Simul.* **2005,** 14, (4), 207-242.

36. Hamley, I. W.; Castelletto, V.; Mykhaylyk, O. O.; Yang, Z.; May, R. P.; Lyakhova, K. S.; Sevink, G. J. A.; Zvelindovsky, A. V. *Langmuir* **2004,** 20, (25), 10785-10790.

37. Iacovella, C. R.; Keys, A. S.; Horsch, M. A.; Glotzer, S. C. *Phys. Rev. E* **2007,** 75, (4), 040801.

38. Chervanyov, A. I.; Balazs, A. C. *J. Chem. Phys.* **2003,** 119, (6), 3529-3534.

39. Huh, J.; Ginzburg, V. V.; Balazs, A. C. *Macromolecules* **2000,** 33, (21), 8085-8096.

40. Lin, Y.; Boker, A.; He, J. B.; Sill, K.; Xiang, H. Q.; Abetz, C.; Li, X. F.; Wang, J.; Emrick, T.; Long, S.; Wang, Q.; Balazs, A.; Russell, T. P. *Nature* **2005,** 434, (7029), 55-59.

41. Dotera, T.; Hatano, A. *J. Chem. Phys.* **1996,** 105, (18), 8413-8427.

42. Frenkel, D.; Smit, B., *Understanding Molecular Simulation*. Academic Press: San Diego, CA, 2002.

43. Lyubartsev, A. P.; Martsinovski, A. A.; Shevkunov, S. V.; Vorontsovvelyaminov, P. N. *J. Chem. Phys.* **1992,** 96, (3), 1776-1783.

44. Wilding, N. B.; Muller, M. *J. Chem. Phys.* **1994,** 101, (5), 4324-4330.

45. Bennett, C. H. *J. Comput. Phys.* **1976,** 22, (2), 245-268.

46. Trebst, S.; Huse, D. A.; Troyer, M. *Phys. Rev. E* **2004,** 70, (4), 046701.

47. Cochran, E. W.; Bates, F. S. *Phys. Rev. Lett.* **2004,** 93, (8), 087802.

48. Anderson, D.; Wennerstrom, H.; Olsson, U. *J. Phys. Chem.* **1989,** 93, (10), 4243-4253.

49. Anderson, D. M.; Davis, H. T.; Scriven, L. E.; Nitsche, J. C. C. *Adv. Chem. Phys.* **1990,** 77, 337-396.

CHAPTER 4

BICONTINUOUS PHASES IN DIBLOCK COPOLYMER/HOMOPOLYMER BLENDS: SIMULATION AND SELF-CONSISTENT FIELD THEORY*

I. INTRODUCTION

A great deal of attention has been given to diblock copolymer (DBC) systems due to their nano-scale self-assembling properties.[1] These systems can be rationally controlled to form regular mesoscopic morphologies that are exploitable in a vast number of practical applications such as high-porosity materials,[2,3] nanoparticle templating agents, catalytic surfaces, high conductivity nanocomposites,[4] and in dye-sensitized solar cells.[5,6] In fact, it has recently been proposed,[7-10] that the most promising morphologies for the achievement of high-efficiency dye-sensitized solar cells are the so-called ordered bicontinuous phases in which the minority (A) component forms two interweaving networks with cubic periodicity, embedded in a continuous matrix of majority (B) component.[11] Among the ordered bicontinuous phases most commonly observed in some amphiphilic systems[12,13] we have: the gyroid (G) phase, the double diamond (DD) phase, the plumber's nightmare (P) phase, and the Neovius' surface [C(P)] phase. Unfortunately though, the G phase[14,15] is the only bicontinuous phase that is stable in the pure DBC melt, and with a stability region which is relatively narrow compared to other phases like the lamellar (L) or cylindrical (C) phases.[16,17] Not surprisingly then, the G phase has received a good deal of attention in both theoretical and simulation studies for a variety of systems such as: DBC solutions and melts,[18-21] surfactants,[22,23] tethered objects,[24,25] nanocomposites,[26]

* Reproduced with permission from Martinez-Veracoechea, F. J.; Escobedo, F. A. *Macromolecules* **2009,** *In Press*. Copyright 2009 American Chemical Society.

and suspensions of pear-shaped particles.[27] However, other bicontinuous phases remain much less studied, being the most relevant exception the triblock copolymer simulations of Dotera.[28]

In the bicontinuous phases, the general structure of the A-component networks can be described in terms of tubes (connectors) and nodes (junction of several tubes).[29] When the A-B interface, in order to minimize the interfacial energy, tries to approach a constant-mean-curvature surface, the nodes necessarily become bulkier than the tubes.[29] Hence, the chains in the nodes find themselves in an entropically unfavorable situation known as packing frustration in which either: the chains stretch to reach the center of the nodes, a lower concentration region appears in the center of the nodes, the nodes deform, or a combination of all the above scenarios occurs.[20,21,30] The larger the number of connectors per node, the bulkier the nodes become, causing larger packing frustrations.[29] While the G phase has only three connectors per node, the DD and P phases have four and six connectors per node, respectively; thus, explaining the lack of stability of multiple bicontinuous phases in DBC melts. Although in theory the alleviation of packing frustration[30,31] should allow for the stabilization of multiple bicontinuous phases, in practice, it is still unclear how to best accomplish this. Indeed, relevant studies for DBC systems portrayed a rather confusing situation: on the one hand, calculations using Self Consistent Field Theory (SCFT) predicted the stabilization, in a extremely narrow range of the phase diagram, of the DD phase by addition of homopolymer;[32,33] while on the other hand, the P phase is the only bicontinuous phase (i.e., other than G) that has been actually found experimentally, in inorganic-DBC hybrid systems.[34] In a previous work,[35] we used lattice Monte Carlo (MC) to study the stabilization of multiple bicontinuous phases by blending a G-phase forming pure DBC system with selective additives that preferentially "like" the A-block of the DBC chain. When the additive consisted of small selective-solvent

particles, no additional bicontinuous phases were observed; however, when the additive consisted of A-component homopolymer chains, other bicontinuous phases (i.e., the DD and P phases) were observed upon increasing homopolymer concentration. The DD phase was found stable in a surprisingly wide range of homopolymer compositions. In addition, we found a novel "alternating diameter cylinders" (ADC) phase wherein cylinders of two different diameters are arranged in a square packing. A phase similar to the ADC was recently predicted in simulations of a solution of nanoparticles and functionalized block copolymers.[36]

A drawback of particle-based simulations of DBC mesophases is that these phases present long-range periodicity which makes them prone to finite-size effects; as a consequence, at the same thermodynamic conditions multiple phases can be spontaneously obtained depending upon simulation box dimensions and (in some cases) initial conditions.[20,21,28,37,38] Thus, in order to establish the stable morphology at each thermodynamic state, comparison of the molar Helmholtz free among the different observed phases [i.e., at a given temperature (T), density (ρ), and composition] must be made.[21] Efficient calculation of accurate pressures in lattice systems is far from trivial, therefore, in discrete space simulations, a common approach has been to approximate Helmholtz free-energy differences by Gibbs free-energy differences under the assumption that the differences in pressure between phases can be neglected.[35] In order to circumvent this approximation, avoid the inherent problems associated with the discretization of configurational space, and compare with previous results, in this work we present a continuum-space molecular simulation study of the stabilization of the DD and P phases in a blend of DBC and homopolymer in the intermediate segregation regime. For this purpose, we use MC and Molecular Dynamics (MD) with a coarse-grained model of the polymer chains in which each bead is represented by the soft-repulsive potential typical of the

Dissipative Particle Dynamics (DPD) fluid.[39,40] In particle-based molecular simulations the effects of finite chain-length and composition fluctuations are automatically incorporated and the mesophases are spontaneously formed. Since previous SCFT studies[32] suggest that, at the homopolymer concentrations where the DD and P phases are observed in simulations, the stable state could be a two-phase state with a DBC-rich phase and a homopolymer-rich phase, we compare the simulation results with SCFT calculations (which we carried out using the code developed by Morse, Tyler, and coworkers[41]). The SCFT calculations show that, although in many cases macrophase separation can indeed precede the stability of complex bicontinuous phases, the DD phase can be stable in a considerably wide region of parameter space. For the thermodynamic conditions that were explored with SCFT, the P phase was always metastable respect to macrophase separation. However, in many cases the P phase was nearly stable, suggesting that there could exist other unexplored regions of the phase diagram where this phase could be fully stable. Moreover, even in the regions where SCFT shows that either the DD phase or the P phase are metastable with respect to macrophase separation, they are found to lie significantly before the spinodal line, suggesting that at those conditions these two phases could be experimentally observed as "very long lived" metastable phases in which the system would probably get "trapped" once formed. Finally, MD simulations of large systems reveal that the time scales needed for mesophase formation are much shorter than the ones needed for macrophase separation into DBC-rich and homopolymer-rich phases, again suggesting that metastable complex bicontinuous phases could in some cases be experimentally observable.

II. SIMULATION MODEL

We represent polymer chains with a bead-spring model where beads interact with the DPD-fluid potential (U^{DPD}) widely used in DBC studies:[39,40]

$$\frac{U^{DPD}(r)}{kT} = \begin{cases} \frac{a_{ij}(1-r)^2}{2} & if\ r < 1 \\ 0 & if\ r \geq 1 \end{cases} \tag{39}$$

Where r is the inter-bead distance, a_{ij} is the constant that sets the repulsion strength and the indices i,j can be either the A or the B component. Beads of the same type interact with a_{ii}=25, while different-type beads interact with $a_{ij}=a_{ii}+3.27\chi$, where χ is the Flory-Huggins interaction parameter commonly used in DBC systems. The DBC has a chain-length (i.e., number of beads per chain) of N_{DBC}=20 with the first six beads belonging to the A component and the rest to the B component, thus, the fraction of A-component beads in the DBC chains is f=0.30. The homopolymer length is N_{ho}=16 and all its beads belong to the A component.

The beads are connected using a harmonic spring potential (U^{har}),

$$\frac{U^{har}(r)}{kT} = \tfrac{1}{2} k_{sp} r^2 \tag{40}$$

with a spring constant value of k_{sp}=4. Throughout this work χ=2.25 (i.e., χN_{DBC}=45) and the monomer density was always set to ρ_o=3. It is important to note that the G phase was previously found stable at these conditions in the pure DBC melt of this model.[21]

III. SIMULATION METHODS

Simulations were run in the Canonical (nVT) ensemble rather than in the isothermal-isobaric ensemble to avoid the expensive of volumes moves associated with the latter (for large systems) and for consistency with the constant-density SCFT

calculations. After generating a random initial configuration at the desired homopolymer volume fraction (ϕ_h) the system was equilibrated using MD. The equations of motion were integrated using the velocity Verlet algorithm[42] with a time step δt=0.05. Temperature was controlled using the time-reversible momentum-preserving Lowe's thermostat,[43] in which each pair of particles that lie within a cutoff radius (in this work r_{cut}=1) have their relative velocities randomly "thermalized" with probability $\Gamma\delta t$ (=0.05 in this work) at each integration step. We ran simulations for a typical value of 3×10^6 integration steps, although most morphologies were spontaneously formed significantly before (i.e., $< 1\times10^6$ integration steps) the simulations were finished.

As previously mentioned, at a given thermodynamic state more than one morphology can be spontaneously formed. Therefore, the stable phase has to be determined by comparison of the intensive "excess" Helmholtz free energies for each phase and box size. The excess properties are defined by taking as reference an ideal chain with bonded interactions only. The intensive excess Helmholtz free energy can be estimated as:

$$\beta a^{ex} = \beta g^{ex} - (Z-1) \tag{41}$$

where β=1/kT, Z=P/$\rho_{ch}kT$ is the compressibility factor, ρ_{ch} is the polymer chain number density, and g^{ex} is the intensive excess Gibbs energy:

$$\beta g^{ex} = \sum y_i \beta \mu_i^{ex} \tag{42}$$

where y_i is the mole fraction of the i specie (i.e., either DBC or homopolymer) and μ_i^{ex} is its excess chemical potential. The compressibility factor (Z) can be accurately calculated directly from an MD simulation using the Virial Theorem.[42] For this purpose we used a shorter step of δt=0.01, ran simulations 2×10^6 steps long, and estimated the uncertainty in the calculated pressure using standard block analysis.[42] In

order to calculate the Gibbs free energy, however, the MC framework becomes more convenient because one can rigorously use the Expanded Ensemble (EXE) formalism[44,45] and Bennett's acceptance ratio method[46] to efficiently calculate the chemical potentials. Note that either the direct or the configurationally-biased test-particle insertion methods fail to provide reliable chemical potential estimates in the dense systems of polymer chains studied here.[21] In the EXE formalism one gradually inserts/removes a target chain by appending/deleting beads to/from it. The transitions between macrostates m and $m+\Delta$ of the EXE are accepted/rejected with a weighed Metropolis acceptance rule:

$$P_{acc} = \min\{\, 1, \exp(-\upsilon + \psi_{m+\Delta} - \psi_m)\} \tag{43}$$

where $\upsilon = -\Delta \ln W$, $\Delta = +1$ for growth, $\Delta = -1$ for reduction, W is the associated Rosenbluth weight[42] and the ψ's are arbitrary biasing weights chosen to improve sampling. We use the Optimized Ensemble method of Trebst et al.[47] to estimate the biasing weights. This method has been used in chemical potential calculations in DBC systems before and details can be found elsewhere.[21,35,48] Once transitions between macrostates are attempted, the difference in free energy between successive macrostates ($\Delta A_{m,m+1}$) can be efficiently computed using Bennett's acceptance ratio method,[46]

$$\beta \Delta A_{m,m+1} \equiv \ln \frac{Q_m}{Q_{m+1}} = C - \ln \frac{\ell_{m+1,m}}{\ell_{m,m+1}} \tag{44}$$

where Q_m is the canonical partition function associated with the mth macrostate, $\ell_{m,m+1}$ is the number of trial transitions from m to $m+1$, and C is found from:

$$\sum_m \left(1 + \exp\left[\upsilon_{m\to m+1} - C\right]\right)^{-1} = \sum_{m+1} \left(1 + \exp\left[\upsilon_{m+1\to m} + C\right]\right)^{-1} \tag{45}$$

where the summation in the left runs over all the $m \rightarrow m+1$ *attempted* transitions and the summation in the right over all the $m+1 \rightarrow m$ *attempted* transitions. Finally the excess chemical potential for a single species can be obtained from:

$$\beta\mu_i^{ex} = [\beta A_M - \beta A_1] = \sum_{m=1}^{M-1} \beta \Delta A_{m,m+1} \quad (46)$$

with M the number of macrostates, which in this work is the number of beads in a chain plus one (i.e., M_{DBC}=21 and M_{ho}=17) since we inserted/deleted beads one at a time. Five independent MC simulations (previously equilibrated with MD) were run for each system (with a given mesophase) to improve statistics and to estimate the uncertainty in the chemical potential values. Each of these simulations was run for a total of 10^6 MC cycles, each cycle comprising four macrostate transition attempts and N_{tot} relaxation moves (i.e., 5% translations, 5% rotations, 20% reptations, 2% switches (where a chain is repositioned upside-down), 45% hops, and 23% configurational bias moves.) with N_{tot} equal to the total number of monomers in the system. To further accelerate the de-correlation of the samples, every 5×10^4 MC steps, the configurations were evolved using MD during 2×10^4 integrations steps of δt=0.02 (during which no statistics were collected) and then used as input for the following 5×10^4 MC steps.

IV. SELF CONSISTENT FIELD THEORY

In the literature there are numerous studies where SCFT has been successfully applied to the elucidate the phase behavior of DBC systems.[49-51] In addition, homopolymer/DBC blends (though only in the weak segregation regime) have already been studied using SCFT by Matsen.[32] Therefore, here we will only outline the main elements of the theory (further details can be found elsewhere[49-51]). In SCFT the problem of many interacting DBC and homopolymer chains is replaced by the

statistical mechanics of an ideal Gaussian chain in an average position-dependent effective mean-field potential:

$$\begin{aligned} w_A(r) &= \chi N \phi_B(r) + \xi(r) \\ w_B(r) &= \chi N \phi_A(r) + \xi(r) \end{aligned} \tag{47}$$

where $N=N_{DBC}$, and the field $\xi(r)$ is a Lagrange multiplier that allows to enforce the incompressibility constraint:

$$\phi_A(r) + \phi_B(r) = 1 \tag{48}$$

Once the w-fields have been specified, the whole statistical mechanics of the system can be expressed in terms of the chain propagators [$q_{DBC}(r,s)$ and $q_{ho}(r,s)$] for the DBC and the homopolymer, respectively, that satisfy the following differential equation:

$$\frac{\partial q_{DBC}(r,s)}{\partial s} = \frac{b_i^2 N}{6} \nabla^2 q_{DBC}(r,s) - w_i(r) q_{DBC}(r,s) \tag{49}$$

with initial condition $q_{DBC}(r,0)=1$. Here s is a contour variable ($0 \le s \le 1$) and i satisfies:

$$i = \begin{cases} A \ \ if \ \ s < f \\ B \ \ if \ \ s > f \end{cases} \tag{50}$$

and b_i is the statistical segment length of the i component. The homopolymer chain propagator $q_{ho}(r,s)$ satisfies an equation similar to (49) but with i=A, and $s \in [0, \alpha]$, with $\alpha=N_{ho}/N_{DBC}=0.8$.

The local volume fraction of A component is obtained by

$$\phi_A(r) = \frac{(1-\phi)}{Q_{DBC}} \int_0^f ds\, q_{DBC}(r,s) q^c_{DBC}(r,s) + \frac{\phi}{\alpha Q_{ho}} \int_0^\alpha ds\, q_{ho}(r,s) q_{ho}(r, \alpha - s) \tag{51}$$

while ϕ_B is found from:

$$\phi_B(r) = \frac{(1-\phi)}{Q_{DBC}} \int_f^1 ds\, q_{DBC}(r,s) q^c_{DBC}(r,s) \tag{52}$$

with the complementary propagator q^c_{DBC} obtained from an equation similar to (49) but with the right hand side multiplied by -1, and with initial condition $q^c_{DBC}(r,1)=1$. The single DBC-chain partition function Q_{DBC} is defined as:

$$Q_{DBC} \equiv \frac{1}{V}\int_V dr\, q_{DBC}(r,1) \tag{53}$$

with a similar expression for Q_{ho} but with $q_{DBC}(r,1)$ replaced by $q_{ho}(r,\alpha)$. Finally the Helmholtz Free energy can be estimated as:

$$\frac{F\,N}{nkT} = (1-\phi)\left[\ln\left(\frac{1-\phi}{Q_{DBC}}\right)-1\right] + \frac{\phi}{\alpha}\left[\ln\left(\frac{\phi}{Q_{ho}}\right)-1\right] + \frac{1}{V}\int dr\left[\phi_A\phi_B\chi N - \sum_{i=A,B} w_i\phi_i\right] \tag{54}$$

Equations (47) through (53) form a closed set of equations that can be numerically solved self-consistently having as independent variables the *w* fields. In this work these equations were solved using the code developed by Morse, Tyler, and coworkers,[41] in which: the *w* fields are efficiently obtained by expanding them in symmetry-adapted basis functions that can be automatically generated for any space group,[52] eq. (49) is solved using a 4th order operator splitting integration algorithm,[53] and finally, an efficient mechanical-stress calculation provides a convenient algorithm for simultaneously iterating on the unit cell size and the *w* fields.[54] Since this approach requires the symmetry of the desired morphologies to be specified before solving the mean-field equations, it is important to note that the G, DD, and P phases belong to the space groups $Ia\bar{3}d$, $Pn\bar{3}m$, and $Im\bar{3}m$, respectively.

V. RESULTS AND DISCUSSION

Molecular Simulation

Simulations were carried out at χN=45 in a range of homopolymer volume fraction between $0.13 \le \phi_{ho} \le 0.30$. At these conditions four distinct morphologies were spontaneously formed, the phases: P, DD, C and in a few cases, the perforated

lamellar (PL) phase. To the best of our knowledge, this work constitutes the first report that the DD and P phases have been obtained in continuum-space particle-based simulations of DBC systems. The PL phase only formed in very small simulation boxes were none of the other phases could fit a complete unit cell, for this reason we safely disregard the PL as a finite-size artifact. In order to establish which one is the stable phase among the other three phases, at each value of ϕ_{ho}, we calculated βa^{ex} as explained in the section on *Simulation Methods.* Due to the long range periodicity of the morphologies, the calculated values of the free energy were a function of the simulation box size (L_{box}), which demonstrates that the wrong choice of simulation box size can cause a an extra free-energy penalty on a given phase, and therefore, induce the formation of a metastable phase instead of the "true" stable one. As an example, in Figure 4.1, we present a plot of βa^{ex} against L_{box} for the C, DD, and P phases, at ϕ_{ho}=0.30. For each phase βa^{ex} is seen to reach a minimum value, which is then used to determine the stable phase. At these conditions the P phase was found to be stable since it has the lowest value of βa^{ex}. In some cases, to obtain a given phase at several values of L_{box}, we took a spontaneously-formed morphology at the desired value of ϕ_{ho}, compressed/expanded it slightly, removed/added polymer chains to keep ρ_o and ϕ_{ho} constant, and then equilibrated it using MD. However, when the phases were at values of L_{box} far enough from its equilibrium value (i.e., minimum free energy), they often evolved spontaneously to another phase, thus limiting the number of available points for each phase in Figure 4.1. As expected, for a given phase, the value of Z (proportional to the pressure) increases with decreasing L_{box} (Figure 4.2). However, the location of the minimum in the excess Helmholtz energy is a compromise between the behavior of Z and the complex dependence of the excess chemical potentials of the two species. At ϕ_{ho}=0.30 for example, while the DBC $\beta\mu^{ex}$ (Figure 4.3a) follows a non-trivial behavior with box size (often showing a minimum),

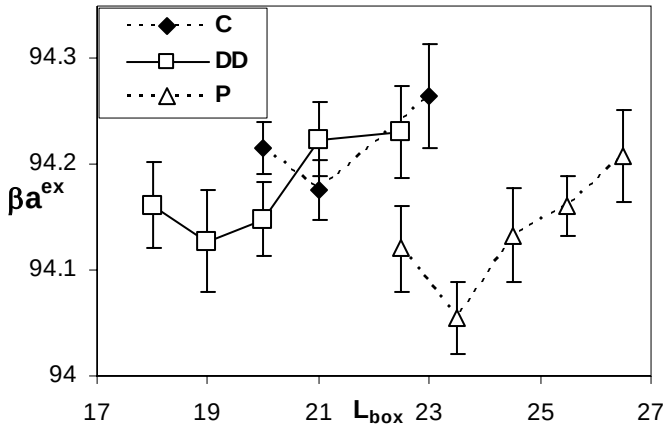

Figure 4.1. Plot of βa^{ex} as a function of the simulation box size, L_{box}, for the C, DD, and P phases, at ϕ_{ho}=0.30. For each phase βa^{ex} is seen to reach a minimum value, which is then used to determine the stable phase.

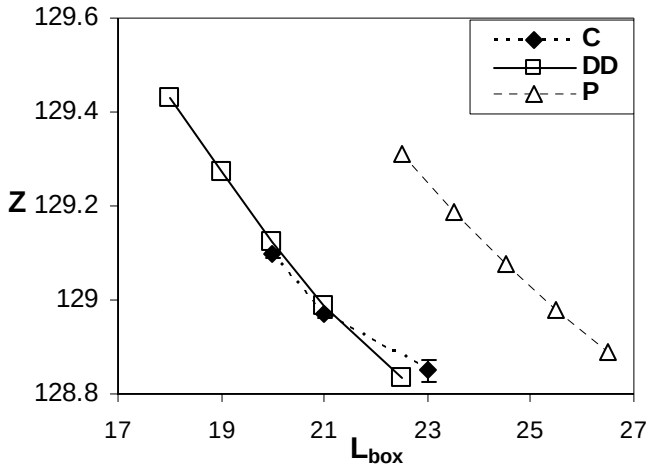

Figure 4.2. Compressibility factor (Z) as a function of L_{box} for different competing phases at ϕ_{ho}=0.30.

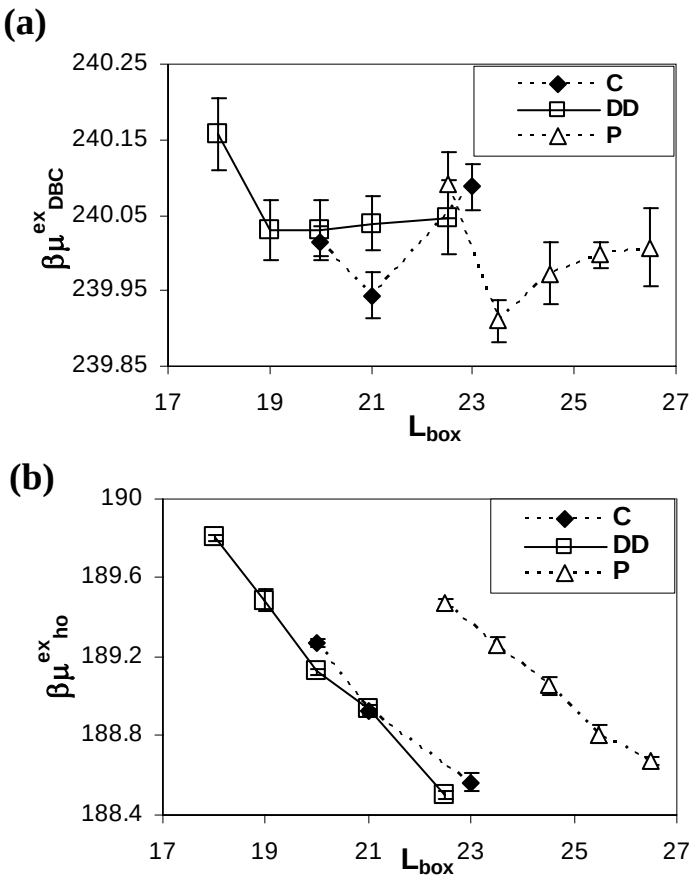

Figure 4.3. Excess chemical potentials $\beta\mu^{ex}$ for the C, DD, and P phases, at ϕ_{ho}=0.30. (a) DBC excess chemical potential. (b) Homopolymer excess chemical potential.

the homopolymer $\beta\mu^{ex}$ (Figure 4.3b) clearly increases with decreasing L_{box}, which is consistent with the idea that a smaller L_{box} implies a stronger confinement of the homopolymer inside smaller A-domain regions, reducing its configurational entropy and hence rising its chemical potential (a similar behavior is observed for all the values of ϕ_{ho}).

One shortcoming of the free energy analysis presented above is that the simulations were performed in relatively small systems, with only one unit cell for the DD and P phases and with just a few unit cells for the C phase, therefore, finite-size effects can be important (in Figs. 4.1-4.3 the total number of "mers" per box can be found from $\#mers = \rho_0 L_{box}^3$). In an attempt to assess these effects in each phase while keeping the systems computationally tractable, we took the already equilibrated systems at the sizes where the free energy is a minimum and doubled them in size (i.e., doubling only one dimension), then equilibrated them using MD and calculated their free energy in the same way as for the "smaller" systems but with MC simulations that were run by a total of 2×10^6 cycles. While the initial morphology was usually preserved, in some cases it either developed some defects or was destroyed. When this happened, we took the equilibrated systems with sizes that were "neighboring" the free energy minimum, doubled them, and calculated the free energy. Interestingly smaller size systems (i.e., to the left of the minimum) tended to get destroyed more often when doubled in size than larger systems (i.e., to the right of the minimum) suggesting that some of these small-box structures were being artificially stabilized by finite-size effects.

After doing a similar free energy analysis for the simulations obtained at different values of ϕ_{ho}, we obtained the approximate phase diagram shown in Figure 4.4a, where we have delineated tentative phase boundaries in order to indicate the regions of stability of each phase. In Figure 4.4b we plot the difference in excess

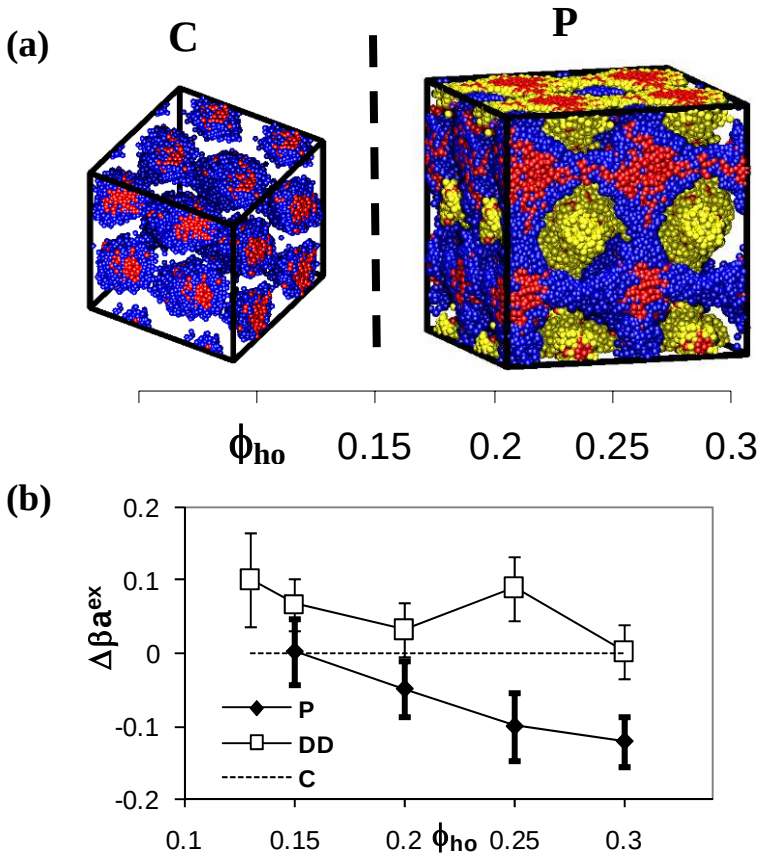

Figure 4.4. (a) Approximate phase diagram obtained with the particle-based simulations as a function of ϕ_{ho} for χN=45. The regions of stability of each phase are roughly delineated based on free energy calculations. Snapshots of the C and P phases are shown wherein the B-component has been omitted for clarity. In the C phase the A-blocks are shown in blue. In the P phase the A-blocks are either shown in blue or yellow depending upon which minority-component network they belong to. The homopolymer is shown in red. (b) Helmholtz free energy difference ($\Delta\beta a^{ex}$) of the distinct phases with respect to the C phase. The DD phase was never found to have the lowest free energy at the discrete values of ϕ_{ho} studied. The C-P phase transition is located around ϕ_{ho}~0.15.

Helmholtz free energy between the different morphologies and the C phase at the different values of ϕ_{ho} (i.e., $\Delta\beta a^{ex} \equiv \beta a^{ex}_i - \beta a^{ex}_C$, with i=P, DD, or C). The free energies employed in this plot were estimated from the double-size systems previously mentioned. For clarity we show the (dashed) curve $\Delta\beta a^{ex}=0$, indicating the excess free energy of the C phase. Interestingly, the DD phase never has the lowest free energy despite spontaneously forming in the simulations, while the P phase is the stable phase over most of the composition range studied. However, at $\phi_{ho}=0.15$ the free energy of the P phase is (within error bars) essentially equal to the free energy of the C phase. Since packing frustration will destabilize the P phase at lower homopolymer volume fractions, and the P phase was not spontaneously formed in the simulations at $\phi_{ho}=0.13$, we conclude that the C-P phase boundary is located around $\phi_{ho}\sim0.15$. Finally, we expect the existence of a G-C phase transition at even lower values of ϕ_{ho} (i.e., outside the composition range studied), since the G phase has been shown to be stable in the pure melt of this model system (i.e., $\phi_{ho}=0$).[21] In summary then, the simulation model is consistent with the sequence G→C→P as ϕ_{ho} increases.

Comparison with SCFT

Molecular simulations present the advantage that the morphologies form spontaneously when started from random configurations, thus little previous information about the symmetry of the morphologies is often needed. However, accurate calculation of the free energy of each phase is computationally demanding, and, no automatic and robust method for determining the appropriate unit cell dimensions of each phase is available to date. Moreover, molecular simulation cannot satisfactorily assess macrophase separation in DBC systems due to the large simulation sizes and long time scales involved. For this reason, once a set of plausible morphologies has been obtained from simulation, it proves convenient to use SCFT

for exploring, in a faster, broader, and more detailed fashion, the phase diagram of the DBC/homopolymer blend.

We explored the phase diagram using SCFT in a range of homopolymer composition between $0 \leq \phi_{ho} \leq 0.40$ and segregation $25 \leq \chi N \leq 35$. In this range of segregation (i.e., intermediate segregation regime) the observed morphologies are less likely to be destroyed by fluctuation effects as has been shown to occur in the weakly segregated region of the phase diagram.[55, 56] Note that while the simulations were performed at a higher value of segregation (i.e., χN=45), such a high value of χN becomes computationally prohibitive for the solution of the SCFT equations given the large number of basis function needed for an accurate enough description. However, we expect that the phase behavior predicted by SCFT at χN=45 should be similar to that observed at χN ~35. This expectation is supported by the weak dependence of the phase boundaries' location on χN (see discussion below), once a high-enough segregation has been reached (i.e., $\chi N \geq 30$).

Exact correspondence between simulation results and SCFT is not possible. In the simulations, only certain values of f are accessible due to the discretization caused by the finite number of beads (e.g., N_{DBC}=20). In addition, finite chain-length effects, fluctuations, and differences in the underlying model, will cause differences in the observed phase diagrams. However, it is expected that the general features of the phase diagram (e.g., sequence of stable phases, etc.) will remain qualitatively the same. While in the particle-based simulations the G phase is stable at f=0.30 for the pure system,[21] this is not the case for the Gaussian chains used in SCFT.[17] For this reason, we calculated phase diagrams using SCFT for several values of f, which roughly comprise the region of parameter space for which the G phase is found stable in the pure system for $25 \leq \chi N \leq 35$. The different values studied were f=(0.315, 0.320, 0.325, 0.330), with the first two being close to the transition between the C and G

phases in the pure system, a region of the phase diagram analogous to where the computer simulations were carried out.

In Figure 4.5a we show the predicted phase diagram in a χN vs. ϕ_{ho} plot for f=0.315. The C phase is the only morphology found stable at these conditions. The system macrophase separates in DBC-rich C phase and in a homogenous homopolymer-rich (HoR) phase, though the G phase is expected to be stable in the pure system for $\chi N > 41$. The HoR phase was found to be essentially pure homopolymer (i.e., $\phi_{ho} > 0.99999$) in the range of parameters studied (including the different values of f). In Figure 4.5b we present the regions of the phase diagram where distinct phases have the lowest Helmholtz free energy, i.e., what the phase diagram would be if macrophase separation were disallowed. This type of plot allows for comparison with molecular simulation results where the relatively small simulations boxes used would preclude macrophase separation. Figure 4.5b shows that the addition of homopolymer reduces the free energy of the DD and P phases with respect to the other phases. However, for f=0.315 the region of "metastability" of the DD phase is very narrow. In fact for low χN (i.e., < 28.87), the DD has no longer a region of lowest free energy. Figure 4.5b also shows, in dashed-line, the boundary where macrophase separation occurs. It is interesting to note that even though the phases to the "right" of the dashed-line are metastable respect to macrophase separation, they are outside their own spinodal curve (not shown), given by the condition:

$$\frac{\partial^2 F}{\partial \phi_{ho}^{\ 2}} = 0 \tag{55}$$

which suggests that the system could remain trapped in one of these metastable phases as a single-phase long-lived metastable state before macrophase separating. The ADC

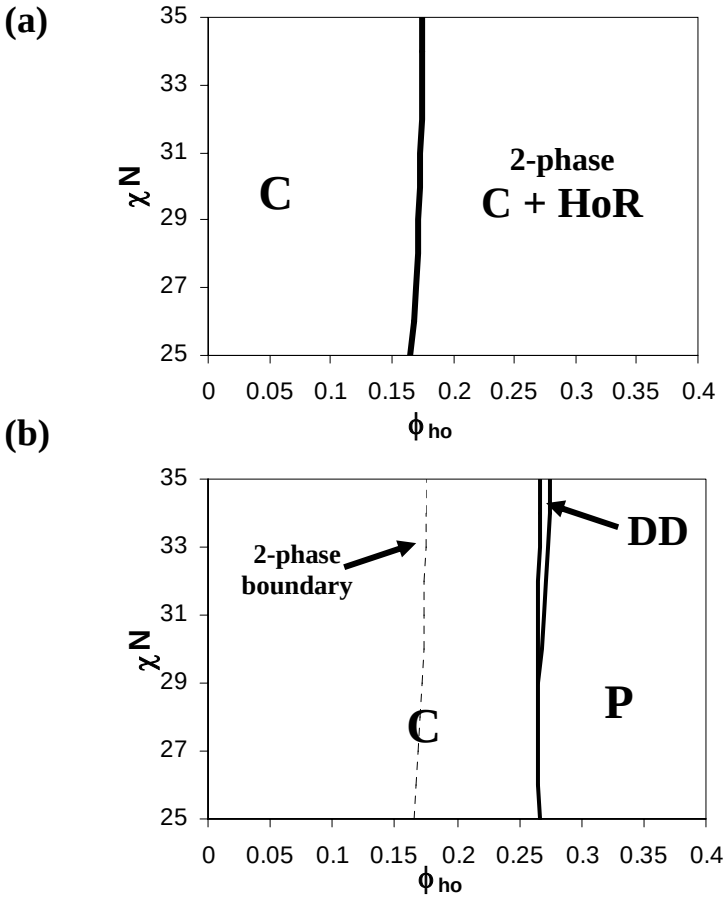

Figure 4.5. Plot of the SCFT predictions in a χN vs. ϕ_{ho} diagram for f=0.315. (a) Stable phase diagram. The C phase is the only stable morphology at the conditions studied. At enough homopolymer concentration the system presents macrophase equilibrium between the C phase and an almost-pure homopolymer-rich (HoR) phase. (b) Regions of phase diagram where the different competing phases have the lowest free energy. The macrophase separation coexistence line is shown (dashed). The DD and P phases are metastable respect to macrophase separation. The region of metastability of the DD phase is quite narrow.

phase was found to always have higher free energy than the other phases (this was also true for all the values of f studied).

Figure 4.6a shows the calculated phase diagram in a χN vs. ϕ_{ho} plot for f=0.32. The region of stability of the G and C phases is separated by a narrow region were they both coexist. At $\chi N > 30.2$ the G phase is stable in the pure system, and remains stable for low homopolymer concentrations. Further addition of homopolymer eventually destabilizes the G phase, and the C phase becomes stable. For $\chi N < 30.2$, the C phase is stable in the pure system, however, a transition of the form C→G→C is observed for a finite range of χN that culminates in a azeotropic point around $\chi N \approx 27.3$ and $\phi_{ho} \approx 0.03$. This is remarkable, since it shows that addition of small amounts of homopolymer (i.e., $\phi_{ho} \sim 0.03$) can stabilize the G phase in areas of the phase diagram where the C phase is the stable one in the pure system. This is consistent with the idea that the reason for the limited stability of the bicontinuous phases in the DBC melt is packing frustration inside the nodes, and that addition of small amounts of homopolymer can relieve this frustration in the G phase. For higher values of $\phi_{ho,}$ nonetheless, the C phase becomes stable until the point where macrophase separation occurs, wherein the C phase coexists with a HoR phase. Similarly, Figure 4.6b shows the phase diagram regions where the distinct phases have the lowest Helmholtz free energy and (in dashed-line) the boundary where macrophase separation occurs. To the right of the dashed-line we observe the DD and P phases, with the DD phase occupying a larger region of phase diagram than with f=0.315. Although the DD and P phases are metastable respect to macrophase separation, they could be "long-lived" since their regions of lowest free energy (as a single phase) are outside their spinodal curves. Figure 4.6b shows how in a system where macrophase separation is prevented (e.g., in simulation of small systems) one could observe a progression of phases with addition of homopolymer like: G→C→DD→P. In a previous work,[35] we performed

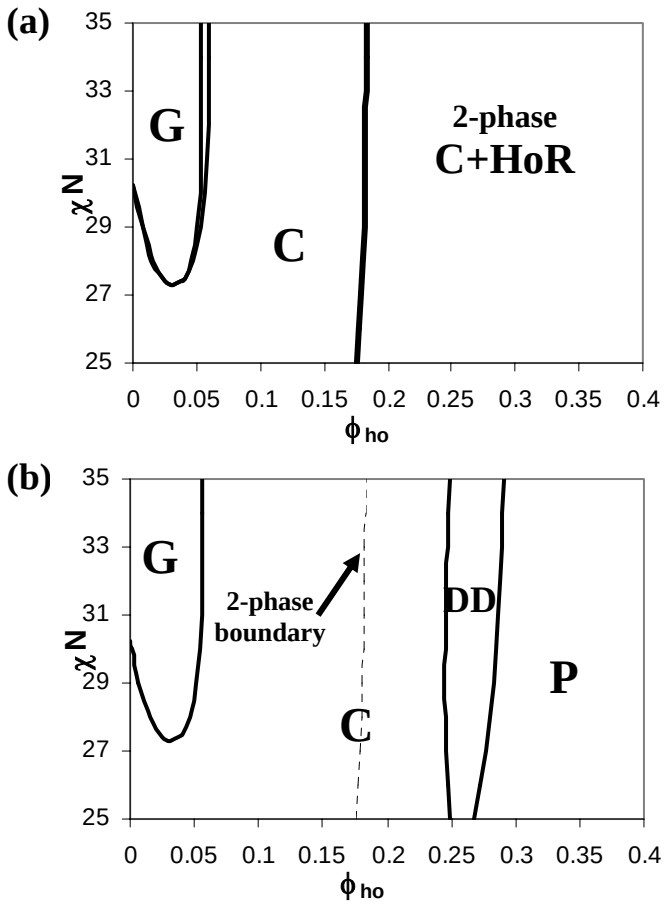

Figure 4.6. χN vs. ϕ_{ho} diagram calculated with SCFT for f=0.32. (a) Stable phase diagram. The G phase is initially stabilized by small amounts of homopolymer but further addition produces a transition towards the C phase. At high homopolymer concentration the system presents macrophase equilibrium between the C phase and the HoR phase. (b) Regions of phase diagram where the different competing phases have the lowest free energy. The macrophase separation coexistence line (dashed) indicates that the DD and P phases are metastable respect to macrophase separation. The region of metastability of the DD phase increases respect to the f=0.315 case.

lattice simulations of DBC/homopolymer blends where we observed precisely such a progression. Although in that work we found that there was a significant region where the C phase had lower free energy than the G and DD phases, we erroneously assumed that the C phase was just metastable (due to the lack of any precedence for a G-to-C transition induced by addition of selective additive). However, the SCFT calculations together with the previous free energy calculations amount to enough evidence to conclude that the C phase is the true stable phase in the region of phase diagram in between the G and DD phases.

In Figure 4.7a we show the calculated phase diagram in a χN vs. ϕ_{ho} plot for f=0.325. The observed phase behavior is qualitatively similar to the f=0.32 case, but with an enlarged region of stability for the G phase, since now the G phase is stable in the pure system for $\chi N > 25.5$. Addition of enough homopolymer (i.e., $\phi_{ho} \sim 0.08$) destabilizes the G phase in favor of the C phase. In Figure 4.7b we show the regions where each phase has the lowest free energy together with the macrophase separation coexistence line (dashed). The free energies of the DD and P phases are seen to be lowered by addition of homopolymer due to reduction in the packing frustration, but not enough to become stable phases. The region where the DD phase is metastable is considerably larger now than for smaller values of f, and the region where the DD phase has the lowest free energy is closer to the two-phase coexistence curve.

Figure 4.8a presents the calculated phase diagram for f=0.33. The observed phase behavior is significantly complex, with the more distinguishing feature being that the DD phase is now the most stable state in a significant region of phase diagram which should be wide enough, both in χN and ϕ_{ho}, to be attainable experimentally. Thus, this work constitutes an extension of the previous work of Matsen[32] where the DD phase was found stable only in a very narrow region of the phase diagram. It is important to note that to date the DD phase has never been observed experimentally in

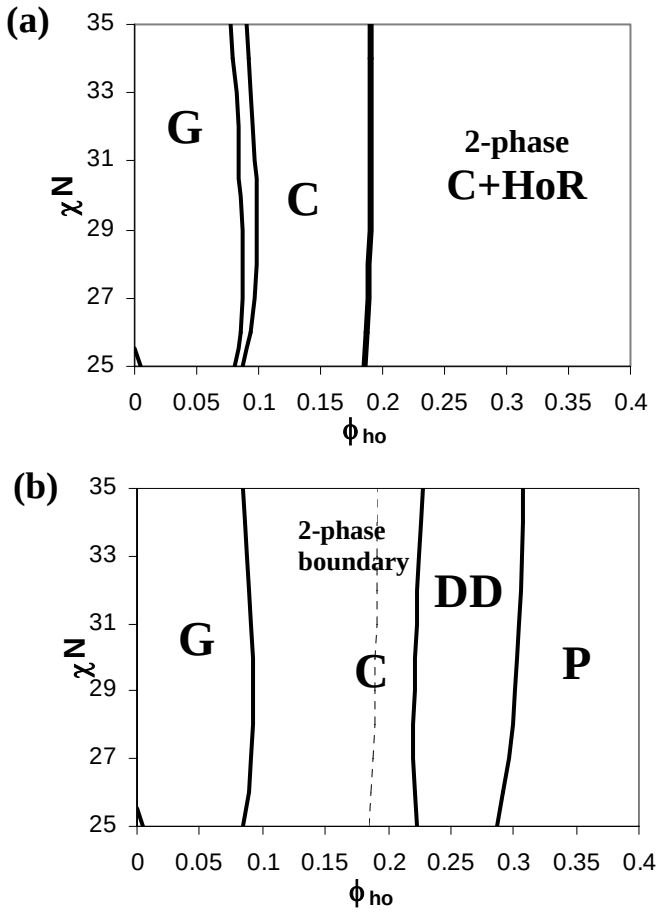

Figure 4.7. SCFT diagram of χN vs. ϕ_{ho} for f=0.325. (a) Phase diagram. The G phase is stable in a significant region of phase diagram for low homopolymer content, but the C phase becomes stable moderate homopolymer content. Further increase in ϕ_{ho} eventually leads to the coexistence of the C phase and the HoR phase. (b) Regions of phase diagram where the different competing phases have the lowest free energy. The macrophase separation coexistence line is also shown (dashed). The DD and P phases are metastable respect to macrophase separation; however, the region of metastabiltiy of the DD phase is near the coexistence line.

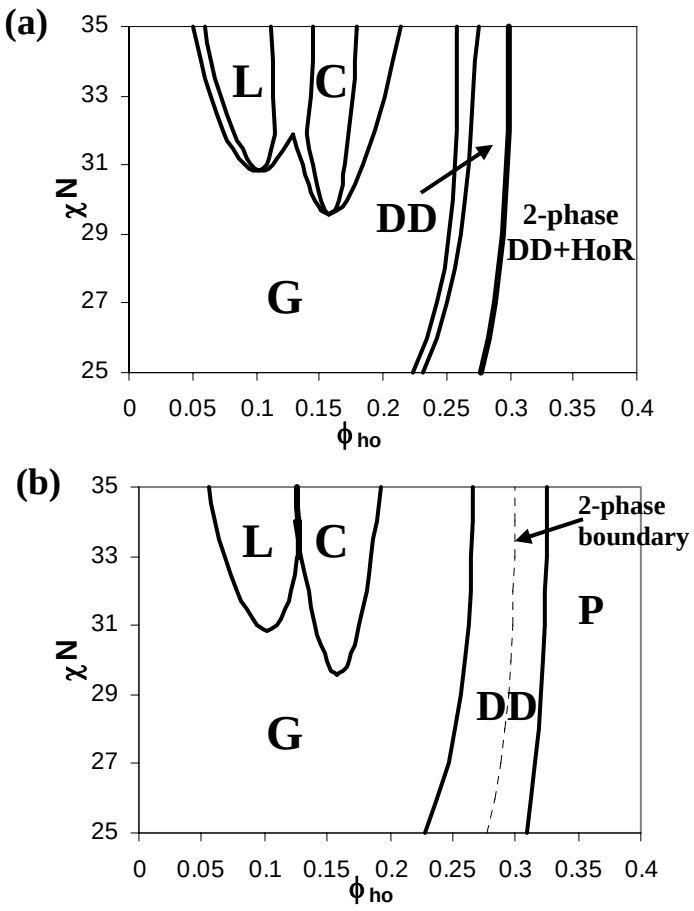

Figure 4.8. χN vs. ϕ_{ho} diagram of the SCFT calculations for f=0.33. (a) Phase diagram. The DD phase is stable in a significant region of phase diagram. A triple point where the L, G, and C phases coexist is observed. A complex progression of phases with addition of homopolymer can be observed, including the remarkable sequence G→L→G→C→G→DD for χN~31.5. Further increase in ϕ_{ho} eventually causes the coexistence of the DD phase and the HoR phase. (b) Regions of phase diagram where the different competing phases have the lowest free energy. The macrophase separation coexistence line is also shown (dashed). The P phase is still metastable respect to macrophase separation.

melts of DBC systems;[14, 57, 58] we hope that the present results will contribute to change this situation.

Figure 4.8a also shows how the L phase starts to be stabilized with increasing χN, reflecting the fact that we are approaching the f and χN values where the G-L phase boundary occurs in the pure system.[59] In the same way, the C phase region becomes much smaller which is consistent with the fact that the C phase is losing stability because of the increasingly longer minority-component block. In between the single-phase regions there are, as expected, regions of coexistence; in particular, there is a triple-point around χN= 31.885 where the L, G, and C phases coexist having homopolymer volume fractions (ϕ_{ho}) of 0.114, 0.130, and 0.140, respectively. In addition, the coexistence regions between the L and G phases, and between the G and C phases, end in azeotropic points when lowering χN. The very wide range of ϕ_{ho} for which the G phase is stable at low χN is a consequence of the fact that at these conditions the G phase is at the very core of its region of stability in the pure system. For values of χN in between the L-G azeotropic point (i.e., χN~30.85) and the triple-point (i.e., χN~31.885) the remarkable sequence of stable phases G→L→G→C→G→DD can be observed upon increasing homopolymer content, which gives an idea of the complex interplay of the different factors (i.e., energetic and entropic) that determine the free energy of each one of the competing phases in the system. However, it is likely that thermal fluctuations, will have an important effect in the actual sequence of phases that can be experimentally observed.[60] Finally, if the homopolymer content of the DD phase is further increased, the system macrophase separates into a DBC-rich DD phase and a HoR phase. In Figure 4.8b we show the regions where each phase has the lowest free energy together with the macrophase separation coexistence line (dashed). It can be observed that close to the region where the system reaches the maximum of homopolymer solubility (i.e.,

coexistence line), the P phase exists as a metastable state (again outside the spinodal curve). Given the proximity of these regions, it seems quite feasible to reach a high-enough degree of "over-saturation" in homopolymer content to make the P phase experimentally observable. Moreover, this very proximity of the P phase to the stable region strongly suggests that there could be different combinations of χN, f, and α where the P phase becomes fully stable in DBC/homopolymer blends. Finding such region, however, will be the subject of future work. Also, near the high homopolymer-concentration region where the P phase is metastable, other complex bicontinuous phases [e.g., C(P), I-WP, etc.][12] could have a region of metastability; these phases, however, would have unit cells much larger than our current computational capabilities allow and therefore are outside the scope of the present work.

In the present study we have lowered the free energy of the DD and P phases by addition of minority-component homopolymer 2.67 times longer than the minority block (c.f., α=0.80 and f=0.30). At these conditions, the homopolymer is not expected to penetrate into the A-block-rich region (dry brush regime[1]), hence inducing either the formation of phases of *more* interfacial curvature like the DD and P phases,[35] or macrophase separation. Conversely, when the size of the homopolymer is comparable or smaller than the affine block (in this case the A-block), the homopolymer swells the affine block (wet brush regime[1]), inducing phases of *less* interfacial curvature (e.g., L, reverse G, reverse C, etc.), and therefore precluding the formation of the P and DD phases.[35, 61] This is consistent with the experimental work of Mareau et al.[62] where addition of homopolymer of a size corresponding to the wet brush regime, induced the formation of the (reverse) G and C phases, but not the DD or P phases, at conditions wherein the pure DBC melt formed the L phase.

The fact that two totally different approaches, namely, continuum space particle-based simulations and SCFT, predict the DD and P phases having a lower free

energy than any other *single* phase at high homopolymer content, suggests that this kind of behavior is very general and should apply to many different real DBC/homopolymer systems. This idea is reinforced when considering that these phases were also observed using lattice MC techniques.[35]

Our simulations using the DPD fluid found that, for the discrete values of ϕ_{ho} studied, the DD phase had always higher free energy than the C and P phases. This is qualitatively what would be observed in SCFT calculations if the "effective" value of the simulation f were in between $0.315 < f < 0.320$, since at these conditions the G phase starts to be stable in the pure system for high χN and the DD phase has the lowest free energy in a very narrow region that could have been easily "skipped" by our choice of discrete ϕ_{ho} values. Interestingly, the previous lattice simulations[35] do present a region where the DD phase has the lowest free energy, suggesting that the for the lattice system the effective value of f is somewhat higher (i.e., $0.32 < f < 0.325$). However, it is important to remember that quantitative comparison between the different approaches is not possible, not only because of the very different nature of the underlying models, but also because of the different values of χN employed in each one of the approaches. Because of these reasons, refining the simulation grid to investigate whether the phase diagrams obtained from the different approaches further agree could prove unproductive.

Although we cannot directly measure in the DPD-fluid simulations the concentration at which the system phase-separates, SCFT calculations for $f < 0.325$, suggest that the regions where our simulations find the DD and P phases with the lowest free energy are metastable with respect to macrophase separation in DBC-rich and HoR phases. However, the same SCFT calculations also show that, at these high values of χN, these phases are not unstable and could therefore be long-lived metastable states. Thus, whether or not the DD and P phase can be observed

experimentally for $f < 0.325$ is going to depend upon the kinetics of mesophase formation and macrophase separation. Though making such a kinetic study lies outside of the scope of the present work, we used MD simulations to get an order-of-magnitude estimate of the difference between the time scales needed for mesophase formation and for macrophase separation. Since macrophase separation can be inhibited due to the free energy penalty incurred to create an interface in a relatively small simulation box,[42] we set one dimension much longer than the other two to induce the formation of the interface perpendicular to the long direction and allow for two well-defined bulk phases.[63] Accordingly, the simulation box had dimensions of 22×22×150 DPD units, and the initial configuration was a random mixture of the DBC and homopolymer at the desired volume fraction (i.e., ϕ_{ho}=0.30), which is expected to be in the metastable region of phase diagram. The system was then evolved using MD for a long simulation time (i.e., 1×10^7 steps of δt=0.05). Though a mesophase was readily observed, no signs of macrophase separation were ever found. For this reason, we decided to induce the macrophase separation by "seeding" a homopolymer-rich nucleus. To create such an initial configuration, a significant portion (i.e., 20%) of the box was filled up with pure homopolymer, while the remainder of the box was filled with a DBC/homopolymer blend of the desired homopolymer volume fraction (i.e., ϕ_{ho}=0.30). The system was evolved again using MD for a long simulation time (i.e., 2×10^7 steps of δt=0.05). Interestingly, while the DBC/homopolymer section of the simulation box rapidly (i.e., before 5×10^5 steps) segregated into A-rich and B-rich domains, no significant diffusion of homopolymer between the two phases was observed. Moreover, the DBC/homopolymer blend initially arranged (< 2×10^6 steps) into two different sections in which the DD phase and the ADC phase were identified (Figure 4.9a). Afterwards, the DD phase section started to grow at the expense of the ADC phase, until after ~3.5×10^6 simulation steps, when the DBC/homopolymer blend

was arranged entirely in the DD phase (Figure 4.9b). Nonetheless, during the whole simulation run (i.e., 2×10^7 steps) no homopolymer was able to go from the DBC/homopolymer section to the homopolymer rich phase, indicating that the kinetics of phase separation is at least (but probably more than) one order of magnitude slower than that of mesophase formation. To understand this difference in time scales, the structure of the interface is examined in the concentration profile shown in Figure 4.9c, where it can be seen that even after a homopolymer-rich nucleus has been formed, the homopolymer molecules would need to diffuse across a nearly-pure B-component region to reach the HoR phase, and therefore incur in a very high energetic penalty. Thus, the interface literally acts as an impermeable barrier that frustrates the macrophase separation process by preventing direct diffusion of the homopolymer chains. The origin of the B-rich domain close to the interface is easily understood when considering that the DBC chains in the vicinity of the HoR nucleus have to position their A-blocks so that they are in contact with the HoR phase, thus effectively "coating" the whole homopolymer-rich nucleus with DBC B blocks. This being the case, macrophase separation needs to rely on other mechanisms to transport the homopolymer chains such as interfacial defect-formation and large density fluctuations. However, it is likely that given the highly-dense systems studied here, such events are too rare to be observed directly in simulations (in the absence of external forces like shearing action). On the other hand, mesophase formation only involves local rearrangement of DBC and homopolymer chains, a process that is significantly faster. It is possible that for real systems where the interfacial area is much larger than that of the simulated systems, interfacial defects may occur that would accelerate the process of macrophase separation. However, in our simulations

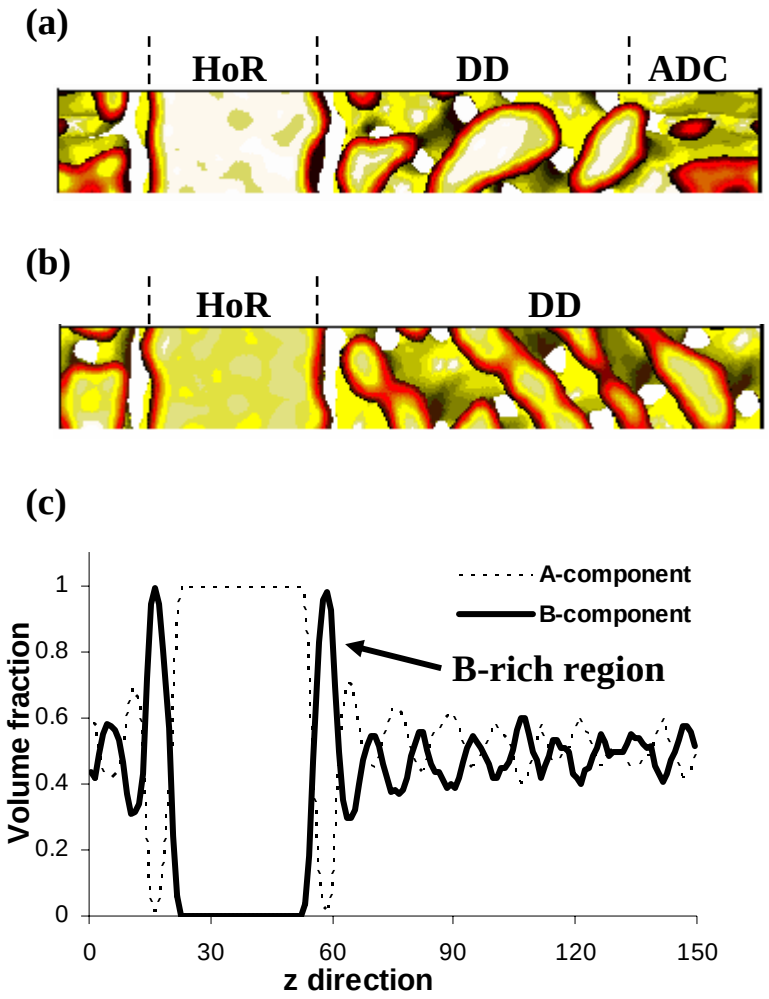

Figure 4.9. MD simulation in a box with dimensions of 22×22×150 DPD units. The initial configuration was seeded with a homopolymer-rich nucleus while the remainder of the box was filled with a DBC/homopolymer blend of ϕ_{ho}=0.30. (a) Snapshot after 2×10^6 integration steps. Two different regions, one with the DD phase, and one with the ADC phase can be observed. Only the A-component is shown. (b) Snapshot after 3.5×10^6 integration steps where the DD phase has taken over the whole system. (c) Concentration profile of the previous snapshot; close to the interface there is a region of almost pure B-component which prevents the diffusion of the homopolymer chains across the interface.

we never observed the formation of such defects; not even when the cross-section of the simulation box was made as large as 40×40 DPD units. This result suggests that, even if the stable state is macrophase separation, if a sample is prepared from a homogenous, quiescent state where the DBC and homopolymer chains are well mixed, the system will tend to form a mesophase prior to macrophase separation and could perhaps remain trapped in this state for time scales long enough for experimental measurement.

VI. CONCLUSIONS

We have shown how a combination of particle-based simulations and SCFT can be used to gain a better understanding of the complex phase behavior of DBC/homopolymer blends. In the continuum-space particle-based simulations the ordered bicontinuous DD and P phases were spontaneously formed without previous information about their symmetry. To the best of our knowledge this is the first time that these two phases have been obtained in continuum-space molecular simulations of DBC systems. Additionally, the simulated phases in the present work are consistent with those of a previous simulation work of DBCs in discrete space.[35] However, particle-based simulations posses the disadvantage that free energy calculations are expensive and that phase separation is difficult to deal with. Conversely, calculations of free energy and phase equilibrium are straightforward in SCFT but this requires information about the symmetries of the candidate phases. Thus, once simulations provided an idea of the possible phase behavior we proceeded to use SCFT to analyze the DBC/homopolymer phase diagram in more detail. The SCFT calculations showed that, although in many cases macrophase separation can indeed precede the stability of complex bicontinuous phases, the DD phase can be stable in a considerably wide region of the phase diagram around f~0.33 and ϕ_{ho}~0.26. We hope that the present

work will prompt experimental efforts to try to confirm the formation of the DD phase in DBC systems. SCFT also showed how a small amount of homopolymer can stabilize the G phase in regions of the phase diagram where it is not stable in the pure system, while a further increase in ϕ_{ho} can actually stabilize the C phase. For the thermodynamic conditions that were explored with SCFT, the P phase was always metastable respect to macrophase separation. However, the proximity of the P-phase metastability region to the two-phase (i.e., DBC-rich and HoR) coexistence line suggests that there could be other regions of parameter space where the P phase is fully stable. Moreover, even when the DD and P phases are only metastable, MD simulations suggests that the kinetics of mesophase formation is at least one order of magnitude faster than the kinetics of macrophase separation indicating that these phases might be able to be observed experimentally as "long-lived" metastable states.

Finally, we showed that the problem of stabilizing multiple bicontinuous phases was equivalent to the problem of overcoming packing frustration while avoiding macrophase separation. In the present work we attempted to perform this stabilization using a linear homopolymer with a chain-length α=0.8×N_{DBC}. Though this size and architecture of the selective additive accomplished many of the desired objectives, it is not necessarily optimal. In a future work we will study the effect that alternative features of the selective additive have in the stabilization of multiple ordered bicontinuous phases.

NOTE ADDED

The P phase was recently found to be fully stable in a finite region of the phase diagram when the selective additive was composed of four-arm star-homopolymers (instead of linear) because of the increased solubility that the star-homopolymers have in the DBC-rich phase due to their more compact structure. These results are

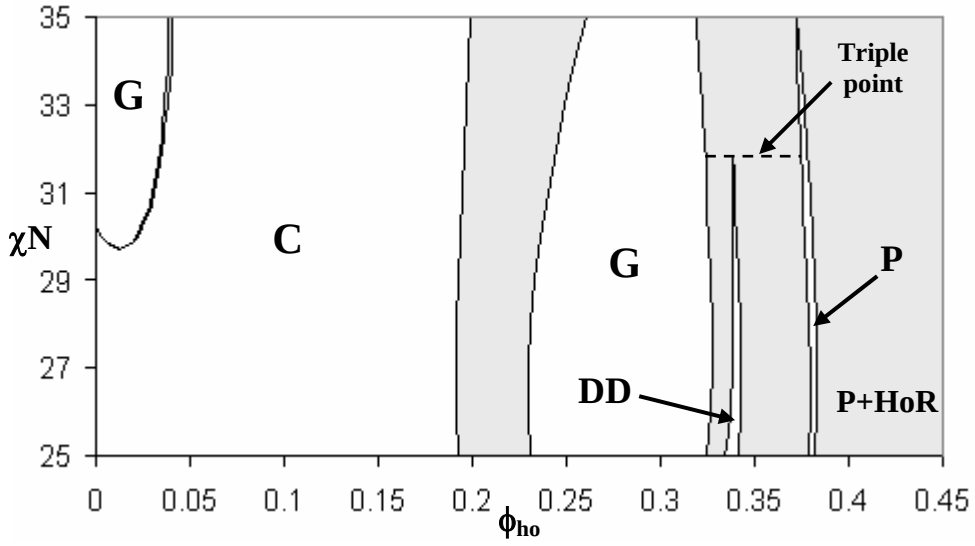

Figure 4.10. χN vs. ϕ_{ho} diagram of the SCFT calculations for f=0.32 in a blend between a DBC and a star-homopolymer of total length α=0.80. The P phase is fully stable. Blank areas are single-phase regions, while shaded areas represent two-phase coexistence regions.

summarized in Figure 4.10 where the DBC/star-homopolymer phase diagram is shown for a value of f=0.32. The total length of the star-homopolymer is still α=0.80 (i.e., each arm α_{arm}=0.20). The DD and P phases are fully stable.

Finally, conformational asymmetry between the two blocks, as is likely to exist in real systems, was found (results not shown) to also stabilize the P phase in blends of DBC/linear-homopolymer. In particular, for a blend of PI-b-PS and PI (linear) homopolymer, SCFT predicted a narrow region of stability for the P phase.

ACKNOWLEDGMENTS

We are very grateful to Prof. David Morse and his student Jian Qin for providing the code and generous guidance to implement the SCFT calculations. We are also grateful to Prof. U. Wiesner for helpful discussions. The financial support by NSF (Grant 0756248) and by the Cornell-KAUST center is gratefully acknowledged.

REFERENCES

1. Hamley, I. W., *The Physics of Block Copolymers*. Oxford University Press: **1998.**

2. Uehara, H.; Yoshida, T.; Kakiage, M.; Yamanobe, T.; Komoto, T.; Nomura, K.; Nakajima, K.; Matsuda, M. *Macromolecules* **2006,** 39, (12), 3971-3974.

3. Kamperman, M.; Garcia, C. B. W.; Du, P.; Ow, H. S.; Wiesner, U. *J. Am. Chem. Soc.* **2004,** 126, (45), 14708-14709.

4. Cho, B. K.; Jain, A.; Gruner, S. M.; Wiesner, U. *Science* **2004,** 305, (5690), 1598-1601.

5. Sun, S. S. *Sol. Energy Mater.* **2003,** 79, (2), 257-264.

6. Watkins, P. K.; Walker, A. B.; Verschoor, G. L. B. *Nano Lett.* **2005,** 5, (9), 1814-1818.

7. Crossland, E. J. W.; Nedelcu, M.; Ducati, C.; Ludwigs, S.; Hillmyer, M. A.; Steiner, U.; Snaith, H. J. **2008**, 10.1021/nl800942c

8. Wang, H.; Oey, C. C.; Djurisic, A. B.; Xie, M. H.; Leung, Y. H.; Man, K. K. Y.; Chan, W. K.; Pandey, A.; Nunzi, J. M.; Chui, P. C. *Appl. Phys. Lett.* **2005,** 87, (2).

9. Oey, C. C.; Djurisic, A. B.; Wang, H.; Man, K. K. Y.; Chan, W. K.; Xie, M. H.; Leung, Y. H.; Pandey, A.; Nunzi, J. M.; Chui, P. C. *Nanotechnology* **2006,** 17, (3), 706-713.

10. Crossland, E. J. W.; Kamperman, M.; Nedelcu, M.; Ducati, C.; Wiesner, U.; Smilgies, D. M.; Toombes, G. E. S.; Hillmyer, M.; Ludwigs, S.; Steiner, U.; Snaith, H. *Nano Lett.*, Article ASAP. DOI: 10.1021/nl803174p.

11. Andersson, S.; Hyde, S. T.; Larsson, K.; Lidin, S. *Chem. Rev.* **1988,** 88, (1), 221-242.

12. Strom, P.; Anderson, D. M. *Langmuir* **1992,** 8, (2), 691-709.

13. Schwarz, U. S.; Gompper, G. *J. Chem. Phys.* **2000,** 112, (8), 3792-3802.

14. Hajduk, D. A.; Harper, P. E.; Gruner, S. M.; Honeker, C. C.; Kim, G.; Thomas, E. L.; Fetters, L. J. *Macromolecules* **1994,** 27, (15), 4063-4075.

15. Schick, M. *Physica A (Amsterdam)* **1998,** 251, (1-2), 1-11.

16. Matsen, M. W.; Schick, M. *Phys. Rev. Lett.* **1994,** 72, (16), 2660-2663.

17. Matsen, M. W.; Bates, F. S. *J. Chem. Phys.* **1997,** 106, (6), 2436-2448.

18. Yu, B.; Li, B. H.; Sun, P. C.; Chen, T. H.; Jin, Q. H.; Ding, D. T.; Shi, A. C. *J. Chem. Phys.* **2005,** 123, (23), 234902.

19. Rychkov, I. *Macromol. Theory Simul.* **2005,** 14, (4), 207-242.

20. Martinez-Veracoechea, F. J.; Escobedo, F. A. *Macromolecules* **2005,** 38, (20), 8522-8531.

21. Martinez-Veracoechea, F. J.; Escobedo, F. A. *J. Chem. Phys.* **2006,** 125, (10), 104907.

22. Larson, R. G. *J. Phys. II (Paris)* **1996,** 6, (10), 1441-1463.

23. Gonzalez-Segredo, N.; Coveney, P. V. *Europhys. Lett.* **2004,** 65, (6), 795-801.

24. Horsch, M. A.; Zhang, Z. L.; Glotzer, S. C. *J. Chem. Phys.* **2006,** 125, (18).

25. Iacovella, C. R.; Keys, A. S.; Horsch, M. A.; Glotzer, S. C. *Phys. Rev. E* **2007,** 75, (4), 040801.

26. Knorowski, C. D.; Anderson, J. A.; Travesset, A. *J. Chem. Phys.* **2008,** 128, (16).

27. Ellison, L. J.; Michel, D. J.; Barmes, F.; Cleaver, D. J. *Phys. Rev. Lett.* **2006,** 97, (23).

28. Dotera, T. *Phys. Rev. Lett.* **2002,** 89, (20), 205502.

29. Matsen, M. W.; Bates, F. S. *Macromolecules* **1996,** 29, (23), 7641-7644.

30. Hasegawa, H.; Hashimoto, T.; Hyde, S. T. *Polymer* **1996,** 37, (17), 3825-3833.

31. Schroder-Turk, G. E.; Fogden, A.; Hyde, S. T. *Eur. Phys. J. B* **2007,** 59, (1), 115-126.

32. Matsen, M. W. *Macromolecules* **1995,** 28, (17), 5765-5773.

33. Matsen, M. W. *Phys. Rev. Lett.* **1995,** 74, (21), 4225-4228.

34. Jain, A.; Toombes, G. E. S.; Hall, L. M.; Mahajan, S.; Garcia, C. B. W.; Probst, W.; Gruner, S. M.; Wiesner, U. *Angew. Chem., Int. Ed. Engl.* **2005,** 44, (8), 1226-1229.

35. Martinez-Veracoechea, F. J.; Escobedo, F. A. *Macromolecules* **2007,** 40, (20), 7354-7365.

36. Sknepnek, R.; Anderson, J. A.; Lamm, M. H.; Schmalian, J.; Travesset, A. *ACS Nano* **2008,** 2, (6), 1259-1265.

37. Schultz, A. J.; Hall, C. K.; Genzer, J. *J. Chem. Phys.* **2002,** 117, (22), 10329-10338.

38. Schultz, A. J.; Hall, C. K.; Genzer, J. *Macromolecules* **2005,** 38, (7), 3007-3016.

39. Groot, R. D.; Warren, P. B. *J. Chem. Phys.* **1997,** 107, (11), 4423-4435.

40. Groot, R. D.; Madden, T. J. *J. Chem. Phys.* **1998,** 108, (20), 8713-8724.

41. Morse, D. C.; Tyler, C. A.; Ranjan, A.; Qin, J.; Thiagarajan, R. PSCF - Home Page. http://www.cems.umn.edu/research/morse/code/pscf/home.php

42. Frenkel, D.; Smit, B., *Understanding Molecular Simulation*. Academic Press: San Diego, CA, 2002.

43. Lowe, C. P. *Europhys. Lett.* **1999,** 47, (2), 145-151.

44. Lyubartsev, A. P.; Martsinovski, A. A.; Shevkunov, S. V.; Vorontsovvelyaminov, P. N. *J. Chem. Phys.* **1992,** 96, (3), 1776-1783.

45. Escobedo, F. A.; Depablo, J. J. *J. Chem. Phys.* **1995,** 103, (7), 2703-2710.

46. Bennett, C. H. *J. Comput. Phys.* **1976,** 22, (2), 245-268.

47. Trebst, S.; Huse, D. A.; Troyer, M. *Phys. Rev. E* **2004,** 70, (4), 046701.

48. Escobedo, F. A.; Martinez-Veracoechea, F. J. *J. Chem. Phys.* **2007,** 127, (17), 174103.

49. Matsen, M. W. *J. Phys.: Condens. Matter* **2002,** 14, (2), R21-R47.

50. Fredrickson, G. H.; Ganesan, V.; Drolet, F. *Macromolecules* **2002,** 35, (1), 16-39.

51. Fredrickson, G., *The Equilibrium Theory of Inhomogeneous Polymers*. Oxford University Press: New York, 2006.

52. Tyler, C. A.; Morse, D. C. *Macromolecules* **2003,** 36, (10), 3764-3774.

53. Ranjan, A.; Qin, J.; Morse, D. C. *Macromolecules* **2008,** 41, (3), 942-954.

54. Tyler, C. A.; Morse, D. C. *Macromolecules* **2003,** 36, (21), 8184-8188.

55. Vassiliev, O. N.; Matsen, M. W. *J. Chem. Phys.* **2003,** 118, (16), 7700-7713.

56. Matsen, M. W.; Griffiths, G. H.; Wickham, R. A.; Vassiliev, O. N. *J. Chem. Phys.* **2006,** 124, (2), 024904.

57. Hajduk, D. A.; Harper, P. E.; Gruner, S. M.; Honeker, C. C.; Thomas, E. L.; Fetters, L. J. *Macromolecules* **1995,** 28, (7), 2570-2573.

58. Matsen, M. W. *J. Chem. Phys.* **1998,** 108, (2), 785-796.

59. Cochran, E. W.; Garcia-Cervera, C. J.; Fredrickson, G. H. *Macromolecules* **2006,** 39, (7), 2449-2451.

60. Fredrickson, G. H.; Helfand, E. *J. Chem. Phys.* **1987,** 87, (1), 697-705.

61. Abetz, V.; Simon, P. F. W., Phase behaviour and morphologies of block copolymers. In *Block Copolymers I*, 2005; Vol. 189, pp 125-212.

62. Mareau, V. H.; Matsushita, T.; Nakamura, E.; Hasegawa, H. *Macromolecules* **2007,** 40, (19), 6916-6921.

63. Martinez-Veracoechea, F.; Muller, E. A. *Mol. Simul.* **2005,** 31, (1), 33-43.

APPENDIX

VARIANCE MINIMIZATION OF FREE ENERGY ESTIMATES FROM OPTIMIZED EXPANDED ENSEMBLES*

I. INTRODUCTION

Estimation of free energy differences is an ubiquitous task in molecular simulation.[1] Although in some applications the free energy difference between two states can be accurately estimated by direct simulation in those two states only,[2] in many applications this "direct" approach is not feasible. In such cases a "multi-stage" approach may be necessary in which the final free energy difference is calculated as the addition of smaller, easier-to-calculate contributions between intermediate states that connect, in a reversible path, the two systems of interest.[3-5] Moreover, in some applications the free energy of the intermediate states can be of interest on its own; e.g., in the study of coexistence properties like the interfacial tension that requires accurate estimates of the free energy barrier between two phases.[6] When such a multi-stage approach is either necessary or convenient for the calculation of free energy differences, the Expanded Ensemble (EXE) methodology[7] has proven to be an efficient means to conduct the calculations. In this approach transitions between different states (stages) are attempted with fixed *a priori* probabilities, and then transitions are accepted/rejected with acceptance criteria that depend upon arbitrary biasing weights used to promote the sampling of inaccessible states. Broadly speaking there are two major approaches to the calculation of free energy differences:[8] visited states methods[9,10] and acceptance ratio methods (which are closely related to transition

matrix methods).[2,11] Visited states methods calculate free energies based on the frequencies with which each of the states is visited during the "random" walk in the expanded ensemble, hence, the statistics directly depend upon the values of the biasing weights and statistics need to be re-zeroed every time the weights are modified. Acceptance ratio methods, conversely, are based on evaluating configurational quantities whenever transitions between states are attempted; since these calculations are independent of the weights, no statistics need to be thrown away when weights are changed. In addition, acceptance ratio methods have been shown to be more efficient and to minimize user intervention.[12] Because of all the above reasons, the present work is restricted to acceptance ratio methods.

The introduction of intermediate stages between states "1" and "M" is carried out with the purpose of increasing the overlap between the relevant regions of phase space of successive macrostates, which in turn improves the accuracy of the free energy calculations.[13-15] Thus, one approach that can be used to improve the efficiency of the free energy estimation is to optimize the choice of this staging. For example, Lu and Kofke[16] showed that, when the free energy is estimated with a "one way" free energy perturbation method, the optimal staging can be approximately found by using a heuristic by which the entropy difference between successive stages is kept constant. Moreover, it has also been shown that the choice of staging can be more important than the particular method used to calculate free energy (or enthalpy) differences.[17]

Since formally speaking the ensemble averages needed in acceptance ratio methods are independent of the values of the biasing weights, these weights can be modified in order to improve the rate of convergence of these averages. This approach would then constitute an alternative procedure to improve the efficiency of the free energy calculations in which the working variables become the biasing weights (as opposed to the staging). Originally, it was thought that weights that provide a uniform

sampling frequency of states (i.e., a "flat histogram") constituted the optimal choice.[18] However, it has been shown that this is not necessary the case.[15] Trebst *et al*,[19] gave a recipe to find weights that aim to maximize the "flux" of round trips between the initial and final states of the EXE, which in principle should improve the efficiency of the free energy estimation. In recent publications,[20,21] the effect of the choice of biasing weights in the actual frequency of the round trips was investigated for both closed and open systems. However, it is still unclear if there is a direct correlation between the "flux" maximization and the minimization of the observed errors in the free energy. In the present work, we investigate if such a relation exists and additionally, to gain insight on the source of the errors, develop a methodology to obtain biasing weights that explicitly aims to minimize the variance in the free energy estimates. The uncertainties observed in the calculated free energies in different proof-of-principle applications are carefully examined in order to establish a quantitative comparison between the different methods to obtain the biasing weights [i.e., flat histogram (FH), the Optimized Ensemble method of Trebst *et al* (OE), and the one being developed in this work]. As proof-of-principle applications we study the calculation of chemical potentials of two different on-lattice systems of symmetric diblock copolymer (DBC) chains that self-assemble in a lamellar morphology. Additionally, we examine, in continuum space, the calculation of the chemical potential of a hard sphere of diameter 10*d* immersed in a system of hard spheres of diameter *d*.

II. METHODOLOGY

Expanded Ensemble Formalism

The general formalism for the EXE has been developed thoroughly elsewhere,[7,22,23] and therefore in this work we only briefly outline the basic principles of the method.

In the EXE formalism it will typically exist (at least) one molecule which will be partially coupled/decouple to/from the system. This "special" molecule will be referred henceforth as the "target" molecule and λ_i will be the label used to denote the degree of coupling to the system (e.g., number of beads of a copolymer chain, diameter of a hard sphere, etc). The EXE partition function (Q_{EXE}) with M macrostates (i.e., number of intermediate states) can be written as,

$$Q_{EXE} = \sum_{m=1}^{M} \exp(\psi_m)\, Q(\lambda_m) \tag{56}$$

where $Q(\lambda_m)$ is the partition function (in our case for the Canonical ensemble) of the system with a target molecule in the "m^{th}" state and ψ_m is an arbitrary biasing weight function. The system visits the different macrostates with probability

$$\Pi_{\psi}(\lambda) = \exp[\psi(\lambda)]\, Q(\lambda) / Q_{EXE} \tag{57}$$

In the present case we will only consider transitions between neighboring states. If such transitions are attempted with equal *a priori* probabilities (i.e., $\alpha_{ij}=\alpha_{ji}$) the acceptance criterion becomes

$$P_{acc} = \min\left\{ 1, \exp(-\vartheta + \psi_{m+\Delta} - \psi_m)\right\} \tag{58}$$

with

$$\vartheta = -\Delta \times \ln(R_w) \tag{59}$$

where R_w is the appropriate Rosenbluth factor[1] (depending upon the kind of bias that has been used) and $\Delta = \pm 1$ depending upon the transition being attempted towards a "higher/lower" macrostate. Note that if there is no configurational bias ϑ reduces simply to

$$\vartheta = \beta\left(U_{m+\Delta} - U_m\right) \tag{60}$$

where U denotes the potential energy and $\beta=1/kT$.

Thus, the usual procedure consists on calculating free energy differences between neighboring states, which are then added up to obtain the total free energy between the states "1" and "*M*". For the specific case of calculating "excess" chemical potentials $\beta\mu^{ex}$ (i.e., chemical potential without the ideal chain contributions) in the Canonical ensemble we have,

$$\beta\mu^{ex}(\lambda_1 \to \lambda_M) = [\beta A(\lambda_M) - \beta A(\lambda_1)]/\Delta N_{ch} = \sum_{m=1}^{M-1} \Delta\beta A_{m,m+1} \tag{61}$$

where $A(\lambda_m)$ is the Helmholtz free energy of the system with a target chain in the m^{th} state, $\Delta\beta A_{m,m+1}$ is the free energy difference between any two neighboring macrostates and ΔN_{ch}=1 is the number of entire molecules being coupled/decoupled. In this way, when the change in the order parameter λ (e.g., number of copolymer beads, diameter of hard sphere, etc.) can be controlled at will, the problem of calculating the free energy difference between multiple macrostates reduces to several "two-states" problems, for which the acceptance ratio methods to estimate free energy differences are well suited.

Free energy estimation

It is straightforward to prove[2] that the free energy difference between two systems ("0" and "1") can be calculated with

$$\Delta\beta A = \ln[\frac{\langle W \exp(-\beta U_0)\rangle_1}{\langle W \exp(-\beta U_1)\rangle_0}] = \ln[\frac{\langle \chi_0 \rangle_1}{\langle \chi_1 \rangle_0}] \tag{62}$$

where W is a finite arbitrary function of the configuration space, the brackets denote ensemble average under the Hamiltonians of the respective systems and the last equality is just the definition of the functions to be averaged, χ_0 and χ_1. For example for the choice,[2]

$$W = \min\{\exp(\beta U_0), \exp(\beta U_1)\} \tag{63}$$

these functions reduce to the familiar Metropolis rule,[24]

$$\begin{aligned}\chi_0 &= \min\{\exp[-\beta(U_0 - U_1)], 1\} \quad \text{and} \\ \chi_1 &= \min\{\exp[-\beta(U_1 - U_0)], 1\}\end{aligned} \tag{64}$$

and the free energy difference can be straightforwardly calculated from (62).

Likewise, for the choice:

$$W = \left[\exp(-\beta U_0) + \exp(-\beta U_1)\right]^{-1} \tag{65}$$

we obtain,

$$\begin{aligned}\chi_0 &= \left\{1 + \exp[\beta(U_0 - U_1)]\right\}^{-1} \quad \text{and} \\ \chi_1 &= \left\{1 + \exp[\beta(U_1 - U_0)]\right\}^{-1}\end{aligned} \tag{66}$$

which is Barker's acceptance rule.[25]

As it was showed by Bennett,[2] in the large sample regime, independently of the choice of the W function, the variance on the free energy estimate can be calculated with,

$$\sigma^2 \equiv \mathrm{var}(\Delta\beta A) = \frac{1}{\ell_{0\to1}}\left[\frac{\left\langle(\chi_1)^2\right\rangle_0}{\left(\langle\chi_1\rangle_0\right)^2} - 1\right] + \frac{1}{\ell_{1\to0}}\left[\frac{\left\langle(\chi_0)^2\right\rangle_1}{\left(\langle\chi_0\rangle_1\right)^2} - 1\right] \tag{67}$$

where $\ell_{0\to1}$ is the number statistically independent transitions, attempted from system 0 to system 1 ($\ell_{1\to0}$ is defined similarly). Since the function W is arbitrary, it can be chosen to minimize the variance, [i.e., minimizing eq. (67)]. This minimization procedure leads to a variational problem with the solution,[2]

$$W = \left[\exp(-\beta U_0) + \exp(C - \beta U_1)\right]^{-1} \tag{68}$$

where

$$C = \ln\left[\frac{Q_0 \ell_{1\to0}}{Q_1 \ell_{0\to1}}\right] \tag{69}$$

with Q_i the Canonical partition function of the i system (i equals either "0" or "1"). Thus, leading to Bennett's acceptance ratio formula,[2]

$$\Delta\beta A = \ln[\frac{\left\langle \left\{1+\exp[\beta(U_0 - U_1 + C)]\right\}^{-1} \right\rangle_1}{\left\langle \left\{1+\exp[\beta(U_1 - U_0 - C)]\right\}^{-1} \right\rangle_0}] + C \tag{70}$$

or in term of the χ functions

$$\begin{aligned} \chi_0 &= \exp\left[C\right] / \left\{1+\exp[\beta(U_0 - U_1 + C)]\right\} \quad \text{and} \\ \chi_1 &= \left\{1+\exp[\beta(U_1 - U_0 - C)]\right\}^{-1} \end{aligned} \tag{71}$$

Note that if the macrostate transitions are attempted with configurational bias, all these equations are readily applicable by making a substitution analogous to the one presented in equations (59) and (60).

Equation (70) is valid regardless of the value of *C* employed, yet only the value of *C* given by (69) yields a minimum variance. However, since the ratio Q_0/Q_1 is not initially known the optimal value of *C* has to be found from the following implicit equation,

$$\ell_{1\to 0} \left\langle \chi_0 \right\rangle_1 = \ell_{0\to 1} \left\langle \chi_1 \right\rangle_0 \tag{72}$$

where the reader is reminded that the χ's are functions of C. Since the variance reaches a minimum for the optimal value of *C*, the next relation also follows,

$$\left. \frac{\partial \sigma^2}{\partial C} \right|_{C_{opt}} = 0 \tag{73}$$

Error minimization

The $\Delta\beta A$ is a function only of ensemble averages whose "true" value does not formally depend on the number of attempted transitions (i.e., $\ell_{0\to 1}$ and $\ell_{1\to 0}$). In practice, however, where only a finite number of samples is available, the accuracy and precision of these averages can strongly depend on the values of the $\ell_{i\to j}$. The dependence of the precision on these quantities becomes clear from the expression for the variance in eq. (67). When the single-stage procedure is generalized to a multi-

stage one (e.g., EXE), the total variance of the free energy difference between macrostates "1" and "*M*" can be estimated by the sum of the individual contributions,

$$\sigma_{tot}^2 = \sum_{m=1}^{M-1} \sigma_{m,m+1}^2 \tag{74}$$

where again, the variance associated with each one of the $\Delta\beta A_{i,i+1}$ is given by,

$$\sigma_{i,i+1}^2 = \frac{1}{\ell_{i\to i+1}}\left[\frac{\left\langle \left(\chi_{i\to i+1}\right)^2 \right\rangle_i}{\left(\left\langle \chi_{i\to i+1}\right\rangle_i\right)^2} - 1\right] + \frac{1}{\ell_{i+1\to i}}\left[\frac{\left\langle \left(\chi_{i+1\to i}\right)^2 \right\rangle_{i+1}}{\left(\left\langle \chi_{i+1\to i}\right\rangle_{i+1}\right)^2} - 1\right] = \frac{\omega_{i\to i+1}}{\ell_{i\to i+1}} + \frac{\omega_{i+1\to i}}{\ell_{i+1\to i}} \tag{75}$$

where we have defined for convenience the quantities,

$$\omega_{i\to i+1} \equiv \frac{\left\langle \left(\chi_{i\to i+1}\right)^2 \right\rangle_i}{\left(\left\langle \chi_{i\to i+1}\right\rangle_i\right)^2} - 1 \tag{76}$$

In the long run, the number of transitions attempted from macrostate "*i*" to macrostate "*j*" is related to the total number of times (ℓ_i) that macrostate "*i*" has been visited,

$$\ell_{i\to j} \approx \alpha_{ij}\ell_i \tag{77}$$

and since in our case we only allow transitions between neighboring macrostates and with equal *a priori* probabilities, the total variance assumes the simple form,

$$\sigma_{tot}^2 = 2\sum_{m=1}^{M-1} \frac{\omega_{m\to m+1}}{\ell_m} + \frac{\omega_{m+1\to m}}{\ell_{m+1}} \tag{78}$$

From eq. (57), it can be seen that in the long run,

$$\ell_i \sim \exp[\psi_i - \beta A(\lambda_i)] \tag{79}$$

thus showing that the choice of ψ_i's can be used to manipulate the expected precision of the free energy estimation.

The Flat Histogram and the Optimized Ensemble Methods

Hitherto, two well-known approaches to determine the weights have been proposed: flat histogram approach (FH) and the methods of Trebst *et al*[19] (OE). In the FH approach all the macrostates are visited with equal frequency, this is achieved by setting $\psi_i = \beta A_i$ [c.f., eq. (79)]. This approach is by far the most used in the literature; however, it has recently been shown to sometimes yield suboptimal results.[19-21] More recently, Trebst *et al.*[19] proposed a different method in which the free energy estimation is optimized by maximizing the steady state "current" between macrostates λ=1 and λ =*M*, estimated as,

$$J = D(\lambda)\,\Pi(\lambda)\frac{dx(\lambda)}{d\lambda} \tag{80}$$

where $D(\lambda)$ is the walker's diffusivity at state λ and $x(\lambda)$ is the fraction of times that the walker at state λ has had a label "+". The walker's label is assigned depending on the extreme λ-state that it visited last: if the most recent extreme-state visited was λ=1 (i.e., fully decoupled molecule) the walker's label becomes "–"; on the other hand, if the most recent visit was to λ=*M* (i.e., fully coupled molecule) the label becomes "+". Trebst *et al*. recipe for maximizing the current dictates the optimal weights be given by the iteration formula

$$\psi(\lambda_i) = \beta A(\lambda_i) - \frac{1}{2}\ln\left(D(\lambda_i)\right), \tag{81}$$

with

$$D(\lambda_i) = \left[\Pi_{\psi}(\lambda_i)\,dx/d\lambda\right]^{-1} \tag{82}$$

note that while the Helmholtz energy here can be efficiently calculated using Bennett's method without loss of information, the quantity in the argument of the logarithm depends on the biasing weights used and hence, needs to be re-zeroed at every iteration.

The MinVar method

In the following we propose a third method in which the biasing weights are chosen to directly minimize the variance in free energy estimation while keeping the total amount of "sampling" fixed. Thus, we will refer to this method as the "MinVar" method. In order to minimize the estimated variance we construct the Langrangian (Γ),

$$\Gamma \equiv \sigma_{tot}^2 + \alpha \sum_{m=1}^{M} \ell_m \tag{83}$$

where α is just a Lagrange multiplier. Since the ℓ_i are monotonic functions of the ψ_i the minimization can be carried out with respect to either set of variables. Thus by differentiation we obtain,

$$\begin{aligned} &\frac{\partial \Gamma}{\partial \ell_i} = -\frac{1}{\ell_i^2}\left(\omega_{i\to i+1} + \omega_{i\to i-1}\right) + \alpha = 0;\ i \in [1, M] \text{ with} \\ &\omega_{1\to 0} = \omega_{M\to M+1} = 0 \end{aligned} \tag{84}$$

since the states λ=0 and λ=M+1 do not exist. Solution of (84) gives,

$$\ell_i = \text{constant} \times \sqrt{\omega_{i\to i+1} + \omega_{i\to i-1}} \tag{85}$$

or in terms of the biasing weights

$$\psi_i = \beta A_i + \frac{1}{2}\ln[\omega_{i\to i+1} + \omega_{i\to i-1}] + \text{constant} \tag{86}$$

where the constant is arbitrary since only the *differences* in the biasing weights are meaningful. Throughout this work we have set the constant so that ψ_1=0. It is interesting that despite the similarity of the form of Eqs. (81) and (86), their derivation is totally independent from each other. Moreover, in (86) the quantity in the logarithm's argument is weight independent (for fixed C's) and hence, need *not* to be re-zeroed every time the ψ_i's are modified.

A subtle point has to be taken into account for the application of equation (86) when using the optimal W function [c.f., eq. (68)]. In this case, there will exist a constant C_i associated with each one of the M-1 pairs of neighboring macrostates. If one minimizes the variance with respect to C_i at fixed N_i, one obtains:

$$\frac{\partial \Gamma}{\partial C_i} = \frac{\partial \sigma_{tot}^2}{\partial C_i} = \sum_{m=1}^{M-1} \frac{\partial \sigma_{m+1,m}^2}{\partial C_i} = 0; \; i \in [1, M], \tag{87}$$

which according to eq. (73), is automatically satisfied if the optimal C_i is used for the calculation of each one of the free energy increments, $\Delta\beta A_{i,i+1}$. However, the optimal value of the C_i depends through eqs. (72) and (77) on the ℓ_i. Hence, when using biasing weights to minimize the variance together with the optimized Bennett's acceptance ratio method, eqs. (72) and (85) have to be solved self-consistently in order to obtain the biasing weights that will provide the minimum possible estimated total variance. Since in order to solve this system of equations we need ensemble averages of various functions (e.g., $\chi_{i\to i+1}$ and $\chi_{i+1\to i}$) that depend on the value of C_i, it would seem that every time that the C_i's are modified (e.g., while solving the equations above) we need to re-zero all the averages in the simulation. In practice however, one can keep averages for a sufficiently large number of different values of C_i, roughly spanning the range of interest, and whence the intermediate values can be obtained by means of linear interpolation.

III. MODEL SYSTEMS

Symmetric Diblock Copolymer of length N_{DBC}=10

The first system that we used as an example is a melt of symmetric DBC of chain length N_{DBC}=10. Simulations were carried out in a lattice of coordination number c=26, unit energy is assigned only between the different-type beads that are in contact. This model has been used extensively in the study of DBC and the details can

be found elsewhere.[26-28] The system was simulated with a void fraction η_{void}=0.25 and at β=0.25.

Calculations of the chemical potential of the DBC system were carried out with two different choices of staging for the EXE. In the first case, "A", addition of each bead of the chain constitutes a different macrostate. In the second case, "B", all the beads are added individually except the 6th, 7th and 8th beads which are added together as a unique macrostate.

Symmetric Diblock Copolymer of length N_{DBC}=4

The second system studied is also a melt of symmetric DBC but with a chain length N_{DBC}=4. The details of the lattice are equal to the system explained above. The system was simulated with a void fraction η_{void}=0.25 and at β=0.5.
Two different ways of partitioning the DBC chain are studied. "A": Each single bead is added individually. "B": The first two beads are added individually while the last two beads are added together.

In both DBC systems (i.e., N_{DBC}=4 and N_{DBC} =10) macrostate transitions are attempted with a frequency of four attempts per MC cycle, where an MC cycle is defined by a number of MC moves (i.e., hops, reptations and switches)[29] equal to the total number of beads present in the system. All the lattice simulations were carried out in a simulation box of size L_{box} =10 and presented a lamellar morphology after equilibration.

Large hard sphere immersed in a small-hard-sphere system

The third system examined consisted of 1350 small hard-spheres of diameter "*d*" in a cubic box of fixed side length of 30 *d*. The aim of the simulation is to obtain the chemical potential of a large hard sphere of diameter 10*d* via the EXE method

previously described in the section on *Methodology*. In this case, the coupling parameter is the diameter of the large sphere d^* that varies from 0 to $10d$ through 9 equally-spaced intermediate steps (i.e., M=11), so that $\{d^*\}=\{0,1,2,3,4,5,6,7,8,9,10\}$ in units of d. Simulations entailed 10^7 cycles, each cycle consisting of 1350 translation moves (with amplitude calibrated to give a 30% average acceptance rate) and 3 attempted λ-transitions.

IV. RESULTS

Diblock Copolymer melts

In the following, we present a systematic study of the uncertainty in the calculation of the excess chemical potential in two DBC systems. We examine the effect on the observed errors of different sets of biasing weights obtained by three different methods (i.e., FH, OE, and MinVar). We also compare the use of the optimized Bennett's acceptance ratio method with a sub-optimal version where we have set C=0. The reason for this being that often in the literature free energy calculations have been carried out using the sub-optimal version due to its alleged simplicity. Additionally, we explore the effect of different choices of staging to connect macrostate "1" with "M".

We start by analyzing the evolution of the mean absolute error, $<e>$,

$$< e >= \left\langle abs\left(\beta\mu^{cal} - \beta\mu^{exact} \right) \right\rangle \tag{88}$$

as a function of the number of MC cycles. The ensemble averages are made with a large enough number of independent simulations (i.e., 2000) for which the uncertainty in the calculated values of the quantity $<e>$ is less than 2%.

We start by showing the results for the system of symmetric DBC with N_{DBC}=10. The "exact" value of chemical potential for this system at the conditions

studied is $\beta\mu^{exact}$=24.5025(3). In Figure A.1 we present a log-log plot of $<e>$ as a function of the number of MC cycles for the FH, OE and MinVar methods using the sub-optimal acceptance ratio method (i.e., C=0) to calculate the free energy. In Figure A.1a the staging "A" has been used (i.e., each bead is added individually), while in figure A.1b the staging "B" has been used (i.e., beads 6, 7, and 8 are added together). In both figures straight lines of slope -1/2 are observed, which is consistent with the expected behavior that the error diminishes with the square root of the number of sampling points. However, an interesting difference between Figures A.1a and A.1b is observed; in Figure A.1a, where the "A" staging has been used, all the methods yield approximately the same accuracy, while in Figure A.1b, with the "B" staging, the MinVar method yields the least error of the three methods while the FH method is obviously the worst. Another important difference is that, for a fixed amount of MC cycles, the "A" staging has values of $<e>$ much lower than the "B" staging. For example, the worst case scenario for the "A" staging (i.e., the FH method) has a final value of $<e> = 9.9\times10^{-3}$ while for the best case scenario of the "B" staging (i.e., the MinVar method) the error is higher (i.e., $<e> = 1.1\times10^{-2}$). These results show that at least for this case the choice of staging seems to be more important than the actual selection of the weights. Moreover, once the chemical potential calculations have been optimized with a relatively "good" staging, the improvement that can be made by modifying the weights is only marginal. Nevertheless, if we have made a "poor" selection of staging, where presumably the variance of the different stages differ by orders of magnitude, the accuracy can be significantly improved by a suitable choice of the ψ_i's.

Next we present the results where the optimal acceptance ratio method (i.e., $C=C_{opt}$) has been used for the free energy calculations. Similarly, we present in Figures A.2a and A.2b, for staging "A" and "B" respectively, log-log plots of $<e>$ as

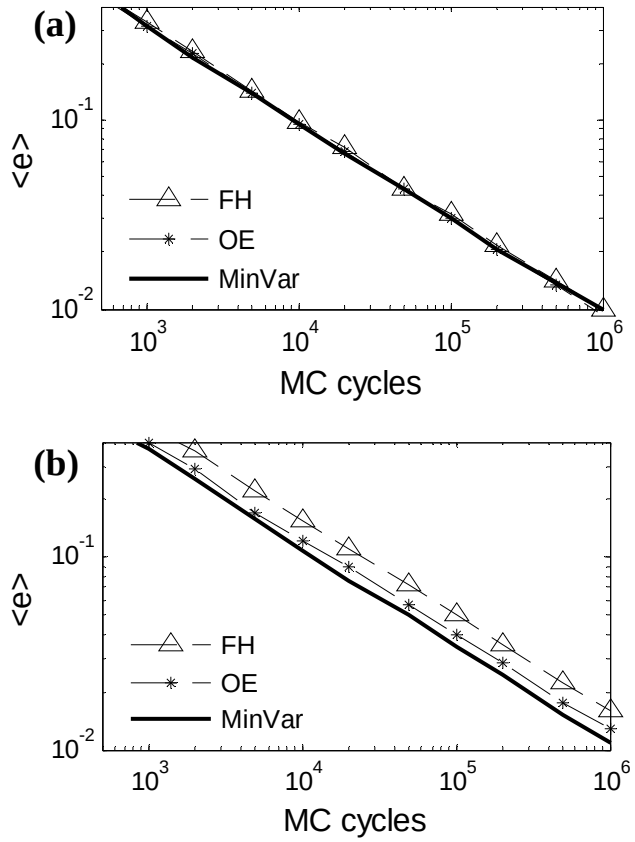

Figure A.1. Log-Log plot of <*e*> as a function of the number of MC cycles for the FH, OE and MinVar methods. The system studied was a melt of symmetric DBC with N_{DBC}=10. Free energy calculations were made using the sub-optimal (i.e., C=0) method. (a) The chain is partitioned using staging "A". (b) The chain is partitioned using staging "B". Only with staging "B" the difference among methods becomes significant.

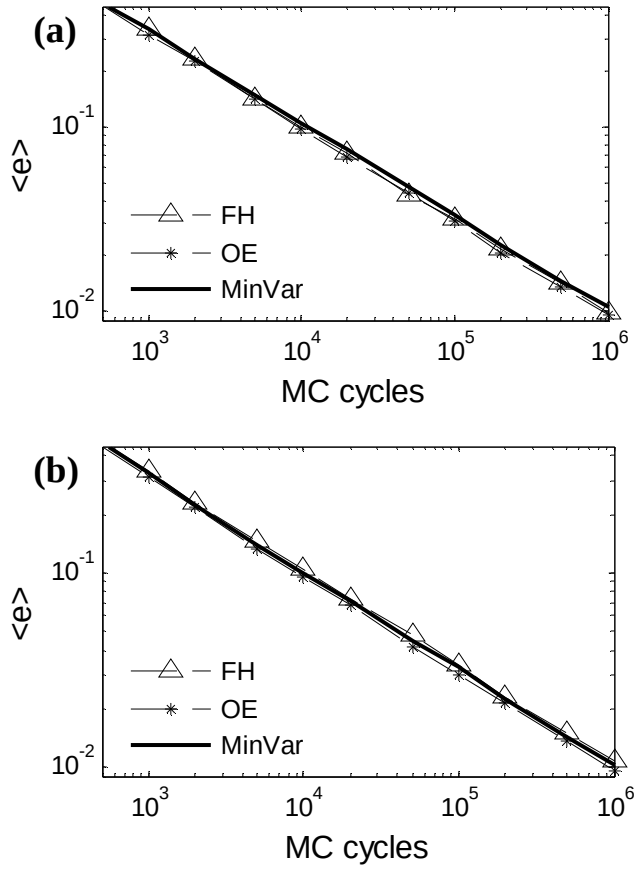

Figure A.2. Log-Log plot of $<e>$ as a function of the number of MC cycles for the FH, OE and MinVar methods. The system studied was a melt of symmetric DBC with N_{DBC}=10. Free energy calculations were made using optimized Bennett's acceptance ratio method[2] (i.e., $C=C_{opt}$) method. (a) The chain is partitioned using staging "A". (b) The chain is partitioned using staging "B". The accuracy obtained using C_{opt} is fairly insensitive to the choice of staging and the biasing weights used.

a function of the MC cycles for the three different methods. Interestingly, it can be observed that the two figures are strikingly similar: in both of them the three different methods yield comparable results and the minimum achieved error was of about the same [i.e., $\langle e \rangle^{"A"} = 9.5\times10^{-3}$ and $\langle e \rangle^{"B"} = 9.6\times10^{-3}$]. Thus usage of the optimized Bennett's acceptance ratio method seems to make the calculation of free energy differences, for the present system, less sensitive to both the choice of staging and the specific biasing weights. In addition, for both choices of staging the method that achieved the minimum error was the method of Trebst *et al* (OE); and for the "A" staging, with $C=C_{opt}$, the MinVar method was actually slightly worse than FH.

In order to explore the system dependence of the trends observed previously we present now the results obtained for the system of symmetric DBC with N_{DBC}=4 where the exact value of chemical potential is taken to be $\beta\mu^{ex}$=15.2621(3). We start with the results obtained when the free energy differences were estimated using the sub-optimal (C=0) acceptance ratio method. In Figure A.3a we show a log-log plot of $\langle e \rangle$ as a function of the MC cycles, where the "A" staging has been used. Figure A.3b is similar to 3a but with the "B" staging instead (i.e., the 3rd and 4th bead are added together). The results are very similar to the ones obtained for the system with N_{DBC}=10. The "A" staging performs in general much better than the "B" staging. We only observe significant difference between the choice of biasing weights for the staging "B", where the MinVar method clearly outperforms the rest. An interesting feature is that the MinVar method in Figure A.3b deviates at the early stages of the simulation (i.e., < 3000 MC cycles) from the expected linear scaling with slope -1/2. This happens because as we will discuss again later, the weights obtained by the MinVar severely increase the time needed to make a "round trip" between the macrostates "1" and "M". As a consequence, at the beginning of the simulation the system takes much longer times to visit the "upper" macrostates, thus precluding the

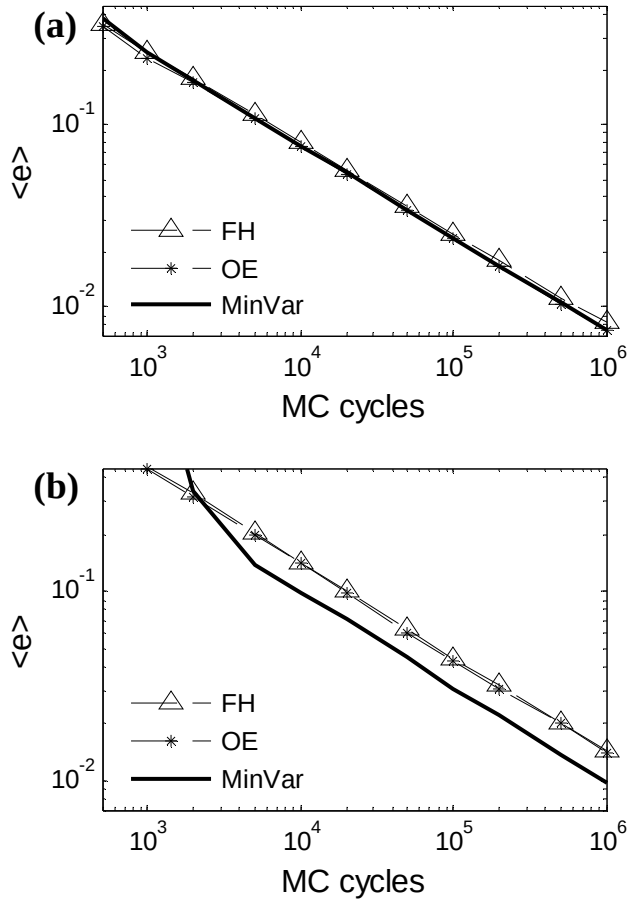

Figure A.3. Log-Log plot of $<e>$ as a function of the number of MC cycles for the FH, OE and MinVar methods. The system studied was a melt of symmetric DBC with N_{DBC}=4. Free energy calculations were made using the sub-optimal (i.e., C=0) method. (a) The chain is partitioned using staging "A". (b) The chain is partitioned using staging "B". Although initially departing from the expected scaling, the MinVar method yields a smaller $<e>$ than the other methods in the long run.

estimation of the free energy differences between these macrostates at the early stages of the simulation when no statistics have yet been accumulated. By convention we set the free energy difference between two neighboring macrostates equal to zero if no statistics have been collected.

In the following we present the results when the free energy is calculated using the optimal acceptance ratio method. In Figures A.4a and A.4b we show the results obtained for "A" and "B" staging. The figures show log-log plots of $<e>$ versus MC cycles for the three different methods to calculate ψ_i. Similarly to the behavior observed for N_{DBC}=10, when $C=C_{opt}$, we see little dependence in the staging and in the method employed. Contrary to what was observed in the sub-optimal case, the "B" staging is now observed to reach results that are slightly more accurate than with the "A" staging (i.e., $<e>^{"A"} = 6.7\times10^{-3}$ and $<e>^{"B"} = 5.6\times10^{-3}$). As we will discuss later this is a consequence of the fact that having less stages can accelerate the number of round trips which in turn helps de-correlating the statistical samples. Finally, notice again that the MinVar method does not seem to be reaching the minimum variance that was expected to yield; in particular, for staging "A" this method gives the worst results.

The fact that the MinVar method is not always yielding the minimum error in all the cases studied suggests that the observed deviations from the exact value are coming from a mechanism that has not yet been considered. In order to shed light into this issue we calculated the "ideal" total variances (σ^2_{id}) as estimated directly from eq. (78) and compared them with the "real" total variance (σ^2_{real}) calculated as the sum of the observed variances of each one of the $\Delta\beta A_{i,i+1}$, again calculated from 2000 independent runs of 10^6 MC cycles. We first examine the system of DBC with N_{DBC}=10 with "B" staging. In Figure A.5a we show the "ideal" and "real" total variances of the calculated chemical potential, calculated with C=0, for the FH, OE

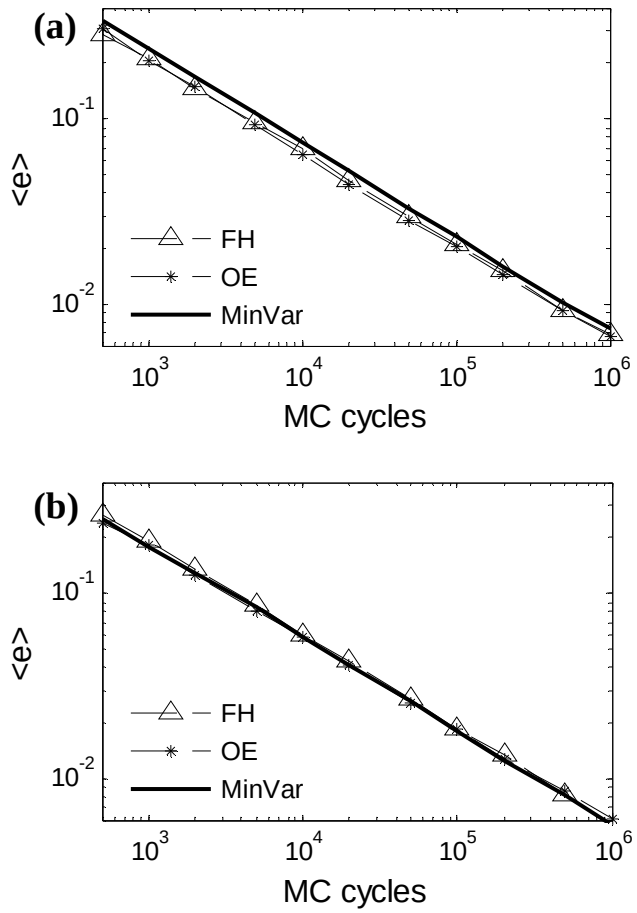

Figure A.4. Log-Log plot of $<e>$ as a function of the number of MC cycles for the FH, OE and MinVar methods. The system studied was a melt of symmetric DBC with N_{DBC}=4. Free energy calculations were made using optimized Bennett's acceptance ratio method[2] (i.e., $C=C_{opt}$) method. (a) The chain is partitioned using staging "A". (b) The chain is partitioned using staging "B". The "B" staging yields in general better results.

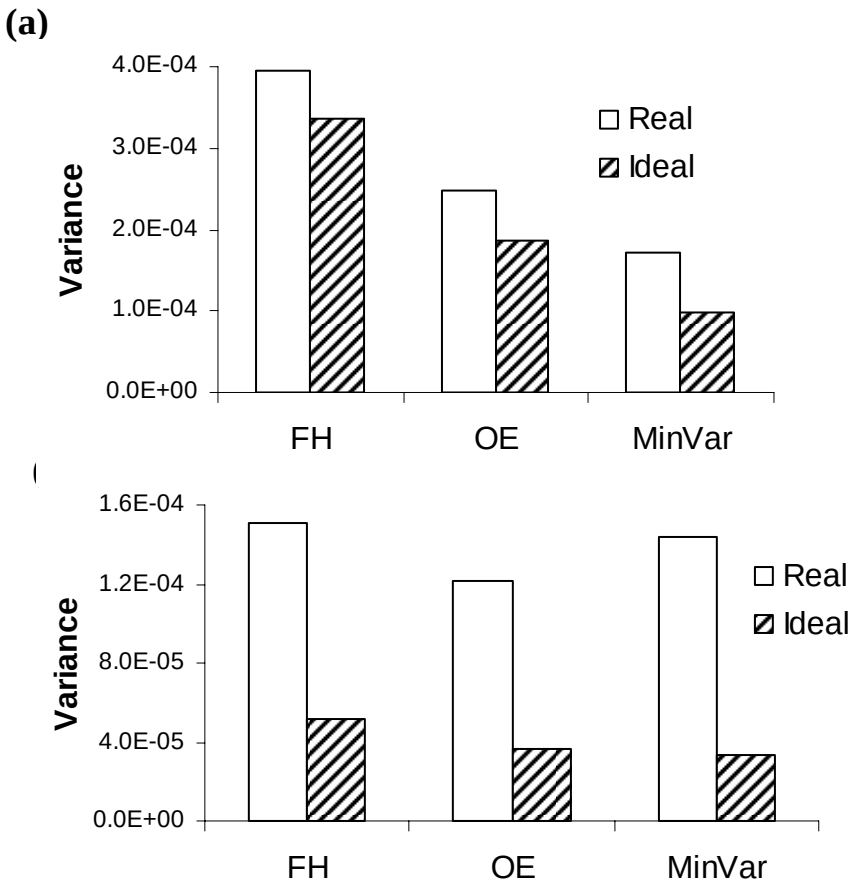

Figure A.5. Plot of the "ideal" and "real" total variances of the calculated chemical potential using the FH, OE, and MinVar methods to estimate the biasing weights. The calculations were made in the system of DBC with N_{DBC}=10 using staging "B". Free energy calculated via (a) The sub-optimal (i.e., C=0) method and (b) the optimized (i.e., $C=C_{opt}$) acceptance ratio method.

and MinVar methods. In this case the MinVar method yields the lowest "ideal" and "real" variances. However, it is interesting to note that the real variances are always larger than the ideal ones, being precisely for the MinVar method where this difference is the greatest. In Figure A.5b we present a similar plot but where the value $C=C_{opt}$ has been used in the free energy calculations. Though, in general the values of "real" variance are, as expected,[13] lower in the $C=C_{opt}$ case than in the $C=0$ case (note the different scales), the improvement is not as dramatic as the "ideal" values suggest. Moreover, in the $C=C_{opt}$ case, the difference between "ideal" and "real" values significantly increases, with again the MinVar method having the greatest difference. Finally, it is clear from Figure A.5b that the MinVar method does not yield the minimum "real" variance (even though it has the lowest value of σ^2_{id}). Similar conclusions can be drawn (results not shown) for the case where the staging "A" is used to partition the DBC chain (though in this case the differences between the $C=C_{opt}$ and $C=0$ results are smaller).

The fact that the observed "real" variances are systematically larger than the values predicted by eq. (78) is a clear indication of lack of statistical independence between the samples used for the various ensemble averages needed to calculate free energy differences. In the EXE approach a target chain is sequentially coupled/decoupled to the system and statistics are gathered every time a transition between macrostates is attempted. However, if transitions between macrostates are attempted reasonably often, it is very likely that the local environment surrounding the target DBC chain has not significantly changed between successive attempts, thus yielding essentially redundant results. This is especially true if the system possesses highly correlated spatial patterns like the lamellar morphology (or any other regular mesophase) in which the DBC chains arrange. In this type of systems, it is not enough

for the target chain to accurately sample its local environment since its location most likely will not be representative of the whole (very heterogeneous) system.

In the EXE formalism once the target chain is totally decoupled it is reinserted at a random point in the simulation box. Moreover, once the target chain is totally coupled, it becomes undistinguishable from any other, and hence, it can exchange identity with a randomly chosen "regular" chain. Because of this, maximizing the number of times the target chain goes from macrostate "1" to "*M*" and vice versa, that is, minimizing the average time τ^{RT} (i.e., number of insertion/deletion attempts) needed to make a round trip, will help de-correlate the samples and under some circumstances minimize the variance.

Thus, minimizing σ^2_{real} entails a compromise between minimizing σ^2_{id} and de-correlating the samples as much as possible. Now it becomes clear the reason for the difference in the performance of the three different methods in the different cases studied. When the EXE setup is significantly sub-optimal, σ^2_{id} can be significantly minimized by the right choice of biasing weights (e.g., Figure A.5a) and in this case the MinVar method helps. However, when EXE has been optimized, either by using $C=C_{opt}$ or by a suitable choice of staging, the value of σ^2_{id} can only be marginally diminished by means of the biasing weights. In this case, the maximum attainable accuracy is limited by the lack of statistical independence within the samples. Therefore, at least in the cases studied in the present work, if one blindly minimizes σ^2_{id} while significantly increasing the correlations, the results will actually become less accurate. Under these circumstances, the minimum error is obtained by de-correlating the samples which as we have suggested should be related to minimizing τ^{RT}.

For the DBC systems studied, the MinVar method significantly increased τ^{RT}. For example, for the case studied in Figure A.5b (i.e., N_{DBC}=10, $C=C_{opt}$ and "B"

staging) the round trip times (measured in number of transition attempts per completed round trip) are: τ_{FH}= 570, τ_{OE}=531, and τ_{MinVar}=932. The increase of τ^{RT} with the MinVar method is also observed (results not shown) when the "A" staging is used and for the system of DBC chains with N_{DBC} = 4. These results are consistent with the previously observed fact that the largest discrepancies between σ^2_{id} and σ^2_{real} were always attained for the MinVar method. In most cases the lowest τ^{RT} was obtained with the OE method, [the only exception being the N_{DBC}=4 system with "B" staging for which the low number of macrostates introduces discretization errors in eq. (81)].

To gain further insight about why in the systems studied the MinVar method does not reduce the inaccuracies in all circumstances, we examine the individual "real" and "ideal" variances of each one of the free energy increments $\Delta\beta A_{i,i+1}$. Here for convenience, we identify each of the "increments" by its index "*i*". As a representative example we show in Figures A.6a and A.6b the variances observed, in linear and logarithmic scales respectively, for the N_{DBC}=10 system, with C=C_{opt} and "B" staging. In this case we only compare the MinVar and the OE method. Since the optimal values of C for each one of the increments can be estimated as $C_{opt,i}$= $\Delta A_{i,i+1}$ +ln$\left(\ell_{i+1\to i}/\ell_{i\to i+1}\right)$, the $C_{opt,i}$ are approximately of the same order of magnitude of their corresponding $\Delta A_{\mathrm{i,i+1}}$ for each of the methods used to calculate the biasing weights. The values $\Delta A_{\mathrm{i,i+1}}$ obtained for the "B" staging were $\Delta A_{\mathrm{i,i+1}}$ ={2.70;2.11;2.07;2.07;2.07;9.24;2.14;2.11}. In Figure A.6 it can be seen that by far the largest variance is the one associated with the free energy difference between macrostates 6$^{\mathrm{th}}$ and 7$^{\mathrm{th}}$ (i.e., increment number 6), wherein three beads (i.e., number 6, 7, and 8) are inserted at the same time. Although, the ideal value of this variance for the MinVar method is lower, the real variance turns out to be higher. In Figure A.7 we show the equilibrium relative frequencies with which the system visits each macrostate for the two methods. The MinVar method attempts to reduce the variance

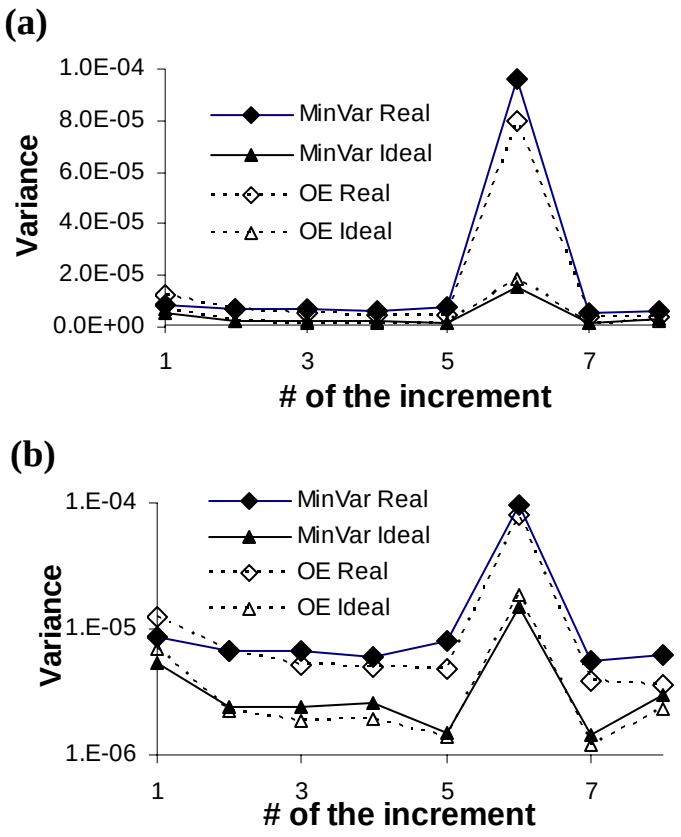

Figure A.6. Plot of the individual "real" and "ideal" variances of each one of the free energy increments $\Delta\beta A_{i,i+1}$. We identify each of the "increments" by its index "i". These results were obtained for the DBC system with N_{DBC}=10 system, $C=C_{opt}$ and the "B" staging. We only compare the MinVar and the OE methods. (a) Linear scale. (b) Logarithmic scale.

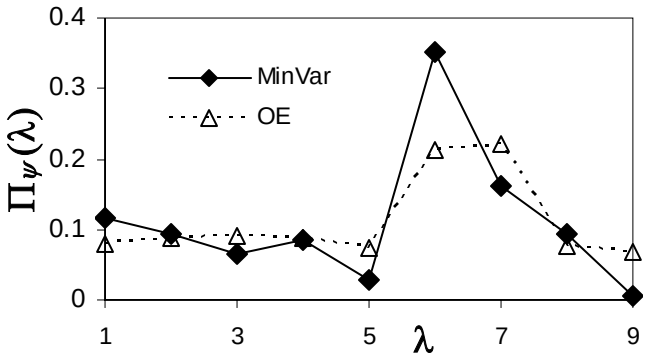

Figure A.7. Plot of the relative frequencies with which the system visits each macrostate. These results were obtained for the DBC system with N_{DBC}=10 system, C=C_{opt} and the "B" staging. We only compare the MinVar and the OE methods. The system gets trapped in the neighborhood of the 6th macrostate when using the MinVar method.

by significantly concentrating the sampling in the 6th macrostate. However, since the frequency of visits to some of the surrounding states is especially low (e.g., 5th and 9th), once the system goes to the 6th macrostate it will likely remain "trapped" in this macrostate (and its surroundings) for a significant portion of the simulation. Therefore, despite the higher number of samples in the "difficult" stage, we obtain a lower quality in the statistics due to the effect of the correlations and thus, poorer estimates in the free energy. This evidently also increases the round trip times. Conversely, the more global character of the OE method allows for improving the quality of the samples by de-correlating them while also concentrating the sampling, though not as intensively as the MinVar method, in the difficult areas. Finally, from Figure A.6b it can be observed that the minimum relative differences between "real" and "ideal" variances are always observed in the free energy increments located in the two extremes, which precisely correspond to the macrostates where, as previously discussed, should exist the least correlations.

To certain extent, the calculation of the chemical potential of a melt of DBC is a challenging test for the MinVar method since its success strongly depends on the premise of sample points being statistically independent but, as we mentioned before, the very specific spatial correlation presented in the DBC mesophases makes the coupling/decoupling attempts highly correlated. Therefore, we would expect that in a more homogenous system where the local environment is essentially the same throughout the system, the MinVar method should be more successful. To show this, we now examine the calculation of the chemical potential of one hard sphere of diameter 10d immersed in a fluid of hard spheres of diameter 1d.

Solvation of large sphere solvate in system of small spheres.

This hard-core system provides a limiting testbed in that the free-energy is of purely entropic origin (excluded volume). This system is also interesting because the use of the optimized Bennett's method with C_{opt}'s provides no improvement.[15] This is because $\exp(-\mathcal{G})$ is either 0 or 1 depending on whether the transition entails an overlap or not, respectively [e.g., $\exp(-\mathcal{G})$ is always unity for transitions that reduce the sphere diameter]; it is easy to show then that free-energy calculations always reduce to the 'unoptimized' acceptance ratio method and that

$$\omega_{i\to i+1} = \frac{\ell_{i\to i+1}}{\ell^*_{i\to i+1}} - 1 \tag{89}$$

where ℓ^* denotes the number of *successful* (non-overlapping) macrostate transitions and ℓ still represents the total number of *attempted* transitions.

As with the DBC system, we examine the sampling efficiency of the FH, OE, and MinVar methods but measuring the statistical variance in $\beta\mu^{\text{ex}}$ of the large sphere for a fixed computational cost (10^7 cycles), assuming that for each method suitable ψ weights have *already* been obtained (for all states) and are fixed. The EXE consisted of eleven (11) macrostates in which the target sphere diameter (d^*) was uniformly spaced between the states d^*=0 and d^*=10d, where d is the diameter of the small spheres. Thus, the macrostate number λ corresponds to different diameters of the large sphere; i.e., $d^* = (\lambda\text{-}1)d$. Histograms of λ-state visits are shown in Figure A.8, showing that, although both the OE and MinVar methods concentrate the sampling on the state before last ($\lambda_{M\text{-}1}$=10), the MinVar method does more so. In fact (and as expected), in the MinVar method the fully coupled state is never actually visited [it follows from Eq. (89) that $\omega_{M\to M-1} = 0$], forsaking the trivial $\lambda_M \to \lambda_{M\text{-}1}$ transition, which provides no useful information,[15] in favor of the hardest one: $\lambda_{M\text{-}1} \to \lambda_M$ (one could argue, however, that the λ_M is *virtually* visited in the sense of the *insertions* in

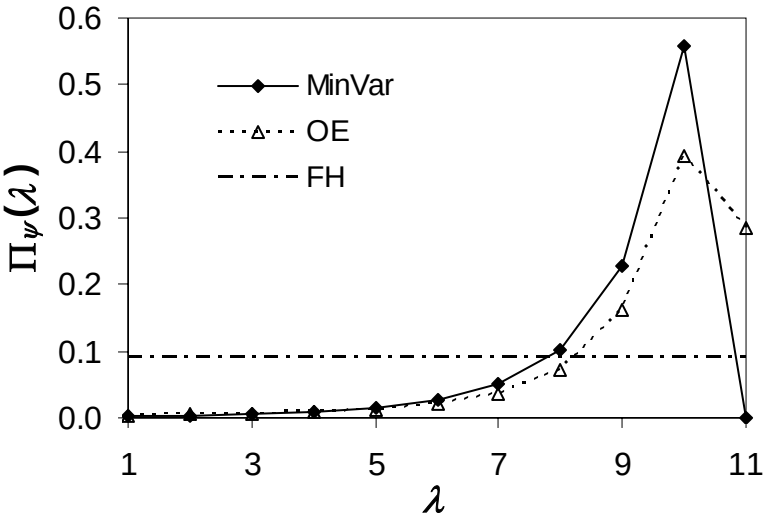

Figure A.8. Macrostate probability density (relative frequency of visits) for the solvation of a large hard-sphere in a system of small hard-spheres. The state number λ corresponds to different diameters of the large sphere; i.e., $d^* = (\lambda\text{-}1)d$, where d is the diameter of the small spheres.

Widom's test-particle method). The values of the excess chemical potential found using the 3 methods were: 38.88 (0.16) for FH, 38.87 (0.068) for OE, and 38.88 (0.065) for MinVar, where the standard deviations (shown in parentheses) were estimated from 8 repeated runs. The exact value is taken to be 38.87(0.005) (based on a simulation 100 times longer) and so neglecting any systematic deviation, the above results show that OE and MinVar perform almost identically while the FH is significantly worse, giving an error ~2.5 times larger (for fixed computational cost. As demonstrated in a previous work[20] the λ staging adopted here can be seen as suboptimal ('poor'), which explains why the FH underperforms. Since the different methods have been compared using the same system size, no attempts have been made to correct for finite-size effects in the chemical potential values; hence, it is likely that the values reported here do not represent a good approximation of the chemical potential of the infinite-size system.[30]

The fact that the MinVar method works well in this case (slightly edging the OE method) may seem at first surprising considering that, having never visited the fully coupled state, the number of round trips is zero (in contrast, the number of round trips per million attempted transitions were 5.3 for OE and 1.86 for FH). However, this is not detrimental to the efficiency of the MinVar method because, there being only one large sphere in the system, one could not improve sampling (configurational decorrelation) by swapping the identity of the fully-coupled large sphere with another equivalent 'large' sphere in the system. Furthermore, unlike the DBC system studied before, the system here is spatially homogeneous. While completing round trips is irrelevant in this case, that will not be the case for systems where the target molecule is one of many identical ones. However, there exist many cases of interest where the target molecule is truly unique; e.g., in calculating the free energy of a solute at infinite solution, or in binding free energy calculations of two distinct molecules. In

general, however, these results demonstrate that maximizing the number of round trips is not necessarily the optimal strategy to minimize the variance of free energies in EXE simulations [we also found that alternative but unreported strategies to evaluate D in Eq. (81) can produce more numerous round trips than Eq. (82) but lead to larger errors in $\beta\mu^{ex}$].

V. CONCLUSIONS

We explored the idea of improving the efficiency of free energy calculations by manipulation of the biasing weights in the EXE formalism. In order to probe the relationship between error minimization and round trips maximization, we developed a method (i.e., MinVar) to calculate the biasing weights ψ_i's that specifically aims to minimize the expected variance in the calculated free energy. The performance of this method was compared with the previously existent FH and OE methods in two systems of DBC chains, the first with N_{DBC}=10 and the second with N_{DBC}=4, and in one system in continuum space where a single hard sphere of diameter 10d is solvated by a fluid of hard spheres of diameter d. We explored the effect of the choice of biasing weights for different choices of staging between the macrostates "1" and "M". In addition to the use of the optimized Bennett's acceptance ratio method to calculate the free energy increments between macrostates, we used a sub-optimal version where we set C=0.

In the DBC systems the MinVar method was only found to yield the best results in the cases where both the staging and the incremental free energy calculation method were far from optimal. However, when the calculation was optimized either by a "smarter" choice of staging or by the use of $C=C_{opt}$ in the acceptance ratio method, the precisions of the three methods were similar. It was also observed that the

use of the optimized Bennett's acceptance ratio method seems to make the precision less dependent upon the choice of staging .

Comparison between the expected variances (σ^2_{id}) and the actual ones (σ^2_{real}) in the DBC systems, showed that the maximum attainable precision when using the optimized Bennett's acceptance ratio method can be limited by the lack of statistical independence among the samples. Hence, aiming to formally minimize σ^2_{id} at the expense of increasing the correlation between the samples, as is done in the MinVar method, can actually result in a decrease in the observed accuracy. Although we observed that there exist a direct relation between the round trip times and the degree of correlation in the samples, minimization of round trip times (as aimed by the OE method) only leads to error minimization when the correlation between the samples is the major limiting factor in the observed precision. Indeed, when studying the system of hard spheres the MinVar method performed slightly better than the OE method (and much better than the FH method) despite of *never* visiting the last macrostate (i.e., *zero* completed round trips), showing that maximizing the number of round trips does not necessarily mean higher precision. It is important to note, however, that in this system the precision of the free energy calculations is not significantly limited by correlations because of its spatial homogeneity.

In conclusion then, one can argue that an ideal strategy in estimating free energies via EXE methods would be a weighing scheme that alternates the use of OE and MinVar methods so as to harness their strengths and to help diagnose sources of statistical error. While the analysis of methods presented in this work has been restricted to the problem of calculating chemical potentials in model systems, it is expected that the conclusions from this work will also be relevant to more complex systems and problems, including the simulation of free energy changes associated to biomolecular solvation, partitioning, binding and alchemical transformations. In

addition, the MinVar method could also be applied outside the EXE methodology (i.e., in simulations where no actual transitions exist between the different macrostates) as a means to dynamically optimize the allocation of computational resources.

One shortcoming of the present MinVar methodology is that it allows for formal minimization of the variance when the transitions between macrostates are attempted only between neighboring macrostates. However, a possible extension in which transitions between non-adjacent macrostates are accounted for may be possible if free energies are efficiently calculated using the recently proposed statistically optimal method of Shirts and Chodera.[31]

ACKNOWLEDGEMENTS

This work was supported by the US Department of Energy, Grant DE-FG02-05ER15682 and by NSF, Grant 0553719.

REFERENCES

1. Frenkel, D.; Smit, B., *Understanding Molecular Simulation*. Academic Press: San Diego, CA, **2002**.

2. Bennett, C. H. *J. Comput. Phys.* **1976,** 22, (2), 245-268.

3. Virnau, P.; Muller, M. *J. Chem. Phys.* **2004,** 120, (23), 10925-10930.

4. Wu, D.; Kofke, D. A. *J. Chem. Phys.* **2005,** 123, (8), 084109.

5. Wu, D.; Kofke, D. A. *J. Chem. Phys.* **2005,** 123, (5), 054103.

6. Singh, J. K.; Errington, J. R. *J. Phys. Chem. B* **2006,** 110, (3), 1369-1376.

7. Lyubartsev, A. P.; Martsinovski, A. A.; Shevkunov, S. V.; Vorontsovvelyaminov, P. N. *J. Chem. Phys.* **1992,** 96, (3), 1776-1783.

8. Abreu, C. R. A.; Escobedo, F. A. *J. Chem. Phys.* **2006,** 124, (5), 054116.

9. Wang, F. G.; Landau, D. P. *Phys. Rev. Lett.* **2001,** 86, (10), 2050-2053.

10. Wilding, N. B.; Muller, M. *J. Chem. Phys.* **1994,** 101, (5), 4324-4330.

11. Wang, J. S.; Swendsen, R. H. *J. Stat. Phys.* **2002,** 106, (1-2), 245-285.

12. Fenwick, M. K.; Escobedo, F. A. *J. Chem. Phys.* **2003,** 119, (22), 11998-12010.

13. Lu, N. D.; Kofke, D. A.; Woolf, T. B. *J. Comput. Chem.* **2004,** 25, (1), 28-39.

14. Kofke, D. A. *Mol. Phys.* **2004,** 102, (4), 405-420.

15. Kofke, D. A.; Cummings, P. T. *Mol. Phys.* **1997,** 92, (6), 973-996.

16. Lu, N. D.; Kofke, D. A. *J. Chem. Phys.* **1999,** 111, (10), 4414-4423.

17. Lu, N.; Kofke, D. A.; Woolf, T. B. *J. Phys. Chem. B* **2003,** 107, (23), 5598-5611.

18. Berg, B. A.; Neuhaus, T. *Phys. Rev. Lett.* **1992,** 68, (1), 9-12.

19. Trebst, S.; Huse, D. A.; Troyer, M. *Phys. Rev. E* **2004,** 70, (4), 046701.

20. Escobedo, F. A.; Martinez-Veracoechea, F. J. *J. Chem. Phys.* **2007,** 127, (17), 174103.

21. Escobedo, F. A. *J. Chem. Phys.* **2007,** 127, (17), 174104.

22. Martinez-Veracoechea, F. J.; Escobedo, F. A. *J. Chem. Phys.* **2006,** 125, (10), 104907.

23. Escobedo, F. A.; Depablo, J. J. *J. Chem. Phys.* **1995,** 103, (7), 2703-2710.

24. Metropolis, N.; Rosenbluth, A. W.; Rosenbluth, M. N.; Teller, A. H.; Teller, E. *J. Chem. Phys.* **1953,** 21, (6), 1087-1092.

25. Barker, A. A. *Aust. J. Phys.* **1965,** 18, (2), 119.

26. Dotera, T.; Hatano, A. *J. Chem. Phys.* **1996,** 105, (18), 8413-8427.

27. Martinez-Veracoechea, F. J.; Escobedo, F. A. *Macromolecules* **2007,** 40, (20), 7354-7365.

28. Larson, R. G. *J. Phys. II (Paris)* **1996,** 6, (10), 1441-1463.

29. Martinez-Veracoechea, F. J.; Escobedo, F. A. *Macromolecules* **2005,** 38, (20), 8522-8531.

30. Siepmann, J. I.; McDonald, I. R.; Frenkel, D. *J. Phys.: Condens. Matter* **1992,** 4, (3), 679-691.

31. Shirts, M. R.; Chodera, J. D., *Statistically optimal analysis of samples from multiple equilibrium states*. Unpublished.